TECHNISCHE UNIVERSITÄT MÜNCHEN

TUM School of Engineering and Design

Efficient Inverse Analysis with Coupled Computational Mechanics Models for Fluid-Biofilm Interaction

Harald Willmann

Vollständiger Abdruck der von der TUM School of Engineering and Design der Technischen Universität München zur Erlangung eines

Doktors der Ingenieurwissenschaften (Dr.-Ing.)

genehmigten Dissertation.

Vorsitz:	Prof. Dr.-Ing. habil. Fabian Duddeck
Prüfende der Dissertation:	
	1. Prof. Dr.-Ing. Wolfgang A. Wall
	2. Prof. Phaedon-Stelios Koutsourelakis, Ph.D.

Die Dissertation wurde am 31.01.2024 bei der Technischen Universität München eingereicht und durch die TUM School of Engineering and Design am 02.09.2025 angenommen.

Abstract

The modeling of biofilms and their interaction with a surrounding fluid flow is always a coupled mechanical problem. Biofilms predominantly develop in the environment of moving water and therefore the coupling to the fluid flow must be considered when analyzing biofilm deformation. In the last years the computational methods for such coupled problems and especially fluid-structure interaction (FSI) have been developed continuously. On the experimental side, the quality of observations of the deformation of biofilms has increased. Especially optical coherence tomography (OCT) was established as an imaging technique for biofilms cultivated in a transparent channel, also called the biofilm flow cell. In this work, the methodological foundation is laid to use experimental observations on biofilms to build the best fitting coupled mechanical models for biofilms. The search for the best fitting model for a desired model result is called *inverse analysis*. Here the desired model result is one that lies as close to experimental observations as possible. Given that OCT scans provide only the geometrical shape of biofilms a special challenge lies in the suitable comparison of a biofilm surface shape between OCT scan and numerical model.

For inverse analysis it is distinguished between the *deterministic* and the *statistical* approach that are both discussed and compared in this work. The continuum mechanical approach to modeling of different physical aspects of flow cell experiments with biofilms is described and the numerical approach to solving the partial differential equations with the finite element method (FEM) is briefly summarized. In the presentations of the developed methods artificially generated data is used to discuss and explain the results obtained and the obstacles in application.

The developed deterministic approach is based on the *Levenberg-Marquardt* method for optimization. Therein the discrepancy between experimental observation and model result are minimized. It is demonstrated that the material parameters of a hyperelastic material model, the porosity in a poroelastic material model and the growth parameters in a surface growth model can be analyzed with this approach.

The developed statistical approach is one for *Bayesian calibration*. There, a *Gaussian process* (GP) surrogate model on the *logarithmic likelihood* is used to keep control over the computational budget. The result of Bayesian calibration goes beyond a single point estimate for the best parameters. It allows a statistical interpretation of the computational mechanics model related to the observed experiment. Here prior knowledge about the parameters, the effect of different, uncertain parameters and a model for measurement errors or noise can be included seamlessly.

The respective strengths and weaknesses of the developed methods are discussed and the advantages over each other are concluded. The developed methods and their discussion enable an analyst of biofilm experiments to find a best fitting material model in a fluid-biofilm interaction setting depending on the quality and amount of data retrieved from experiments.

Zusammenfassung

Die Modellierung von Biofilmen und ihrer Interaktion mit einer umgebenden Strömung ist immer ein gekoppeltes mechanisches Problem. Biofilme wachsen vorwiegend in der Umgebung fließenden Wassers and daher muss die Kopplung zur Strömung bei der Analyse ihrer Verformung berücksichtigt werden. In den letzten Jahren wurden kontinuierlich Berechnungsmethoden für solche gekoppelten Probleme, insbesondere für *Fluid-Struktur Interaktion* (FSI) entwickelt. Auf der experimentellen Seite hat sich die Qualität der Beobachtungen der Verformung von Biofilmen verbessert. Speziell die optische Kohärenztomographie (OCT) wurde als bildgebendes Verfahren für Biofilme, die in einem transparenten Kanal kultiviert werden, etabliert. So ein transparenter Kanal wird auch Biofilm Flusszelle genannt. In dieser Arbeit wird die methodische Grundlage dafür bereitet, experimentelle Beobachtungen von Biofilmen zu nutzen um ein am besten passendes mechanisches Modell für Biofilme zu finden. Die Suche nach dem am besten passenden Modell für ein angestrebtes Modellergebnis wird *inverse Analyse* genannt. Hier ist das angestrebte Modellergebnis eines, das möglichst nahe an den experimentellen Beobachtungen liegt. Da OCT Aufnahmen nur die geometrische Form von Biofilmen liefern, liegt eine spezielle Herausforderung darin, die Oberflächenform von Biofilmen zwischen OCT Aufnahme und numerischem Modell passend zu vergleichen.

In der inversen Analyse werden der *deterministische* und der *statistische* Ansatz unterschieden, die beide in dieser Arbeit diskutiert und verglichen werden. Der kontinuumsmechanische Ansatz zur Modellierung von verschiedenen physikalischen Aspekten von Flusszellen Experimenten mit Biofilmen wird beschrieben und der numerische Ansatz zur Lösung der partiellen Differenzialgleichungen mit der finite Elemente Methode (FEM) wird kurz zusammengefasst. In der Vorstellung der entwickelten Methoden werden künstlich erzeugte Daten verwendet, um anhand derer die erzielten Resultate und die Schwierigkeiten in der Anwendung zu diskutieren und zu erklären.

Der entwicklete deterministische Ansatz basiert auf der *Levenberg-Marquardt* Optimierungsmethode. Dabei wird die Abweichung zwischen experimenteller Beobachtung und Ergebnis des Modells minimiert. Es wird gezeigt, dass die Parameter eines hyperelastischen Materialmodells, die Porosität in einem poroelastischen Materialmodell und die Wachstumsparameter in einem Oberflächenwachstumsmodell mit diesem Ansatz untersucht werden können.

Der entwickelte statistische Ansatz ist einer der *Bayesschen Kalibirierung*. Darin wird basierend auf einem Gaussprozess (GP) ein Ersatzmodell für logarithmische Wahrscheinlichkeiten genutzt, um damit den Rechenaufwand kontrollieren zu können. Das Ergebnis einer Bayesschen Kalibrierung reicht weiter als eine Abschätzung eines einzelnen, optimalen Satzes an Parametern. Es erlaubt eine statistische Interpretation des numerischen Modells im Verhältnis zu experimentellen Beobachtungen. Hier können vorher bekanntes Wissen über die untersuchten Parameter, der Effekt von Un-

sicherheiten bezüglich anderer Parameter und ein Modell für Messfehler und -rauschen nahtlos berücksichtigt werden.

Die entsprechenden Stärken und Schwächen der entwickelten Ansätze werden diskutiert und die jeweiligen Vorteile herausgearbeitet. Die entwickelten Methoden und deren Diskussion ermöglichen es dem Analysten eines Biofilm Experiments abhängig von der Qualität und der Menge der gewonnen Daten, ein optimal passendes Materialmodell in einem Fluid-Biofilm Interaktions Szenario zu finden.

Contents

1 Introduction

Biofilms are build up by aggregates of microorganisms of various kind. They provide protection for the microorganisms against environmental influences and are therefore the preferred habitat compared also to the planktonic state for many species. Before it is elaborated on what is known currently about biofilms it is started with the question of how they deserve this name. Historically the word film has been introduced, because the first observations in the field were concerning appearances as biological layers on surfaces [37]. The term has developed to describe a whole form of live of microorganisms, that have been observed in various shapes. The International Union of Pure and Applied Chemistry (IUPAC) has found the definition for biofilm as "Aggregate of microorganisms in which cells that are frequently embedded within a self-produced matrix of extracellular polymeric substance (EPS) adhere to each other and/or to a surface"[90]. This definition clearly focuses the mechanical viewpoint of microorganisms living in biofilms to adhere to each other and adhere to a surface. The term adherence immediately arises the question of what forces biofilms develop against deformation and separation. In other words adherence suggests that a macroscopic mechanical description can be found to represent biofilms with a proper material model. More precisely the mechanical modeling of biofilms is mainly targeting the biofilm matrix that makes up the majority of the dry mass in biofilms. The biofilm matrix has a variety of functions for the microorganisms besides the adhesion to surfaces and the cohesion inside of a biofilm [36, 38]. Although biofilms are often considered bacterial biofilms [39] other types of microorganisms interact with them in integrated communities [13, 14, 80].

1.1 Motivation

As various as the constituents and inhabitants of biofilms can be, also their appearance differs. They occur in natural aquatic environments, industrial aquatic systems like pipelines or filters and especially in wastewater treatment, but also in the biomedical field, e.g., on medical implants and dental unit water lines [29, 49]. Especially in the biomedical field inside the human body they can be a source of infectious diseases [30, 48] and therefore strategies for their removal must be developed. In industrial applications and especially heat exchangers an increase in flow resistance and deterioration of heat transfer can directly be linked to the effect of biofilm occurence [25]. On the other hand, e.g., for wastewater treatment, biofilms can be beneficial and therefore desired as

they can be applied for productive tasks [35, 68]. Biofilms can also be used as living catalysts in chemical syntheses [47].

From the engineering perspective on biofilm mechanics, the main research question of this work arises of how to model biofilms that are exposed to a fluid flow, that interacts with them. Given the complexity of interactions between microorganisms and EPS no single, general explanation of macroscopic behavior is available. The biofilm matrix has been phrased "dark matter" of biofilms [36]. That is why a continuum mechanical approach to biofilm mechanics modeling is followed in this work. Therefore, biofilms are modeled as continuous bodies with nonlinear kinematic description and common material models.

Implicitly following the continuum mechanical approach, strategies for the phenomenological characterization of biofilm materials have been developed in the mechanical analyses of biofilms [21, 24, 45, 46]. With the great variety of biofilm compositions, occurrence and shapes apparently also a variety of testing strategies has been developed. For this work it is a valuable goal to find a repeatable testing strategy for biofilm material characterization. The tests summarized in the literature describe biofilms as very soft materials.

The removal of a biofilm species from the surface it grew on drastically compromises its integrity. That is why a non-destructive approach to estimate material properties from image data was proposed [82]. This strategy for parameter estimation is tailored to a pronounced biofilm patch on a global basis. It has served as a benchmark in biofilm mechanics [20]. The estimation relies on characteristic shapes of the biofilm patch to be able to geometrically measure and compare the deformation from image data. The basic principle to grow a biofilm in a flow cell, that is accessible to imaging at all times, expose it to a variable load in the same environment it was grown and make an estimation of the material parameters based on the deformation observed under varying load is also followed in this work. The difference is, that the very limiting assumptions are successively loosened for the presented approaches.

As the shapes of biofilms even for growth under automated, reproducible environmental conditions vary [44], the goal in this work is to find a flexible way of comparing biofilm shapes under deformation. The resulting load onto the biofilm can only be reduced to one comparable quantity, the fluid volume rate, if the full coupling between fluid and biofilm is considered in the model. That is why continuum models for fluid-solid interaction (FSI) need to be employed for modeling a representation of the biofilm [72]. In the context of inverse analysis, a representation of the experiment is built in a computational model. The results from the computational model are then compared to experimental observations in order to find the best fitting parameterization of the model. This approach was already followed before for linear solid mechanical models and a single material parameter [72]. Additionally to the model assumptions also the type of comparison between biofilm shapes from experimental observations and from nu-

merical model evaluations needs more flexibility and is therefore elaborated on in this work.

Once a suitable strategy for the comparison of shapes is found, it must be decided upon how to make the best use of it. A common and direct approach that is followed in Paper A is to define a discrepancy measure between experimental observations and results of multiple evaluations of a numerical model and minimize this discrepancy with regard to the material parameters. A second and more flexible approach that was followed in Paper B is to define a similarity measure between experimental observations and numerical model results and build a probabilistic model for the probability density in all parameter dimensions. The probability model describes how likely parameter combinations in the given model lead to the experimental observations made. Then as a byproduct the optimal point, maximizing this probability, can be found. Additionally to a single point estimate for the optimum, a more general, flexible and conclusive explanation for observed data can be given. This approach also allows incorporating models for measurement errors into the probabilistic modeling. Both approaches lead to algorithms that are widely referred to as inverse analysis, as they are related to the question: If the outcome of an experiment is known, what is the best model to explain what was observed?

This leads to the general research objective to propose a method for the determination of a material model for biofilms. With the recent advances in experiments in form of flow cell experiments and the imaging via optical coherence tomography (OCT), such data are regarded as the starting point. This type of experiments further allows to keep the biofilm in the same environment during the whole life cycle from initial growth to arbitrary testing protocols. Thus, it is the goal to develop a conceptual workflow for the interpretation of a non-destructive test-cycle with the help of modern computational mechanical models in order to make such models available for reliable model predictions.

1.2 Contributions

This thesis is based on the work that has been channeled into two main publications that are included cumulatively in the appropriate context of this thesis. They are further placed in the appendix of this thesis as Paper A and Paper B in the published formats.

Paper A:
[96] H. Willmann and W. A. Wall. “Inverse analysis of material parameters in coupled multi-physics biofilm models”. In: *Advanced Modeling and Simulation in Engineering Sciences* 9.7 (2022). DOI: 10.1186/s40323-022-00220-0

Paper B:
[95] H. Willmann, J. Nitzler, S. Brandstäter, and W. A. Wall. "Bayesian calibration of coupled computational mechanics models under uncertainty based on interface deformation". In: *Advanced Modeling and Simulation in Engineering Sciences* 9.24 (2022). DOI: 10.1186/s40323-022-00237-5

In these two articles, that will consistently will be referred to as Paper A and Paper B in the remainder of the thesis, several contributions for reaching the research objectives have been presented.

- **Development of a method for deterministic inverse analysis (Paper A)** In this article a basic, stable measure for the discrepancy between numerical model result and experimental observations is presented and tested. This measure allows for the formulation of an objective function in form of least-squares, that is minimized using a Levenberg-Marquardt approach. This is a novel combination of an optimization algorithm with a simple discrepancy measure and coupled computational models for fluid-biofilm interaction.

- **Development of a method using a Bayesian approach (Paper B)** In this article a general Bayesian formulation of the probabilistic inverse problem under the influence of uncertainties is presented. The method results in a global approximation to the multi-dimensional posterior probability density in the parameter space. The influence of different prior assumptions as well as different discrepancy measures is studied and an exemplary discussion of the interpretation of the result is presented. This is a new combination of known tools from a probabilistic toolbox and fluid-solid interaction models to analyze a solid phase based on the deformation of the interface.

- **Proof of concept for existing biofilm models (Paper A)** Previously known physical models of biofilms are used in example inverse analyses for the key parameters in homogeneous, heterogeneous and poroelastic biofilm models as well as a surface growth model. This proofs that a comparison of model and experiment based on the shape of the interface between biofilm and fluid flow allows inverse analysis.

- **Phenomenological observations in inverse analysis approaches (Paper A and Paper B)** In both articles several general phenomena are observed and discussed with generic academic examples. This allows a neutral, unbiased interpretation of the results. Some fundamental structures in the objective function or probability densities linked to the comparison of surfaces have been observed and discussed, as well as the influence of noise on the results. The avalability of the new methods allows a thorough discussion and comparison of strengths and weaknesses of both

a determistic and a probabilisitic approach to inverse analysis. This leads to specific recommendations which approach is preferrable in which scenario depending on, e.g., quality of experimental data, cost of computational model evaluation, availability of prior knowledge or the presence of uncertainties.

- **Discussion of computational efficiency (Paper A and Paper B)** The evaluation of the computational model is the most expensive component in both presented approaches, so a special focus is persistently laid on computational efficiency. This discussion is further pursued in this thesis.

Software engineering perspective Current work was only possible in this short period of time and with the usage of modern FEM technology because the foundation in computational modeling was build in persistent, continuous efforts that contributed to the software BACI (Bavarian Advanced Computational Initiative) [8]. BACI is an inhouse research software programmed in C++. BACI is under persistent development at the institute for computational mechanics (LNM) at the Technical University of Munich (TUM). It is currently hosted on servers of the Leibniz Rechenzentrum (LRZ) in Garching and jointly developed in a cooperation with further institutes. Especially recent works in fluid-solid interactions [66, 77], the modeling of porous materials in a poroelastic framework [92] and their coupling in contact with solids and interaction with fluids [5] have made presented numerical examples possible. Dedicated developments in biofilm modeling [28, 98] have lead to a comprehensional biofilm model in BACI for fluid-biofilm interaction, the distribution of potential nutrients and biofilm surface growth. Contributions and additions to BACI and the BACI project have been developed during the creation of this work. BACI was already existent and a powerful tool before the referenced works, and the contributions that lead to what BACI is today are listed online [8], but not explicitly referenced here as it would distract the attention from the direct connections to presented work.

Developed inverse analysis approaches were implemented in the python software QUEENS [15] that is currently developed at LNM at TUM. A base version of the software QUEENS was provided by AdCo Engineering^{GW} GmbH, which is gratefully acknowledged. Recent efforts in inverse analysis at LNM that were implemented in BACI [18, 56] have been partly re-implemented in QUEENS during this work. It showed that especially the flexibility of controlling the numerical model evaluations from the outside, brings significant advantages and therefore the strategic decision of implementing the inverse analysis in QUEENS and outside of the simulation software BACI has been made.

1.3 Outline

In this cumulative work we give a brief introduction to the mechanical modeling of biofilms in chapter 2. Then the deterministic and the statistical approach to inverse analysis are introduced in chapter 3. Therein, the publications Paper A and Paper B are included and summarized. The summaries are placed, where the content of the full text publications fits best. Details presented in the articles are not repeated in the main part of this dissertation wherever possible. The intention is to introduce the topics so far, that the explanations and discussions herein can be understood. Some minor additions to the fundamentals of the published articles are presented. The two approaches are discussed and compared in chapter 4. The appendix contains the full text versions of Paper A and Paper B.

2 Mechanical modeling of Biofilms

Since the focus in this work is set on the mechanical behavior of biofilms, a profound mechanical modeling of biofilms is essential to enable inverse analysis. It is expected for the modeling of soft biological materials, as which biofilms must be considered, that the use of a nonlinear description of the kinematics is essential. The consistent employment of *nonlinear continuum mechanics* makes room for the usage of elaborate nonlinear material models. The aimed use case for the inverse analysis is flow cell experiments with biofilms. There, the idea is to keep biofilms in their surrounding environment for their whole life and testing cycle. Therefore, a coupling to the fluid flow that is controlled by the experimenter must be accounted for in every relevant model. This means that generally a coupled multi-field mechanical model needs to be employed. In this thesis, a short presentation of the initial and boundary value problem of fluid-solid interaction is presented to enable a discussion of the model assumptions and their influence on inverse analysis.

With the development of computational mechanical modeling in general, also the number of applications in biofilm modelling has increased. A review by Horn and Lackner [51] on biofilm modeling gives an overview of the broad landscape of approaches in biofilm modeling. Modeling physics related to biofilms brings in a variety of aspects that can be considered. Amongst others those are solid mechanics, poromechanics, fluid-biofilm interaction, nutrient distribution, biofilm growth and erosion and detachment. Several modeling approaches have been presented in the past regarding one or more of these physical aspects combined.

In this chapter first the general equations of nonlinear kinematics are presented in section 2.1. Then general relations between kinematics and material models are drawn in section 2.2. This allows to extend the presentation to initial and boundary value problems in section 2.3. Finally, possibilities for the computational solution of the equations are sketched in section 2.4.

2.1 Nonlinear continuum mechanics

The presentation of nonlinear continuum mechanics allows referencing the respective aspects of the physical models and therefore further allows the interpretation of inverse analysis results by clear definitions of the relevance of the incorporated parameters. The following presentation is intended to be concise and the interested reader is referred to

standard works in the field e.g. [23, 50].

To define the basic concepts of nonlinear kinematics a unique mapping φ_t that maps from the *reference configuration* Ω_0 to the *current configuration* Ω_t is defined as seen in Figure 2.1.

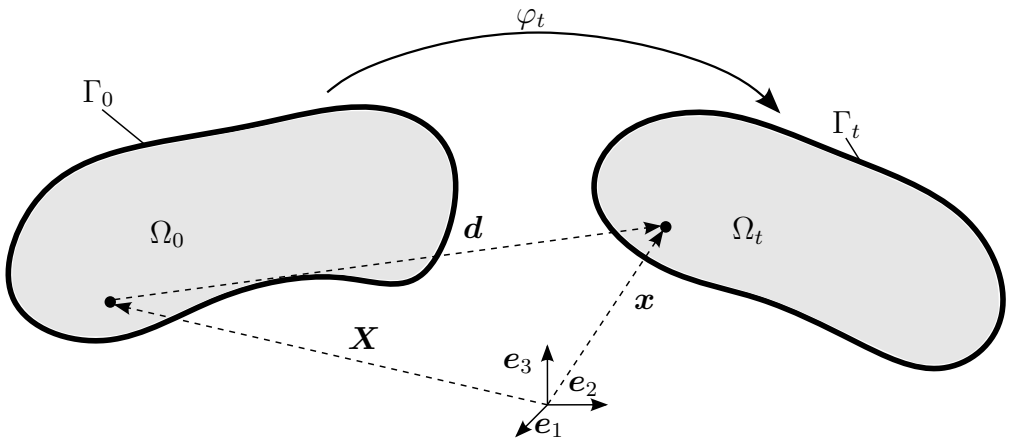

Figure 2.1: Mapping φ_t from reference configuration Ω_0 to current configuration Ω_t.

In the regarded cases it is sufficient to choose the initial configuration as the reference configuration, as for the desired purpose the initial configuration is also assumed to be undeformed and therefore makes a suitable reference configuration. The mapping is defined as

$$\varphi_t(\boldsymbol{X}, t) : \begin{cases} \Omega_0 \to \Omega_t \\ (\boldsymbol{X}, t) \mapsto \boldsymbol{x}(\boldsymbol{X}, t) \end{cases} \tag{2.1}$$

for material points at coordinates $\boldsymbol{X}$ from the reference to the current configuration at coordinates $\boldsymbol{x}$. Therefore, the *displacements* $\boldsymbol{d}$ compute to

$$\boldsymbol{d} = \boldsymbol{x} - \boldsymbol{X}. \tag{2.2}$$

Further the *velocity* $\boldsymbol{V}$ can be computed as the total time derivative of the displacements

$$\boldsymbol{V} = \frac{\mathrm{d}\boldsymbol{d}}{\mathrm{d}t} = \left.\frac{\partial \boldsymbol{d}}{\partial t}\right|_{\boldsymbol{X}} \tag{2.3}$$

and the *acceleration* $\boldsymbol{A}$ as a further total time derivative of the velocity reads as

$$\boldsymbol{A} = \frac{\mathrm{d}^2\boldsymbol{d}}{\mathrm{d}t^2} = \left.\frac{\partial \boldsymbol{V}}{\partial t}\right|_{\boldsymbol{X}}. \tag{2.4}$$

The kinematic relation at a material point can be given with help of the *deformation gradient* $\boldsymbol{F}$ which is

$$\boldsymbol{F} = \frac{\partial \boldsymbol{x}(\boldsymbol{X}, t)}{\partial \boldsymbol{X}}. \tag{2.5}$$

From the deformation gradient it can be shown that the volume change of a infinitesimal volume element $\mathrm{d}V$ in material configuration to the current deformed state $\mathrm{d}v$ is computed as

$$\det(\boldsymbol{F})\mathrm{d}V = J\mathrm{d}V = \mathrm{d}v \tag{2.6}$$

also introducing the alternative expression as a Jacobian $J = \det \boldsymbol{F}$ which is the determinant of the deformation gradient. The deformation gradient can generally be split multiplicatively into a stretch tensor $\boldsymbol{U}$ or $\boldsymbol{v}$ and rotational component $\boldsymbol{R}$. This is also called polar decomposition. It is written as

$$\boldsymbol{F} = \boldsymbol{R} \cdot \boldsymbol{U} = \boldsymbol{v} \cdot \boldsymbol{R} \tag{2.7}$$

and therefore the stretch tensors are known as *right stretch tensor* $\boldsymbol{U}$ and the *left stretch tensor* $\boldsymbol{v}$. The polar decomposition separates the rigid body movement from the deformation of the domain.

The deformation gradient is used for the definition of *right Cauchy-Green deformation tensor* $\boldsymbol{C} = \boldsymbol{F}^{\mathsf{T}} \cdot \boldsymbol{F}$ that can be used to introduce the *Green-Lagrange strains* $\boldsymbol{E}$ as

$$\boldsymbol{E} = \frac{1}{2}\left(\boldsymbol{F}^{\mathsf{T}} \cdot \boldsymbol{F} - \boldsymbol{I}\right) = \frac{1}{2}\left(\boldsymbol{C} - \boldsymbol{I}\right). \tag{2.8}$$

It can quickly be checked that this strain measure fulfills the property to be zero for rigid body movement. For rigid body movement the deformation gradient becomes $\boldsymbol{F} = \boldsymbol{R} \cdot \boldsymbol{I}$ and therefore $\boldsymbol{C} = \boldsymbol{R}^{\mathsf{T}} \cdot \boldsymbol{R} = \boldsymbol{I}$.

To be able to formulate equations for balance, the concept of *stresses* needs to be introduced. For the current configuration it is straightforward to define a traction and follow Cauchy's stress theorem to the existence of a unique *Cauchy stress tensor* that relates *surface tractions* on a surface to the stress state.

Surface tractions are a continuous physical quantity for the force on a surface. To define them, the limit towards an infinitesimal surface element is regarded. If $\Delta \boldsymbol{f}$ is the resulting force on an area Δa, the limit

$$\boldsymbol{t} = \lim_{\Delta a \to 0} \frac{\Delta \boldsymbol{f}}{\Delta a} \tag{2.9}$$

describes the continuous surface tractions. Cauchys theorem states that there is a unique second order tensor $\boldsymbol{\sigma}$ that relates the stress state in any point $(\boldsymbol{x}, t)$ in current configuration to the surface tractions with unit normal $\boldsymbol{n}$

$$\boldsymbol{t} = \boldsymbol{\sigma}(\boldsymbol{x}, t) \cdot \boldsymbol{n}. \tag{2.10}$$

The kinematic relations can be used to compute the *second Piola-Kirchhoff stress tensor*

$$\boldsymbol{S} = J\boldsymbol{F}^{-1}\boldsymbol{\sigma}\boldsymbol{F}^{-\mathsf{T}} \tag{2.11}$$

that is commonly used to describe solids in material configuration.

2.2 Material modeling

The material model in continuum mechanics is generally relating the current state of a material to its stress response. The relations are also known as constitutive equations.

2.2.1 Hyperelastic materials

The materials that are used in this work are *hyperelastic materials*. Materials of this kind are characterized by the existence of a unique *strain-energy density function* Ψ. This is an expression for the stored energy through deformation. It is expected to only depend on the current deformation state. This can be expressed as

$$\Psi = \Psi(\boldsymbol{F}) = \Psi(\boldsymbol{U}) = \Psi(\boldsymbol{C}) = \Psi(\boldsymbol{E}), \tag{2.12}$$

as these kinematic quantities depend only on the deformation state. Further the last three $\boldsymbol{U}, \boldsymbol{C}, \boldsymbol{E}$ are also independent from rigid body movements. As a consequence of the second law of thermodynamics it can be shown that for such materials the relation between stresses and strains can straightforward be computed as a partial differentiation of the strain-energy density function as

$$\boldsymbol{S} = \frac{\partial \Psi(\boldsymbol{E})}{\partial \boldsymbol{E}} = 2\frac{\partial \Psi(\boldsymbol{C})}{\partial \boldsymbol{C}}. \tag{2.13}$$

2.2.2 Example material models

As they were used in the demonstration examples in Paper A and Paper B specifically two common isotropic material models are presented. Those are the *Saint-Venant-Kirchhoff* and *Neo-Hooke* materials. They are both amongst the most simple hyperelastic material models.

The Saint-Venant-Kirchhoff material is known for its analogy to linear continuum mechanics with its linear relation between stress and strain. The strain energy function can be written as

$$\Psi_{\mathrm{SVK}} = \frac{\lambda}{2}\left(\mathrm{tr}\left(\boldsymbol{E}\right)\right)^2 + \mu \boldsymbol{E} : \boldsymbol{E} \tag{2.14}$$

with the *Lamé coefficients* λ and μ. After the partial derivation (2.13)

$$\boldsymbol{S}_{\mathrm{SVK}} = \lambda \mathrm{tr}\left(\boldsymbol{E}\right) \boldsymbol{I} + 2\mu \boldsymbol{E} \tag{2.15}$$

the linear dependency between $\boldsymbol{E}$ and $\boldsymbol{S}_{\mathrm{SVK}}$ becomes apparent. For the inverse analyses examples in Paper A and Paper B a second common parameterization with *Young's modulus* E and *Poisson's ratio* ν was used. This is a reparameterization of the Lamé coefficients which compute as

$$\mu = \frac{\mathrm{E}}{2(1+\nu)}, \quad \lambda = \frac{\nu \mathrm{E}}{(1+\nu)(1-2\nu)}. \tag{2.16}$$

A further material model, that is often used for biomechanical material modeling is the *neo Hookean* material. This is written with the strain energy function

$$\Psi_{\mathrm{NH}} = \frac{\mu}{2}\left(\mathrm{tr}\left(\boldsymbol{C}\right) - 3\right) - \mu \ln(J) + \frac{\lambda}{2}\left(\ln(J)\right)^2 . \tag{2.17}$$

Which, after partial derivation (2.13) leads to the stress tensor

$$\boldsymbol{S}_{\mathrm{NH}} = \mu\left(\boldsymbol{I} - \boldsymbol{C}^{-1}\right) + \lambda \ln(J)\boldsymbol{C}^{-1}. \tag{2.18}$$

Additional to the two presented material models, there is a wide field of more elaborate material models with potentially more parameters. For the modeling of biofilms it is suggested to begin with these two common material models and follow a phenomenological approach to choose a model that fits best to observations as long as no detailed micromechanical explanation of biofilm material behavior is found. To find a more complex material description, for example in [17] a generic polynomial material law was used to determine the contributions of different exponents to the observed material behavior in an inverse analysis approach.

2.3 Physical models

Under consideration of the kinematic relations, the evaluation of balance equations leads to a set of continuous equations for the homogeneous modeling of biofilms. The balance of mass, balance of momentum, balance of angular momentum and balance of energy must hold. In Paper A and Paper B the field equations for solid and fluid mechanics as well as their coupling at an interface are directly presented without boundary or initial conditions for the sake of brevity. Therefore, it is elaborated on those here, so that a mechanical foundation is provided to serve as context for the publications. To get a first overview of the domains, boundaries and coupling interface for solid-fluid interaction they are sketched in Figure 2.2. Therein the outer domain boundaries are combined *Dirichlet* (D) and *Neumann* (N) boundaries. In general on the Dirichlet boundary the primary variables are prescribed, whereas on the Neumann boundary the tractions are prescribed.

2.3.1 Fluid equations

For the fluid in a flow channel the model of an *incompressible Navier-Stokes flow* of a Newtonian fluid is used. For the solution of the fluid-solid coupling an arbitrary Langrangian-Eulerian (ALE) approach is used. It accounts for the domain displacements $\boldsymbol{d}^{\mathrm{G}}$ on the deformable fluid domain, here represented by Ω^{G}. In ALE formulation the fluid equations read as

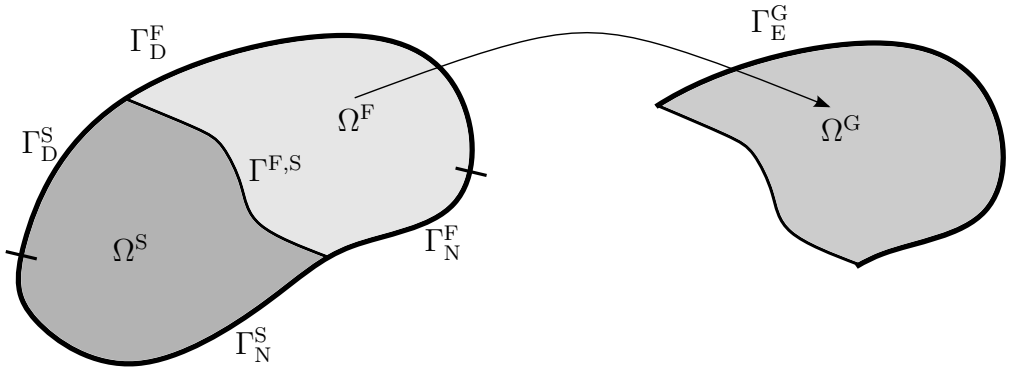

Figure 2.2: Domain and boundary names in arbitrary Langrangian-Eulerian (ALE) approach of fluid-solid interaction.

$$\rho^{\mathrm{F}} \frac{\partial \boldsymbol{v}^{\mathrm{F}}}{\partial t} + \rho^{\mathrm{F}} (\boldsymbol{c}^{\mathrm{F}} \cdot \boldsymbol{\nabla}) \boldsymbol{v}^{\mathrm{F}} - 2\mu^{\mathrm{F}} \boldsymbol{\nabla} \cdot \boldsymbol{\epsilon}(\boldsymbol{v}^{\mathrm{F}}) + \boldsymbol{\nabla} p^{\mathrm{F}} = \rho^{\mathrm{F}} \hat{\boldsymbol{b}}^{\mathrm{F}} \quad \text{in } \Omega^{\mathrm{F}} \times (0,T) \tag{2.19a}$$

$$\boldsymbol{\nabla} \cdot \boldsymbol{v}^{\mathrm{F}} = 0 \qquad \text{in } \Omega^{\mathrm{F}} \times (0,T). \tag{2.19b}$$

with the ALE convective velocity $\boldsymbol{c}^{\mathrm{F}} = \boldsymbol{v}^{\mathrm{F}} - \dfrac{\partial \boldsymbol{d}^{\mathrm{G}}}{\partial t}$ that accounts for the fluid velocity relative to the deforming fluid domain. The further variables are fluid velocity $\boldsymbol{v}^{\mathrm{F}}$, fluid pressure p^{F} and the body force $\hat{\boldsymbol{b}}^{\mathrm{F}}$ acting on the fluid domain $\Omega^{\mathrm{F}} \times (0,T)$ for all times. The fluid density ρ^{F} and fluid dynamic viscosity μ^{F} are material parameters. The strain rate tensor $\boldsymbol{\epsilon}(\boldsymbol{v}^{\mathrm{F}})$ is further computed as

$$\boldsymbol{\epsilon}(\boldsymbol{v}^{\mathrm{F}}) = \frac{1}{2} \left(\boldsymbol{\nabla} \boldsymbol{v}^{\mathrm{F}} + \left(\boldsymbol{\nabla} \boldsymbol{v}^{\mathrm{F}} \right)^{\mathsf{T}} \right). \tag{2.20}$$

With the strain rate tensor and the dynamic viscosity of the fluid, the Cauchy stress in the fluid domain of a *Newtonian fluid* can be defined as

$$\boldsymbol{\sigma}^{\mathrm{F}} = -p^{\mathrm{F}} \boldsymbol{I} + 2\mu^{\mathrm{F}} \boldsymbol{\epsilon}(\boldsymbol{v}^{\mathrm{F}}). \tag{2.21}$$

This finally allows to formulate the boundary conditions. On the fluid Dirichlet boundary $\Gamma_{\mathrm{D}}^{\mathrm{F}}$ the velocity and on the fluid Neumann boundary $\Gamma_{\mathrm{N}}^{\mathrm{F}}$ the fluid traction is prescribed

$$\boldsymbol{v}^{\mathrm{F}} = \hat{\boldsymbol{v}} \quad \text{on } \Gamma_{\mathrm{D}}^{\mathrm{F}} \times (0,T), \tag{2.22}$$

$$\boldsymbol{\sigma}^{\mathrm{F}} \cdot \boldsymbol{n}^{\mathrm{F}} = \hat{\boldsymbol{h}}^{\mathrm{F}} \quad \text{on } \Gamma_{\mathrm{N}}^{\mathrm{F}} \times (0,T). \tag{2.23}$$

For the initial time an initial divergence free velocity field $\boldsymbol{v}^{\mathrm{F}}(\boldsymbol{x}, t=0) = \boldsymbol{v}_0^{\mathrm{F}}(\boldsymbol{x})$ needs to be given at all spatial points $\boldsymbol{x} \in \Omega^{\mathrm{F}}$ in the fluid domain.

The ALE approach for the fluid comes with some further restrictions on the fluid domain displacements $\boldsymbol{d}^{\mathrm{G}}$. First on the domain boundaries $\Gamma_{\mathrm{E}}^{\mathrm{G}}$ a change in shape is prohibited. For that it is sufficient to restrict the movement normal to the fluid boundary

$$\boldsymbol{d}^{\mathrm{G}} \cdot \boldsymbol{n}^{\mathrm{G}} = 0 \quad \text{on } \Gamma_{\mathrm{E}}^{\mathrm{G}} \times (0, T). \tag{2.24}$$

The fluid domain displacement field $\boldsymbol{d}^{\mathrm{G}}(\boldsymbol{x}, t)$ is the solution of an arbitrary mapping, that is often chosen as the solution of a quasi elastostatic pseudo-solid, that needs to fulfill compatibility at the interface $\Gamma^{\mathrm{F,S}}$. The material law for the pseudo-solid should be chosen, so that fluid domain displacements are distributed as well as possible.

2.3.2 Solid equations

The most simple and therefore first approach followed in this work is to model biofilms as homogeneous, isotropic solids. For those the balance of linear momentum

$$\rho_0^{\mathrm{S}} \frac{\mathrm{d}^2 \boldsymbol{d}^{\mathrm{S}}}{\mathrm{d}t^2} = \boldsymbol{\nabla}_0 \cdot (\boldsymbol{F} \cdot \boldsymbol{S}) + \rho_0^{\mathrm{S}} \hat{\boldsymbol{b}}_0^{\mathrm{S}} \quad \text{in } \Omega_0^{\mathrm{S}} \times (0, T) \tag{2.25}$$

needs to hold. Where the equation is solved for the solid displacements $\boldsymbol{d}^{\mathrm{S}}$ under the body force $\hat{\boldsymbol{b}}_0^{\mathrm{S}}$ on the reference domain $\Omega_0^{\mathrm{S}} \times (0, T)$ for all times with the material parameter ρ_0^{S}, the density of the solid in reference configuration. For the solid, the boundary conditions

$$\boldsymbol{d}^{\mathrm{S}} = \hat{\boldsymbol{d}} \quad \text{on } \Gamma_{\mathrm{D}}^{\mathrm{S}} \times (0, T), \tag{2.26}$$

$$(\boldsymbol{F} \cdot \boldsymbol{S}) \cdot \boldsymbol{n}^{\mathrm{S}} = \hat{\boldsymbol{h}}^{\mathrm{S}} \quad \text{on } \Gamma_{\mathrm{N}}^{\mathrm{S}} \times (0, T), \tag{2.27}$$

need to hold and the initial conditions on the displacement field $\boldsymbol{d}^{\mathrm{S}}(\boldsymbol{x}, t = 0) = \boldsymbol{d}_0^{\mathrm{S}}(\boldsymbol{x})$ and $\dfrac{\mathrm{d}\boldsymbol{d}^{\mathrm{S}}}{\mathrm{d}t}(\boldsymbol{x}, t = 0) = \dot{\boldsymbol{d}}_0^{\mathrm{S}}(\boldsymbol{x})$ on the whole domain $\boldsymbol{x} \in \Omega^{\mathrm{S}}$ must be prescribed.

2.3.3 Fluid-solid interaction

To be able to model a biofilm flow cell experiment, the coupling of biofilm and fluid flow must be considered and the coupled system of fluid-solid interaction (FSI) solved. As a first model of a flow cell experiment, the coupling of an incompressible Navier-Stokes flow and a hyperelastic solid can be used. To specify the coupling, the conditions on the interface must be set. Often the term fluid-structure interaction is used in the same context. This is not used in this work as fluid-solid interaction is more precise to describe the phenomena generally related to the two-phase, two-field coupling, that is not tied to specific characteristic geometrical shapes of the solid.

On the fluid-solid interface a no-slip condition between fluid and solid is presumed as well as the balance of tractions needs to hold

$$\frac{\partial \boldsymbol{d}^{\mathrm{S}}}{\partial t} = \boldsymbol{v}^{\mathrm{F}} \quad \text{on } \Gamma^{\mathrm{F,S}} \times (0, T), \tag{2.28}$$

$$\boldsymbol{h}_{\Gamma}^{\mathrm{S}} = -\boldsymbol{h}_{\Gamma}^{\mathrm{F}} \quad \text{on } \Gamma^{\mathrm{F,S}} \times (0, T). \tag{2.29}$$

The fluid domain needs to maintain compatibility to the solid domain

$$\boldsymbol{d}^{\mathrm{G}} = \boldsymbol{d}^{\mathrm{S}} \quad \text{on } \Gamma^{\mathrm{F,S}} \times (0, T). \tag{2.30}$$

In Paper A further physical models for biofilms are described. Importantly those are a poroelastic [31] approach to biofilm modeling [91] and the coupling to a fluid flow [1]. The approach towards nutrient distribution [98] in a biofilm growth model [28] are also presented therein.

2.4 Numerical modeling

For the solution of the initial and boundary value problems summarized in this chapter and the further ones described in Paper A the *finite element method* (FEM) is used [52, 100] for solid [11, 99] and fluid fields [101]. As stated above the equations are inherently nonlinear and therefore nonlinear FEM is employed [97]. FEM is the method of weighted residuals. After formulation of the initial and boundary value problem in the so-called strong forms, as presented in this chapter The next step is to formulate so-called *weak forms*. There the presented *strong forms* of the equations are ordered into a residual form and weighted with arbitrary continuous weighting functions and integrated over the whole domain and boundaries. In the next step a spatial discretization takes place and a finite set of weighting and ansatz functions for the field equations is found on the finite *elements* of the spatial discretization with explicit *degrees of freedom* for the primary variables at the *nodes*. During this work linear ansatz and weighting functions are employed. It is common practice to use higher *polynomial order* especially dealing with more complex fluid field solutions. The spatial discretization allows for an integration of the weak form on all domain and boundary elements as the weighting and ansatz functions are known and a system of equations can therefore be formulated for the primary variables at the nodes. As the described equations are nonlinear the further step of linearization for the degrees of freedom needs to be done. In the models used for this work the physical problem is further discretized in time. This gives a finite number of timesteps for which a suitable *time integration scheme* needs to be employed. In this work the time integration of choice is the *one-step-theta* method, where a user specified parameter Θ is chosen to weigh contributions of the new timestep. As a fluid problem is always part of a fluid-biofilm interaction modeling, a suitable *fluid stabilization* needs

to be used. Further the resulting system of equations can become big, depending on the spatial discretization size, such that a suitable *solver* must be found.

The used ALE approach has the advantage that one spatial discretization can be found for the fluid domain and the degrees of freedom stay the same over the whole solution period. This leads to the ALE approach being a very efficient choice. The ALE approach used in this work is a *monolithic* FSI method, which means that all degrees of freedom, namely solid displacements, fluid velocities and pressures and the fluid domain displacements are solved in the same system of equations at once. This has proven to be a good choice in biomedical applications [62]. The moving fluid domain in an ALE approach further brings the disadvantage that the unphysical domain displacement field needs to be solved and if no solution can be found, the whole simulation needs to be aborted. This is part of the demonstrational examples in Paper B , where several simulations could not be solved, if too high fluid domain distortions were involved. This is the immanent danger, when using the ALE approach for inverse analysis with soft materials, e.g., biomechanical materials, as soft materials undergo high displacements and therefore lead to high fluid domain deformations, that can lead to failing forward simulations. Nevertheless, if no contact phenomena occured in the modeled experiment, the ALE approach is the most efficient and therefore it was used for demonstrating the inverse analysis strategies developed in this work. To circumvent ALE specific problems related to high fluid domain distortions, fixed grid approaches as , e.g., CutFEM based FSI [77, 78] can be used. A CutFEM approach was also used in Paper A for a poroelastic modeling approach [1, 5]. Using the CutFEM approach, even changes in the biofilm topologies including self-contact and contact scenarios can be modeled [2, 3].

2.5 Modeling of flow cell experiments with biofilms

The inverse analysis approaches presented in this work focus on so-called flow cell experiments (e.g. see categorization of experiments [24]). In this type of experiment a biofilm is grown in a flow cell and then tested with a varying load via controlled fluid inflow into the flow cell [20, 44]. Then the biofilm geometry in the fluid channel is scanned using optical coherence tomography (OCT) [93, 94] for the unloaded and potentially multiple loaded states. OCT has proven to be well suited for the mesoscale structure and volumetric features of biofilms [94]. In general because of the inhomogeneuos structure of the biofilms and only limited penetration depth of OCT this will result in a potentially three-dimensional greyscale scan of the biofilm channel. The focus in such flow cell experiments is laid on the deformation of the biggest and best pronounced patch in the channel. A first approach for deterministic determination of a single material parameter with a linear continuum mechanical approach [72] has proven the concept of using continuous fluid-solid interaction models of flow cell experiments for this purpose.

In the past, the modeling of biofilm streamers has been a topic of interest [98]. Biofilm streamers are filaments of biofilm often attached to a bigger aggregate that are free to oscillate in the fluid flow in a flow cell [81]. The influence of shape characteristics of such oscillations was studied in [85] and additionally the nutrient distribution in such an oscillating state in [84, 98]. In general inverse analysis is also possible with such streamer parts of biofilms, but a different type of comparative measure based on the characteristics (e.g. frequency and magnitude) of the oscillations needs to be defined. In current work the focus is set on the analysis of quasi steady deformations of biofilm patches in flow cell experiments. The imaging of streamers in sufficient quality must also still be proven feasible. To the authors current knowledge a high enough temporal and spatial resolution of three-dimensional OCT scans is not practicable.

The modeling of biofilm physics is not limited to the aspects shown in this work. The modeling of biofilm growth has been shown in [28] and also used in this work. There have also been earlier, other approaches to biofilm growth rather focussing on the nutrient distribution and consumption alone [73] and potentially considering a heterogeneous perspective on growth [6]. The consideration of detachment effects has also been introduced in biofilm modeling [7, 22]. Biofilms have alternatively been modeled using multi-phase mixture models [87] exposed to fluid flow. It was shown that the environment of growth has a great influence on biofilm structure [79] and therefore a heterogeneous, potentially layered structure can be assumed. Biofilms have also shown to have viscoelastic [59], and porous properties [9].

As the methods for inverse analysis developed in this work are solely based on a geometric evaluation of the deformation, the actual solid mechanical model (e.g. viscoelastic, porous, heterogeneous) is to be chosen individually and further progress in biofilm modeling can be transferred to the forward model in an inverse analysis. The individual choice is strongly influenced by the quality and amount of data available, as e.g. for viscoelastic effects, a time series of images in the relevant short timescale is required.

3 Inverse analysis

The term inverse analysis is related to the solution of *inverse problems*. The analysis of physical problems generally includes finding a physical model, that includes the defining parameters in the physical laws and boundary conditions. In the context of inverse analysis the physical model is also called *forward model* $\mathfrak{M}$. The finding of a suiting model becomes especially intricate when the outcome of a modeled experiment is observed. Inverse analysis includes a further step that is finding an inverse model of how to compare model results to experimental observations and what can be concluded from such a comparison [86]. Previous chapter 2 gives a short introduction of how the physical modeling of biofilms can be done. In this chapter the focus is set on the second task. Nevertheless, it is clear that the inverse problem is strongly influenced by the choice of forward model.

The setting of inverse problems can be motivated from different perspectives. A few very general and non-exhaustive, non-unique inverse problem settings are introduced. First a *reconstruction problem* is set if the input parameters are known, observations were made, but the forward model is yet to be found. If a good model is already available and a certain model outcome shall be designed by an unknown, specific parameter choice, the inverse problem can be called *design problem*. The standard case in this work is that experimental observations were made, the physical model is selected and the choice of parameters to explain the observations is sought after. This type can be called *identification problem*. The term *parameter estimation* is also used. Or as it was labeled in Paper B the term *calibration problem* characterizes this type of inverse problem.

First, some basic terms in inverse problems are introduced, that are used in the publications and the following in section 3.1. The contributions in Paper A and Paper B regard the inverse analysis approach in biofilm flow cell experiments. The number of two publications in a wider sense mirrors the general situation that there are two possible approaches towards inverse problems. First as in Paper A and section 3.2 the *deterministic* approach is followed. Secondly as in Paper B and section 3.3 the *statistical* or *probabilistic* approach is used.

3.1 Basic terminology

Some recurring terms and notation will be used consequently and is therefore summarized here in form of an overview.

Forward model The forward model $\mathfrak{M}$ is the model applied for explaining the physical relations in the regarded experiments. In this work a continuous, coupled fluid-biofilm interaction model as described in chapter 2 is used exclusively.

(Input) parameters The input parameters $\boldsymbol{x}$ of an inverse problem are the degrees of freedom in the inverse analysis, that are varied to find an optimum. A solution for $\boldsymbol{x}$ is a solution of the inverse problem. In a statistical approach the probability density distribution over $\boldsymbol{x}$ of the model representing the data, is the solution of the problem. The vector $\boldsymbol{x}$ is often stated to live in the input space. The number of parameters n_{x}, which is also the number of components in $\boldsymbol{x}$ is called the dimension of the inverse problem.

Uncertain parameters The model can, additionally to the input parameters $\boldsymbol{x}$, depend on uncertain parameters $\boldsymbol{\theta}$. These uncertainties $\boldsymbol{\theta}$ can, e.g., represent uncertain boundary conditions, that are not known as a singular, exact value, but are prone to uncertainty. Ideally the probability distributions can be determined for the values $\boldsymbol{\theta}$. For the sheer numerical approach both $\boldsymbol{x}$ and $\boldsymbol{\theta}$ are parameters in the model, but they differ in their relevance and interpretation.

Spatio-temporal coordinates Spatio-temporal coordinates $\boldsymbol{c}$ are introduced to specify time and location in experiment and forward model in which the biofilm geometry is compared against each other. Comparisons should only be made for the same $\boldsymbol{c}$.

Observations Observations $\boldsymbol{y}_{\mathrm{obs}}$ are made from the experiment. The composition of $\boldsymbol{y}_{\mathrm{obs}}$ is depending on the type of comparison between observations and forward model. If more than one coordinate $\boldsymbol{c}$ in the comparison exists, a further specification as $\boldsymbol{y}_{\mathrm{obs},\boldsymbol{c}}$ including the index $\boldsymbol{c}$ is necessary.

Distance measure It is one central component in Paper A and Paper B to discuss how the comparison between experimental observation and forward model results can be done. This is widely summarized as a discrepancy or distance measure $\mathfrak{D}$. With the terminology and notation in this section it can be written $\mathfrak{D} = \mathfrak{D}(\boldsymbol{y}_{\mathrm{obs},\boldsymbol{c}}, \mathfrak{M}(\boldsymbol{x}, \boldsymbol{\theta}, \boldsymbol{c}))$ as a very general term for the distance measure.

Training data In the probabilistic case in Paper B a surrogate over the results of the forward model evaluations is built. The training data consist of one forward model evaluation and the comparison to the experimental observations each for n_{train} simulation runs.

3.2 Deterministic approach

The deterministic approach to inverse analysis is labelled as such in this work as the distance measure $\mathfrak{D}$ is directly used to define the *objective function* in terms of a least-squares problem. The minimum of the objective function with respect to the input parameters $\boldsymbol{x}$ is then found by deterministic optimization [58, 70]. The Levenberg-Marquardt method for optimization followed in Paper A is based on the works of Levenberg [64] and Marquardt [65] and explained in [67] as a single method.

Continuous efforts for inverse analysis at LNM [10, 18, 75, 88] have led to the version of the Levenberg-Marquardt optimization as it is used in this work. In the deterministic approach efficiency is manifested in the low number of iterations. As the number of iterations corresponds to the number of forward model evaluations the optimizing approach takes to find the optimal parameters. Levenberg-Marquardt optimization has also been used for analysis of tumor models [61] and nonlinear cardiac models [71].

3.2.1 Paper A: Levenberg-Marquardt approach

Inverse analysis of material parameters in coupled multi-physics biofilm models

Harald Willmann, Wolfgang A. Wall

Summary

This paper presents a method for inverse analysis that is centered around a Levenberg-Marquardt optimization of an objective function based on a geometric comparison of a deformed biofilm shape and forward model evaluations. The fluid-biofilm interaction models are used to model the setup of flow-cell experiments.

In the first part the systems of equations for a pure fluid-solid interaction model in ALE formulation is presented. Then the model is extended with a scalar transport model that is used as a dummy nutrient including a Monod kinetic consumption of the nutrient in the biofilm domain. Then a phenomenological model for surface growth and erosion is based on resulting nutrient fluxes and surface tractions on the fluid-biofilm interface. Nutrient inflow into the biofilm domain causes growth at the surface and the normal

and tangent component of the interface tractions individually erode the biofilm. Then the system of equations for a coupled fluid-poroelastic biofilm model are presented. The porous solid is itself modeled as a homogenized mixture of a nonlinear solid and a Darcy flow of a fluid phase. The two phases themselves are coupled, as the deformation has direct influence on the local porosity and therefore is linked to the porous-fluid pressure.

In the next step it is described how the comparison of the forward model outcome to experimental observations is made. As a distinction of material points is assumed not to be possible from OCT scan data, a solely shape based comparison is proposed. The objective function for optimization is defined via a norm of a vector of local interface distances. The Levenberg-Marquardt optimizer with an update strategy of the regularization and a certain set of convergence criteria are presented. The gradient information of the objective function needed for optimization is determined in a finite difference approach. The algorithm therefore needs one more than the number of parameters $n_{\mathrm{x}} + 1$ of forward model evaluations per iteration for the approximation to the gradient in all directions.

For the examples section reference results were generated with one forward model evaluation respectively and the addition of Gaussian noise to the reference result. For the pure FSI model, the two parameters of Young's modulus and Poisson's ratio in a hyperelastic Saint-Venant Kirchhoff material model were optimized. The parameter results of the inverse analysis were compared for different levels of Gaussian noise. In a second example a heterogeneous model consisting of three subdomains for the solid biofilm model was analyzed. Then the porosity and Young's modulus with a Neo-Hookean material model of the porous skeleton were analyzed. In the last example the three growth parameters of the presented surface growth model were analyzed. All examples were started with multiple initial guesses for the parameters and it showed that success of the method is dependent on the initial guess. With the help of the examples it was shown, that the mentioned key parameters of the biofilm models in the coupled fluid-biofilm interaction models could be analyzed up to a moderate level of noise on the data with the presented type of distance measure.

Contribution

Contribution section was published with the original full text version of the paper. "HW implemented the inverse analysis approach, run the simulations, prepared the figures and primarily drafted the manuscript. WAW worked out the general conception of the project. Both authors contributed to the discussion of results and prepared and approved the final manuscript."[96]

Reference

[96] H. Willmann and W. A. Wall. "Inverse analysis of material parameters in coupled multi-physics biofilm models". In: *Advanced Modeling and Simulation in Engineering Sciences* 9.7 (2022). DOI: 10.1186/s40323-022-00220-0

Full text is appended as Paper A.

3.2.2 General modularity of deterministic approach

The presented algorithm for deterministic inverse analysis includes a set of choices. The only requirement is that a decision for all components of the approach must be made. The individual steps can be interchanged modularly. The generic method is visualized in Figure 3.1. By modularity it is meant that, e.g., the forward model $\mathfrak{M}$

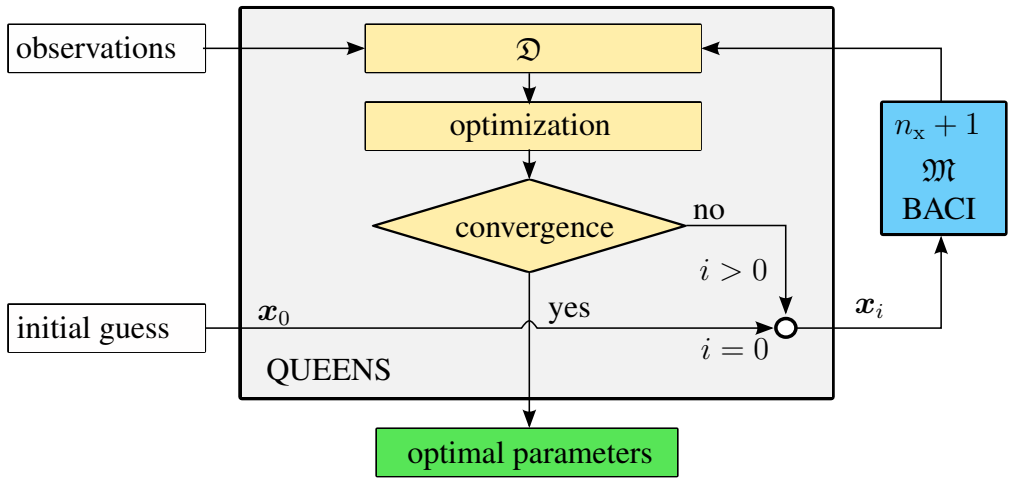

Figure 3.1: Deterministic inverse analysis in QUEENS with BACI as used in Paper A.

can be exchanged, as it was done in Paper A. Alternatively also the optimizer can be changed to, e.g., L-BFGS-B. Finally, also the distance measure can be changed to, e.g., closest point projection distances at every interface node of the forward model.

A further aspect shown in Figure 3.1 is the iterative evaluation of the forward model. This has the major implication that if one forward model evaluation fails, the iterations break and no solution can be found. By the iterative approach and independent convergence criterion the total amount of forward model evaluations, which are expected to be costly, are unknown beforehand. With this approach, because of the iterative character, at most $n_x + 1$ evaluations can be run in parallel.

3.3 Statistical approach

The statistical approach to inverse analysis [55, 86] gives more flexibility to an inverse analysis. The goal of a statistical inverse analysis is to find a probability distribution of how probable it is that a certain combination of values of the input variables $\boldsymbol{x}$ combined with the forward model $\mathfrak{M}$ are the best to explain an experimental observation. The determination of such probability densities over the input parameters offers a deeper interpretation of interactions between the parameters in the inverse problem and therefore goes far beyond the determination of one fixed combination of parameter that fits best. A statistical approach further allows the incorporation of prior information, influence of uncertain inputs and a probability model tailored to the expected shape of noise in the data as shown in Paper B.

For probabilistic inverse analysis a valuable contribution was done at TUM by Kehl [56, 57]. In his works, a detailed *variational Bayes* approach to inverse analysis was developed and implemented in the software BACI [8]. Especially a certain strategy for the comparison of interfaces in terms of *surface currents* was revisited from the literature [53, 89] and introduced for inverse problems of growth of *abdominal aortic aneurysms (AAA)*. This measure is also employed in Paper B for the comparison of biofilm surface shapes. Further, the joint development efforts for the python software QUEENS [15] facilitated the development of a robust, flexible implementation of the method presented in Paper B. A Bayesian approach has also been applied to models of urea hydrolysis by E.coli biofilms in [54].

To use *Bayes' theorem* for the inverse analysis of mechanical problems a short, general introduction to the concept of probability densities follows in the next subsection.

3.3.1 Concept of probability density

In the following, the basic concept of probability density and some basic properties and terms are introduced, so they can be addressed in the discussion. The concepts can be found in the literature about probability theory (e.g. [12, 16]) or the basics in applied literature (e.g. [19, 74]).

Probability densities constitute the continuous distribution of probability over a certain variable. So that the probability, that the variable lies in a certain interval can be written as an integral

$$P\left(x \in (a,b)\right) = \int_a^b p\left(x\right) \mathrm{d}x. \tag{3.1}$$

In simpler means $P\left(x \in (a,b)\right)$ represents the probability of the statement $(x \in (a,b))$ to be true, so for x to lie in an interval from a to b. Probability densities are expected to

have positive values in the whole range of x and to integrate to one

$$p(x) > 0, \tag{3.2a}$$

$$\int_{-\infty}^{\infty} p(x)\,\mathrm{d}x = 1. \tag{3.2b}$$

The knowledge of the density allows to compute the *expectation* $\mathbb{E}$ of x as

$$\mathbb{E}[x] = \int_{-\infty}^{\infty} xp(x)\,\mathrm{d}x. \tag{3.3}$$

The expectation is also called *expected value* or *mean*. The *variance* $\mathbb{V}$ can further be computed as

$$\mathbb{V}[x] = \int_{-\infty}^{\infty} (x - \mathbb{E}[x])^2\, p(x)\,\mathrm{d}x = \mathbb{E}\left[(x - \mathbb{E}[x])^2\right]. \tag{3.4}$$

The *standard deviation* σ is the square root of the variance

$$\sigma = \sqrt{\mathbb{V}[x]}. \tag{3.5}$$

In the case of a vector of variables $\boldsymbol{x}$ the *expectation* and *covariance* are computed accordingly

$$\mathbb{E}[\boldsymbol{x}] = \int_{-\infty}^{\infty} \boldsymbol{x}p(\boldsymbol{x})\,\mathrm{d}\boldsymbol{x}, \tag{3.6a}$$

$$\mathbb{COV}[\boldsymbol{x}, \boldsymbol{x}] = \mathbb{E}\left[\{\boldsymbol{x} - \mathbb{E}[\boldsymbol{x}]\}\{\boldsymbol{x}^\mathsf{T} - \mathbb{E}[\boldsymbol{x}^\mathsf{T}]\}\right] = \mathbb{E}\left[\boldsymbol{x}\boldsymbol{x}^\mathsf{T}\right] - \mathbb{E}[\boldsymbol{x}]\,\mathbb{E}\left[\boldsymbol{x}^\mathsf{T}\right]. \tag{3.6b}$$

Therein the expectation is a vector of length n_x and the covariance is a matrix of shape $n_\mathrm{x} \times n_\mathrm{x}$. With the introduction of a vector of variables, the probability density of two combined variables $\boldsymbol{x}, \boldsymbol{y}$ can be defined as the *joint probability density* $p(\boldsymbol{x}, \boldsymbol{y})$. In short some basic principles of probability theory of continuous probability densities [12, 19] namely the product and sum rule of probability are revisited, as they are frequently used and help understand the probabilistic approach. For the joint density, the continuous sum rule states

$$p(\boldsymbol{x}) = \int_{\boldsymbol{y}} p(\boldsymbol{x}, \boldsymbol{y})\,\mathrm{d}\boldsymbol{y}. \tag{3.7}$$

This integral is sometimes called marginalization of the joint distribution over $\boldsymbol{y}$. Further the *conditional probability density* $p(\boldsymbol{x}|\boldsymbol{y})$ can be explained with the joint as

$$p(\boldsymbol{x}|\boldsymbol{y})\,p(\boldsymbol{y}) = p(\boldsymbol{x}, \boldsymbol{y}). \tag{3.8}$$

The conditional $p(\boldsymbol{x}|\boldsymbol{y})$ can be read as the probability density for $\boldsymbol{x}$ *given* $\boldsymbol{y}$. It describes the probability density over $\boldsymbol{x}$ given that $\boldsymbol{y}$ is already fixed. In words (3.8) reads as the probability density of $\boldsymbol{x}$ given $\boldsymbol{y}$ times the probability density of $\boldsymbol{y}$ itself is the probability density of the joint $p(\boldsymbol{x}, \boldsymbol{y})$. (3.8) is also called the product rule of probability.

3.3.2 Bayesian approach to inverse analysis

With the introduced terms above, the probabilistic computations in the inverse analysis approach can be concluded. The central equation in the probabilistic approach to inverse analysis is *Bayes theorem* [76]. With two vectors of variables $\boldsymbol{x}, \boldsymbol{y}$ it can be formulated as

$$p\left(\boldsymbol{x}|\boldsymbol{y}\right) = \frac{p\left(\boldsymbol{y}|\boldsymbol{x}\right) p\left(\boldsymbol{x}\right)}{p\left(\boldsymbol{y}\right)}. \tag{3.9}$$

In this form Bayes theorem looks like a simple consequence of (3.7) and (3.8), but it is very powerful and versatile for the application in inverse analysis. The following Bayes formulation is the exact form presented in Paper B, but it is compared to the general form in (3.9) here as a prerequisite to the application

$$\underbrace{p\left(\boldsymbol{x}|\boldsymbol{y}_{\mathrm{obs}}\right)}_{\text{posterior}} = \frac{\overbrace{p\left(\boldsymbol{y}_{\mathrm{obs}}|\mathfrak{M}\left(\boldsymbol{x},\boldsymbol{c}\right)\right)}^{\text{likelihood}} \cdot \overbrace{p\left(\boldsymbol{x}\right)}^{\text{prior}}}{\underbrace{\int p\left(\boldsymbol{y}_{\mathrm{obs}}|\mathfrak{M}\left(\boldsymbol{x},\boldsymbol{c}\right)\right) \cdot p\left(\boldsymbol{x}\right) \mathrm{d}\boldsymbol{x}}_{\text{evidence}}} \propto \underbrace{p\left(\boldsymbol{y}_{\mathrm{obs}}|\mathfrak{M}\left(\boldsymbol{x},\boldsymbol{c}\right)\right) \cdot p\left(\boldsymbol{x}\right)}_{\text{unnormalized posterior}}. \tag{3.10}$$

The *posterior* $p\left(\boldsymbol{x}|\boldsymbol{y}_{\mathrm{obs}}\right)$ is the solution of a Bayesian inverse problem. It represents the probability density over the input, given that the data $\boldsymbol{y}_{\mathrm{obs}}$ has been observed in experiments. In the posterior it is possible to find the so-called *maximum a posteriori (MAP)* which is that input coordinate, that leads to the highest posterior density. This MAP estimate is the direct correspondence to the result of a deterministic approach to inverse analysis. The *likelihood* is the probability that observed data fits the given forward model $\mathfrak{M}$ for a specific choice of parameters $\boldsymbol{x}$ at the corresponding coordinates $\boldsymbol{c}$. Likelihood modeling should be done according to the shape of the expected noise in the data. The evaluation of the likelihood is the costly part in this approach as for every point to evaluate it, a forward model must be solved and the result must be compared to the observation data. Prior information on the input parameters can be used in the form of *prior* distributions $p\left(\boldsymbol{x}\right)$ that quantify the distributions with which the parameters are expected to be distributed. The prior quantifies knowledge about the parameters in a probability density. The easiest assumption is a uniform prior on an interval. Combined the likelihood and prior build the *unnormalized posterior*. The likelihood as given in (3.10) is not a probability density in $\boldsymbol{x}$, but in $\boldsymbol{y}_{\mathrm{obs}}$ and that is why the integral, the *evidence* is in general not equal to one. With the application of *sequential Monte Carlo (SMC)* methods [26, 27, 32–34] the explicit integration of the evidence can be circumvented, as SMC can be evaluated with the unnormalized posterior and the normalization is transferred to the *particle approximation* of the method. In Paper B a specific adaptive version of SMC [60] is used.

3.3.3 Paper B: Bayesian calibration approach

Bayesian calibration of coupled computational mechanics models under uncertainty based on interface deformation

Harald Willmann, Jonas Nitzler, Sebastian Brandstäter, Wolfgang A. Wall

Summary

This paper presents a method for Bayesian calibration under uncertainty based on a Gaussian process (GP) surrogate for the likelihood. The generation of a surrogate makes efficient use of the forward model evaluations. The method results in a Sequential Monte Carlo (SMC) particle approximation of the posterior.

The setting of biofilm flow cell experiments is described briefly and the modeling of such experiments using a monolithic ALE approach for fluid-solid interaction is introduced. Inverse analysis under uncertainty is introduced with the general expression of Bayes' theorem for calibration under uncertainty and the respective variables involved. For the application of a Bayesian approach, the model of a Gaussian static likelihood is introduced. For the evaluation of the likelihood three different suitable distance measures for the comparison of deformed biofilm shapes are introduced. First the euclidean distance at measurement points is shortly revisited. As a second measure closest point projection distances are briefly introduced. The third measure formerly used as discrete surface currents in the referenced inverse analysis literature is explained using the flexible framework of reproducing kernel Hilbert spaces (RKHS). In the RKHS approach a squared exponential kernel is briefly presented and later used. The concept of SMC particle approximation of the posterior and integration of statistics on the posterior is briefly introduced. The setup and training of a GP regression model with a Matérn 3/2 kernel is introduced and used as a regression model for the logarithmic likelihood in the Bayesian calibration approach.

The numerical examples are created with a forward model of a general fluid-biofilm interaction model of an arbitrary shape. As a comparison, a forward model result with ground truth values for the parameters is generated and used as artificial observation data. At first the three surface distance measures are compared in their resulting shape of the likelihood surrogate for a fixed high number of forward model evaluations n_{train}. The general shape of the likelihood has similar characteristics in all three cases. The likelihood is high in a narrow, inclined, curved band in the two-dimensional input space and peaks around the ground truth. Qualitatively the RKHS based distance measure results in the most expressive likelihood shape. In a study over the number of training points n_{train} it shows that $n_{\text{train}} \approx 200$ are enough to represent the general shape of the posterior as well as the maximum a posteriori (MAP) estimate for a two parameter

example. For a more detailed posterior it was shown that further increase in n_{train} results in a smoother, more detailed shape. It is demonstrated how failing forward model simulations only increase the uncertainty of the surrogate, but do not hinder the overall calibration. Then the influence of different assumptions towards the prior distributions and assumptions to the uncertainty of specific boundary conditions on the posterior is analyzed in different approximated posteriors. In a final, heterogeneous example the approach is demonstrated with six parameters, one uncertain boundary condition and an addition of Gaussian noise to the ground truth simulation. This setting results in a complex high-dimensional posterior, which is interpreted from different perspectives. The influence of the individual parameters to the results is analyzed qualitatively.

Contribution

Contribution section was published with the original full text version of the paper. "HW implemented the workflow in QUEENS, run the simulations and generated the figures. HW and JN concepted and discussed the approach. SB implemented the SMC integration and contributed to the discussion of its application. WAW concepted the general outline of the project. All authors read and approved the manuscript."[95]

Reference

[95] H. Willmann, J. Nitzler, S. Brandstäter, and W. A. Wall. "Bayesian calibration of coupled computational mechanics models under uncertainty based on interface deformation". In: *Advanced Modeling and Simulation in Engineering Sciences* 9.24 (2022). DOI: 10.1186/s40323-022-00237-5

Full text is appended as Paper B.

3.3.4 General modularity of statistical approach

This Bayesian calibration approach offers some choices that have to be made. The very general, modular structure of the generic method is depicted in Figure 3.2. As already discussed in Paper B the steps of the generic method can be exchanged by better fitting solutions if further potential for improvement is identified.

The distribution of training points can also be done with, e.g., a Latin-Hypercube approach or may be based on the prior information, to be more efficient overall, if more simulations are carried out with highly probable parameter combinations and fewer with less relevant parameter combinations. The method works as presented with any kind of forward model, as the comparison of the deformation is purely geometric. The type of distance measure can be chosen freely, as long as it fits in the likelihood model.

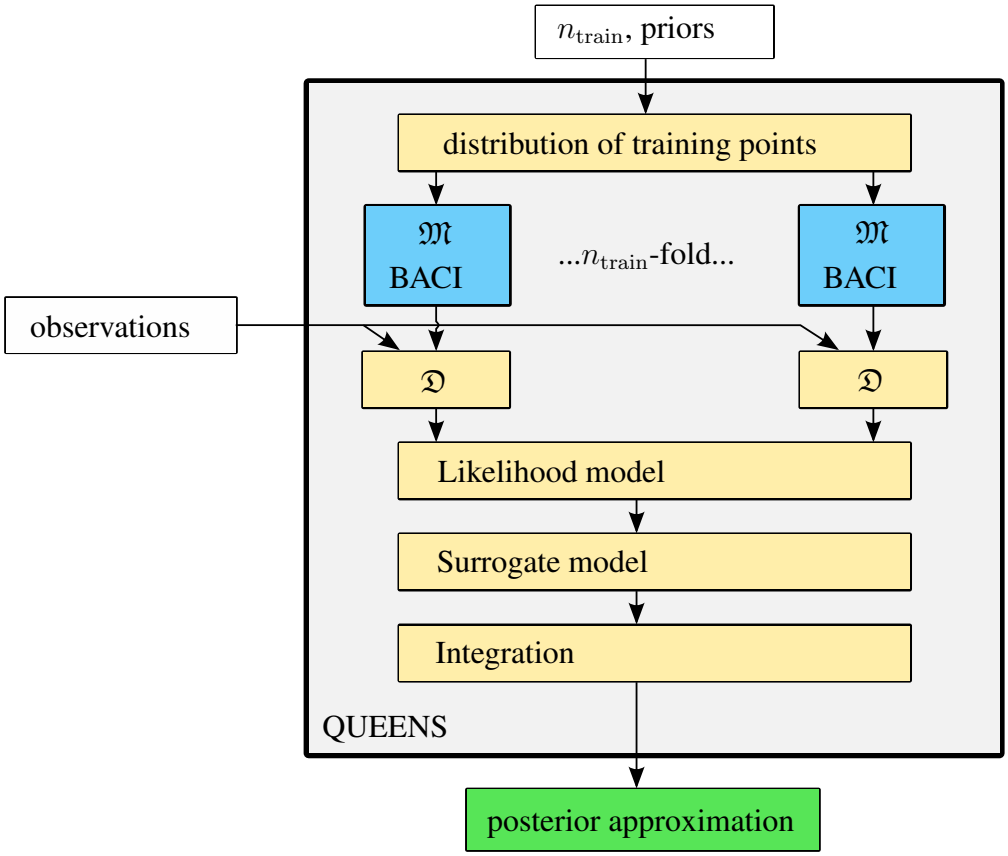

Figure 3.2: Efficient Bayesian calibration with regression model in QUEENS with BACI as used in Paper B.

Different likelihood models can be used if anticipated error from experiments is different. If the magnitude of noise is unknown, also a non-static likelihood approach can be used, where the variances in the likelihood model are optimized with the data. The construction of a surrogate model can also be left out and replaced by forward model evaluations in the SMC approach if the forward model is affordable to evaluate. If a surrogate model for the likelihood is used that needs to fit the application. That means the choice of kernel and determination of kernel parameters of a GP surrogate should be tuned to the data acquired. The SMC along with the particle approximation are used for an approximation of the posterior. Other methods like pure Markov Chain Monte Carlo (MCMC) approaches can be used alternatively for integration of the evidence.

4 Discussion

In this chapter the necessary assumptions for inverse analysis are revisited and from that a general discussion of the applicability of the approaches is deduced.

4.1 Assumptions for inverse analysis of flow cell experiments

The first and most significant block of assumptions is made towards forward modeling. It is clear that, the better the forward model represents the experiment, the more meaningful the inverse results are. In the examples shown in the publications an isotropic, homogeneous, hyperelastic material model is used for the biofilm. A prototype heterogeneous material model shares those assumptions in a piecewise manner. That means the same material model with different parameters is used for each subdomain individually. It is assumed that this continuum mechanical modeling of biofilms can represent biofilm deformation behavior that is observed in experiments. Especially that means that no microscopic structure needs to be detailed in the modeling of the experiment. So in general a phenomenological approach to material modeling is used. That enables the application of established continuum material models for the inverse analysis of how biofilms can be approximated by those.

For the modeling of flow cell experiments the dominant biofilm patch is analyzed and potential smaller patches or thin ground layers of biofilm are neglected. If no patches are formed but just a floor layer of biofilm develops, presented discrepancy measures are not expected to offer much insight. This is a natural restriction by means of OCT measurement, as remote regions of the channel including inflow and outflow pipes cannot be measured and therefore some limits have to be drawn. In the reduction of the experiment setup to two dimensions a strong assumption towards the symmetry of the patch and therefore the fluid flow has to be made. With the plain strain assumption used in the forward model no out-of-plane deformation can be considered. If the experimental data of OCT consists of spatially planar scans only and in fact the biofilm is deformed out of plane, the inverse analysis can not be done with a two-dimensional forward model. As an improvement, e.g., combinations of planar deformation data and an initial three-dimensional scan and further a three-dimensional forward model could enable inverse analysis in this scenario.

It is known that detachment processes play a significant role in biofilm analysis. If detachment processes are influencing the experimental observations a forward model must include them. Overall it must be recommended to use as much of the data as possible in the best level of detail obtainable and as accurate prior knowledge as available and use a forward model that is modeling all observed physical effects. The application for the inverse analysis result should always be kept in mind when building the forward model. If the parameters that result from an inverse analysis are later used for predictions of biofilm behavior, it is very beneficial if the model used for predictions is already used as a forward model in inverse analysis. That is therefore recommended.

For all approaches, the quality of the measurement data is crucial. Additionally to the bare acquisition of OCT scans, also some strategy for image segmentation needs to be employed. This means that a strategy needs to be defined to determine if a spatial point in a flow cell is occupied by biofilm or not. That must be concluded from a potentially noisy set of grayscale information on a spatial grid obtained from an OCT scan. The topic of image segmentation is not covered in this work. A definition of a suitable approach in segmentation is the logical next step to analyzing raw experimental data. The keen eye of the experimenter or analyst is always a valuable tool to do some segmentation. Experts in biofilm experimentation and OCT imaging are capable to estimate from a scan where the fluid-biofilm interface is located. For the purpose of this work it is assumed that a suitable image segmentation is done and the observation data is the result of that.

4.1.1 Assumptions in deterministic approach

For the deterministic approach to inverse analysis, the analyst has to fix his assumptions towards biofilm modeling and characteristics of the objective function. That includes the finding of a good initial guess. The deterministic approach is well suited if the forward model is assumed to be close enough to reality so that the shape of the objective function is not altered by unknown, not modeled influences to the experiment or too much measurement noise. It is assumed that one distinct optimum exists in the objective function and that it is the global optimum. Further the initial guess must be good enough to be able to find the global optimum. In gradient based optimizers the existence of further, local optima is hindering as they may also be found as the result of the analysis without any hint towards the global optimum. It is assumed that all analyzed parameters are actually significant to the biofilm deformation. If this is not true, the optimizer will just iterate in this degree of freedom and the result is only influenced by all other parameters. From the iteration steps it can be guessed which parameters have what kind of influence on the objective function. Nevertheless, the single point optimum is the only result from a deterministic inverse analysis.

4.1.2 Assumptions in statistical approach

For a Bayesian calibration approach there is a different set of assumptions. The prior distributions as well as the distributions of uncertain parameters must be quantifiable. One kind of informative prior is a uniform prior on an interval. But also for uniform priors a posterior unequal to zero can only be found inside the interval of the uniform distribution. In other words you cannot find probability mass, where you don't look for it. And by fixing prior assumptions you directly influence your result. The likelihood model is assumed to fit to the expected shape of measurement error or noise. By building a GP regression model on the likelihood a certain level of continuity is assumed with the choice of the kernel functions. A comparative single value for all parameters is the MAP estimate that corresponds to the single point estimate that results from the deterministic approach. But also other statistics of the posterior or of marginals of the posterior can be evaluated as, e.g., the expectation, the covariance or the shape of percentiles.

4.2 Comparison of approaches

In the whole field of inverse analysis it is clear that on the one hand the type of forward model is strongly influencing not only the results, but also which approach is favorable. On the other hand, the type of experiment and type of data retrieved from it are expected to have high influence on both results and the question of the best inverse analysis approach. Before deciding for a deterministic or probabilistic approach it should be considered if the advantages of a statistical approach can be played out. This means that questions if the error structure is known if there is known uncertainty about boundary conditions, or if there is prior knowledge available about the parameters should be answered.

The deterministic approach as presented in Paper A gives a simple answer to what the choice of parameters in a selected forward model is that is fitting best to the data observed. If the forward model is well known and it is certain that the modeling corresponds well to the experiment the best fit might be all that is interesting to know. On the downside the approach does not allow further interpretation as, e.g., an estimation of how well another combination of parameter fits in comparison or even how relevant the individual parameters are for the quality of the fit. In presented examples in Paper A the deterministic approach needed only a small number of iterations to approach the optimum of the objective function. A low number of iterations and therefore low number of forward model evaluations is attractive in these approaches. Nevertheless, the exact number of forward evaluations is unknown a priori.

A big disadvantage of a deterministic approach is that if the forward model cannot be evaluated in every iteration, it simply fails and no result can be found. If the objective function is multimodal, i.e., more than one local optimum exists firstly the search path

may induce jumps and therefore the number of iterations increases and secondly when an optimum is found it is not clear if it is the global optimum. Further if the objective function is flat in some input regions, this can increase the number of iterations if the search path leads through those regions. An objective function becomes flat if there is little influence of the parameters towards its value. From all of the above it must be concluded that an initial guess should be available and should fit as well as possible.

The Bayesian calibration approach as presented in Paper B gives full control over the computational budget. The posterior result is more expressive, the more forward simulations are run. In this approach multimodality is not as critical as the forward simulations are distributed uniformly in the input space and therefore it is explored independently of the resulting posterior. The simulation results can then be compared globally and so the region of the global MAP can be narrowed down dependent on the distribution of the training points and their number. In between the training points there is room for higher posteriors than the value at the MAP estimate that can be found with limited n_{train}. By increasing n_{train}, the exploration of the input space can be improved. Potentially by adding more points, i.e. testing more parameter combinations, a new feature of the posterior is discovered. With the presented Sobol-sequence for the distribution of the training points more can be added to the analysis to improve the exploration of the input space. This is a special feature of the Sobol-sequence to be able to continue finding points that are well distributed, whereas their number does not have to be fixed initially. Usually for statistic approaches the necessary number of forward model evaluations is higher than with a fast converging deterministic approach, as the runs are distributed evenly in the input space.

A combination of both approaches can also be used to try and exploit the advantages of both. As the quality of the initial guess is crucial for the success of deterministic approaches they can be chosen in the high posterior regions of a preliminary Bayesian calibration approach. So the Bayesian approach serves with an overview and the capability to estimate if the found optimum is a global one and the deterministic approach is used to optimally exploit the experimental observation data to find the best fit. Nevertheless, if there is significant noise in the data this information of the optimal fit without a noise model becomes less expressive.

4.3 Conclusion

In this work and more precisely the appended articles two different approaches to inverse analysis of biofilms were presented. First a deterministic optimization approach is presented in Paper A and second a Bayesian calibration approach is presented in Paper B. The conditions for their application are discussed and compared.

With both approaches it was shown that a purely shape-based comparison of observed data and simulation results from fluid-biofilm interaction problems can be used

in an inverse analysis method and that the material parameters in different material and physical models can be analyzed. The necessary framework and steps for inverse analysis approaches have been demonstrated and the general modular composition in both approaches has been described.

4.4 Outlook

The logical next step is to apply the presented methods to real experimental data. Only in application, further tuning of the methods can be done and picking the right tools for all individual modules can be elaborated. It is encouraged to use three-dimensional scans of biofilms as well as possible, as the given methods allow that without limitation. The extension to viscoelastic material models is straight forward, only the comparison between experiment and forward model must be made for more than one spatio-temporal coordinate. The same can apply to more complex hyperelastic material models in which it will become necessary to compare more than one loaded state.

The finite element method, although it is the method of choice in this work is not the only method to construct a forward model. Other approaches like hybradizible Discontinuous Galerkin methods [63] or particle methods [42, 43] for the fluid equations in FSI could be used. Especially when it comes to a change in topology of the biofilm as in detachment, where a model for fracture is needed (e.g. [83]), or in self contact that can be modeled with CutFEM approaches like e.g. [4], the ALE method is limited. Nevertheless, the choice of forward model is open to the analyst and should be done in a way to represent the analyzed experiment best.

The presented approaches do not fit for every use case. Specifically if the dimension of the inverse problem, i.e. the number of parameters n_{x}, is much higher than in shown examples (i.e. roughly > 15) presented approaches are expected to reach their limits. Such problems can occur if the parameters are defined as random fields over the whole solid domains and therefore the heterogeneous structure of the material is sought after. Such problems are sometimes labeled *elastography* [40, 41]. In terms of FEM models for a biofilm the material parameters could be determined individually for each finite element. For higher dimensions other methods like Variational Bayes methods [56] become more efficient. If the forward model is too expensive for presented methods also Multi-fidelity approaches [69] can be used. Therein the *high fidelity* forward model is complemented by data retrieved from a much simpler *low fidelity* model, that is assumed to have at least a similar dependency on the parameters.

Bibliography

[1] C. Ager, B. Schott, M. Winter, and W. Wall. "A Nitsche-based cut finite element method for the coupling of incompressible fluid flow with poroelasticity". In: *Computer Methods in Applied Mechanics and Engineering* 351 (2019), pp. 253–280. DOI: 10.1016/j.cma.2019.03.015.

[2] C. Ager, A. Seitz, and W. Wall. "A consistent computational approach for general fluid-poroelasticity-structure-contact interaction problems". In: *Journal of Computational Physics* 441 (2021), p. 110450. DOI: 10.1016/j.jcp.2021.110450.

[3] C. Ager, B. Schott, A.-T. Vuong, A. Popp, and W. A. Wall. "A consistent approach for fluid-structure-contact interaction based on a porous flow model for rough surface contact". In: *International Journal for Numerical Methods in Engineering* 119.13 (2019), pp. 1345–1378. DOI: 10.1002/nme.6094.

[4] C. Ager, A. Seitz, and W. A. Wall. "A consistent and versatile computational approach for general fluid-structure-contact interaction problems". In: *International Journal for Numerical Methods in Engineering* 122 (2021), pp. 5279–5312. DOI: 10.1002/nme.6556.

[5] C. F. Ager. "Computational Methods for Fluid-Structure Interaction including Porous Media and Solid Contact". Dissertation. München: Technische Universität München, 2021. URL: http://nbn-resolving.de/urn/resolver.pl?urn:nbn:de:bvb:91-diss-20210310-1520849-1-3.

[6] E. Alpkvist and I. Klapper. "A Multidimensional Multispecies Continuum Model for Heterogeneous Biofilm Development". In: *Bulletin of Mathematical Biology* 69.2 (2007), pp. 765–789. DOI: 10.1007/s11538-006-9168-7.

[7] E. Alpkvist, C. Picioreanu, M. C. van Loosdrecht, and A. Heyden. "Three-dimensional biofilm model with individual cells and continuum EPS matrix". In: *Biotechnology and Bioengineering* 94.5 (2006), pp. 961–979. DOI: 10.1002/bit.20917.

[8] *BACI: A Comprehensive Multi-Physics Simulation Framework*. URL: https://baci.pages.gitlab.lrz.de/website/, Last accessed on 2021-16-06.

[9] D. de Beer, P. Stoodley, and Z. Lewandowski. "Liquid flow in heterogeneous biofilms". In: *Biotechnology and Bioengineering* 44.5 (1994), pp. 636–641. DOI: 10.1002/bit.260440510.

[10] A. Bel-Brunon, S. Kehl, C. Martin, S. Uhlig, and W. Wall. "Numerical identification method for the non-linear viscoelastic compressible behavior of soft tissue using uniaxial tensile tests and image registration – Application to rat lung parenchyma". In: *Journal of the Mechanical Behavior of Biomedical Materials* 29 (2014), pp. 360–374. DOI: 10.1016/j.jmbbm.2013.09.018.

[11] T. Belytschko, W. K. Liu, B. Moran, and K. Elkhodary. *Nonlinear finite elements for continua and structures*. John Wiley & Sons, 2014.

[12] D. Bertsekas and J. N. Tsitsiklis. *Introduction to probability*. Belmont: Athena Scientific, 2008.

[13] K. Besemer. "Biodiversity, community structure and function of biofilms in stream ecosystems". In: *Research in Microbiology* 166.10 (2015), pp. 774–781. DOI: 10.1016/j.resmic.2015.05.006.

[14] K. Besemer. "Microbial Biodiversity in Natural Biofilms". In: *Aquatic Biofilms: Ecology, Water Quality and Wastewater Treatment*. Caister Academic Press, 2016, pp. 63–88. DOI: 10.21775/9781910190173.04.

[15] J. Biehler, J. Nitzler, W. Wall, and V. Gravemeier. *QUEENS – A Software Platform for Uncertainty Quantification, Physics-Informed Machine Learning, Bayesian Optimization, Inverse Problems and Simulation Analytics: User Guide*. AdCoEngineering^{GW}. 2019.

[16] P. Billingsley. *Probability and Measure*. John Wiley & Sons, Inc., Hoboken, 2012.

[17] A. M. Birzle and W. A. Wall. "A viscoelastic nonlinear compressible material model of lung parenchyma – Experiments and numerical identification". In: *Journal of the Mechanical Behavior of Biomedical Materials* 94 (2019), pp. 164–175. DOI: 10.1016/j.jmbbm.2019.02.024.

[18] A. M. Birzle. "Experimental Analysis and Computational Material Modeling of Lung Tissue". Dissertation. München: Technische Universität München, 2019. URL: http://nbn-resolving.de/urn/resolver.pl?urn:nbn:de:bvb:91-diss-20190228-1449047-0-5.

[19] C. M. Bishop. *Pattern Recognition and Machine Learning*. Springer-Verlag New York Inc., 2011.

[20] F. Blauert, H. Horn, and M. Wagner. "Time-resolved biofilm deformation measurements using optical coherence tomography". In: *Biotechnology and Bioengineering* 112.9 (2015), pp. 1893–1905. DOI: 10.1002/bit.25590.

[21] M. Böl, A. E. Ehret, A. B. Albero, J. Hellriegel, and R. Krull. "Recent advances in mechanical characterisation of biofilm and their significance for material modelling". In: *Critical Reviews in Biotechnology* 33.2 (2013), pp. 145–171. DOI: 10.3109/07388551.2012.679250.

[22] M. Böl, R. B. Möhle, M. Haesner, T. R. Neu, H. Horn, and R. Krull. "3D finite element model of biofilm detachment using real biofilm structures from CLSM data". In: *Biotechnology and Bioengineering* 103.1 (2009), pp. 177–186. DOI: 10.1002/bit.22235.

[23] J. Bonet and R. D. Wood. *Nonlinear continuum mechanics for finite element analysis*. Cambridge university press, 1997.

[24] H. Boudarel, J.-D. Mathias, B. Blaysat, and M. Grédiac. "Towards standardized mechanical characterization of microbial biofilms: analysis and critical review". In: *npj Biofilms and Microbiomes* 4 (2018), p. 17. DOI: 10.1038/s41522-018-0062-5.

[25] J. Bryers and W. Characklis. "Early fouling biofilm formation in a turbulent flow system: Overall kinetics". In: *Water Research* 15.4 (1981), pp. 483–491. DOI: 10.1016/0043-1354(81)90059-2.

[26] N. Chopin. "A sequential particle filter method for static models". In: *Biometrika* 89.3 (2002), pp. 539–552. DOI: 10.1093/biomet/89.3.539.

[27] N. Chopin and O. Papaspiliopoulos. *An Introduction to Sequential Monte Carlo*. Springer International Publishing, 2020. DOI: 10.1007/978-3-030-47845-2.

[28] M. Coroneo, L. Yoshihara, and W. A. Wall. "Biofilm growth: A multi-scale and coupled fluid-structure interaction and mass transport approach". In: *Biotechnology and Bioengineering* 111.7 (2014), pp. 1385–1395. DOI: 10.1002/bit.25191.

[29] J. W. Costerton, K. Cheng, G. G. Geesey, T. I. Ladd, J. C. Nickel, M. Dasgupta, and T. J. Marrie. "Bacterial biofilms in nature and disease". In: *Annual Reviews in Microbiology* 41.1 (1987), pp. 435–464.

[30] J. W. Costerton, P. S. Stewart, and E. P. Greenberg. "Bacterial biofilms: a common cause of persistent infections". In: *Science* 284.5418 (1999), pp. 1318–1322.

[31] O. Coussy. *Poromechanics*. Chichester, UK: John Wiley & Sons, Ltd, 2003. DOI: 10.1002/0470092718.

[32] P. Del Moral, A. Doucet, and A. Jasra. "Sequential Monte Carlo samplers". In: *Journal of the Royal Statistical Society: Series B (Statistical Methodology)* 68.3 (2006), pp. 411–436. DOI: 10.1111/j.1467-9868.2006.00553.x.

[33] P. Del Moral, A. Doucet, and A. Jasra. "Sequential Monte Carlo for Bayesian Computation". In: *Bayesian Statistics 8, Oxford University Press*. Ed. by J. M. Bernardo, M. J. Bayarri, J. O. Berger, A. P. Dawid, D. Heckerman, A. F. M. Smith, and M. West. 2007, pp. 1–34.

[34] A. Doucet, N. Freitas, and N. Gordon, eds. *Sequential Monte Carlo Methods in Practice*. Springer New York, 2001. DOI: 10.1007/978-1-4757-3437-9.

[35] M. Edel, H. Horn, and J. Gescher. "Biofilm systems as tools in biotechnological production". In: *Applied Microbiology and Biotechnology* 103.13 (2019), pp. 5095–5103. DOI: 10.1007/s00253-019-09869-x.

[36] H.-C. Flemming, T. R. Neu, and J. Wingender. *The Perfect Slime: Microbial Extracellular Polymeric Substances (EPS)*. Vol. 15. London, UK: IWA Publishing, 2016. DOI: 10.2166/9781780407425.

[37] H.-C. Flemming, P. Baveye, T. R. Neu, P. Stoodley, U. Szewzyk, J. Wingender, and S. Wuertz. "Who put the film in biofilm? The migration of a term from wastewater engineering to medicine and beyond". In: 7.1 (2021). DOI: 10.1038/s41522-020-00183-3.

[38] H.-C. Flemming and J. Wingender. "The biofilm matrix". In: *Nature Reviews Microbiology* 8.9 (2010), pp. 623–633. DOI: 10.1038/nrmicro2415.

[39] H.-C. Flemming, J. Wingender, U. Szewzyk, P. Steinberg, S. A. Rice, and S. Kjelleberg. "Biofilms: an emergent form of bacterial life". In: *Nature Reviews Microbiology* 14.9 (2016), pp. 563–575. DOI: 10.1038/nrmicro.2016.94.

[40] I. Franck and P. Koutsourelakis. "Multimodal, high-dimensional, model-based, Bayesian inverse problems with applications in biomechanics". In: *Journal of Computational Physics* 329 (2017), pp. 91–125. DOI: 10.1016/j.jcp.2016.10.039.

[41] I. M. Franck and P. Koutsourelakis. "Sparse Variational Bayesian approximations for nonlinear inverse problems: Applications in nonlinear elastography". In: *Computer Methods in Applied Mechanics and Engineering* 299 (2016), pp. 215–244. DOI: 10.1016/j.cma.2015.10.015.

[42] S. L. Fuchs, C. Meier, W. A. Wall, and C. J. Cyron. "A novel smoothed particle hydrodynamics and finite element coupling scheme for fluid–structure interaction: The sliding boundary particle approach". In: *Computer Methods in Applied Mechanics and Engineering* 383 (2021), p. 113922. DOI: 10.1016/j.cma.2021.113922.

[43] S. L. Fuchs, C. Meier, W. A. Wall, and C. J. Cyron. "An SPH framework for fluid–solid and contact interaction problems including thermo-mechanical coupling and reversible phase transitions". In: *Advanced Modeling and Simulation in Engineering Sciences* 8.1 (2021). DOI: 10.1186/s40323-021-00200-w.

[44] L. Gierl, K. Stoy, A. Faíña, H. Horn, and M. Wagner. "An open-source robotic platform that enables automated monitoring of replicate biofilm cultivations using optical coherence tomography". In: *npj Biofilms and Microbiomes* 6 (2020), p. 18. DOI: 10.1038/s41522-020-0129-y.

[45] E. S. Gloag, S. Fabbri, D. J. Wozniak, and P. Stoodley. "Biofilm mechanics: Implications in infection and survival". In: *Biofilm* 2 (2020), p. 100017. DOI: 10.1016/j.bioflm.2019.100017.

[46] T. Guélon, J.-D. Mathias, and P. Stoodley. "Advances in Biofilm Mechanics". In: *Springer Series on Biofilms*. Springer Berlin Heidelberg, 2011, pp. 111–139. DOI: 10.1007/978-3-642-19940-0_6.

[47] B. Halan, K. Buehler, and A. Schmid. "Biofilms as living catalysts in continuous chemical syntheses". In: *Trends in Biotechnology* 30.9 (2012), pp. 453–465. DOI: 10.1016/j.tibtech.2012.05.003.

[48] L. Hall-Stoodley, J. W. Costerton, and P. Stoodley. "Bacterial biofilms: from the Natural environment to infectious diseases". In: *Nature Reviews Microbiology* 2.2 (2004), pp. 95–108. DOI: 10.1038/nrmicro821.

[49] L. Hall-Stoodley and P. Stoodley. "Developmental regulation of microbial biofilms". In: *Current Opinion in Biotechnology* 13.3 (2002), pp. 228–233. DOI: 10.1016/S0958-1669(02)00318-X.

[50] G. A. Holzapfel. *Nonlinear Solid Mechanics. A Continuum Approach for Engineering*. English. John Wiley & Sons, 2001.

[51] H. Horn and S. Lackner. "Modeling of Biofilm Systems: A Review". In: (2014), pp. 53–76. DOI: 10.1007/10_2014_275.

[52] T. J. R. Hughes. *The finite element method : linear static and dynamic finite element analysis*. Mineola, NY: Dover Publications, 2000.

[53] A. Imperiale, A. Routier, S. Durrleman, and P. Moireau. "Improving Efficiency of Data Assimilation Procedure for a Biomechanical Heart Model by Representing Surfaces as Currents". In: *Functional Imaging and Modeling of the Heart*. Ed. by S. Ourselin, D. Rueckert, and N. Smith. Berlin, Heidelberg: Springer Berlin Heidelberg, 2013, pp. 342–351. DOI: 10.1007/978-3-642-38899-6_41.

[54] B. D. Jackson, J. M. Connolly, R. Gerlach, I. Klapper, and A. E. Parker. "Bayesian estimation and uncertainty quantification in models of urea hydrolysis by E. coli biofilms". In: *Inverse Problems in Science and Engineering* 29.11 (2021), pp. 1629–1652. DOI: 10.1080/17415977.2021.1887172.

[55] J. Kaipio and E. Somersalo. *Statistical and Computational Inverse Problems*. Springer New York, 2005. DOI: 10.1007/b138659.

[56] S. Kehl. "Bayesian Calibration of Nonlinear Cardiovascular Models for the Predictive Simulation of Arterial Growth". Dissertation. München: Technische Universität München, 2017. URL: http://nbn-resolving.de/urn/resolver.pl?urn:nbn:de:bvb:91-diss-20171219-1364112-1-6.

[57] S. Kehl and M. W. Gee. "Calibration of parameters for cardiovascular models with application to arterial growth". In: *International Journal for Numerical Methods in Biomedical Engineering* 33.5 (2016), e2822. DOI: 10.1002/cnm.2822.

[58] C. T. Kelley. *Iterative Methods for Optimization*. SIAM Society for Industrial and Applied Mathematics, Philadelphia, 1999.

[59] I. Klapper, C. J. Rupp, R. Cargo, B. Purvedorj, and P. Stoodley. "Viscoelastic fluid description of bacterial biofilm material properties". In: *Biotechnology and Bioengineering* 80.3 (2002), pp. 289–296. DOI: 10.1002/bit.10376.

[60] P. Koutsourelakis. "A multi-resolution, non-parametric, Bayesian framework for identification of spatially-varying model parameters". In: *Journal of Computational Physics* 228.17 (2009), pp. 6184–6211. DOI: 10.1016/j.jcp.2009.05.016.

[61] J. Kremheller, S. Brandstaeter, B. A. Schrefler, and W. A. Wall. "Validation and parameter optimization of a hybrid embedded/homogenized solid tumor perfusion model". In: *International Journal for Numerical Methods in Biomedical Engineering* 37.8 (2021). DOI: 10.1002/cnm.3508.

[62] U. Küttler, M. Gee, C. Förster, A. Comerford, and W. A. Wall. "Coupling strategies for biomedical fluid-structure interaction problems". In: *International Journal for Numerical Methods in Biomedical Engineering* 26.3-4 (2010), pp. 305–321. DOI: 10.1002/cnm.1281.

[63] A. La Spina, M. Kronbichler, M. Giacomini, W. A. Wall, and A. Huerta. "A weakly compressible hybridizable discontinuous Galerkin formulation for fluid–structure interaction problems". In: *Computer Methods in Applied Mechanics and Engineering* 372 (2020), p. 113392. DOI: 10.1016/j.cma.2020.113392.

[64] K. Levenberg. "A method for the solution of certain non-linear problems in least squares". In: *Quarterly of applied mathematics* 2.2 (1944), pp. 164–168. DOI: 10.1090/qam/10666.

[65] D. W. Marquardt. "An algorithm for least-squares estimation of nonlinear parameters". In: *Journal of the society for Industrial and Applied Mathematics* 11.2 (1963), pp. 431–441. DOI: 10.1137/0111030.

[66] M. Mayr. "A Monolithic Solver for Fluid-Structure Interaction with Adaptive Time Stepping and a Hybrid Preconditioner". Dissertation. München: Technische Universität München, 2016. URL: http://nbn-resolving.de/urn/resolver.pl?urn:nbn:de:bvb:91-diss-20161215-1315660-1-7.

[67] J. J. Moré. "The Levenberg-Marquardt algorithm: implementation and theory". In: *Numerical analysis*. Berlin, Heidelberg: Springer, 1978, pp. 105–116. DOI: 10.1007/BFb0067700.

[68] M. Morikawa. "Beneficial biofilm formation by industrial bacteria Bacillus subtilis and related species". In: *Journal of Bioscience and Bioengineering* 101.1 (2006), pp. 1–8. DOI: 10.1263/jbb.101.1.

[69] J. Nitzler, J. Biehler, N. Fehn, P.-S. Koutsourelakis, and W. A. Wall. "A generalized probabilistic learning approach for multi-fidelity uncertainty quantification in complex physical simulations". In: *Computer Methods in Applied Mechanics and Engineering* 400.115600 (2022). DOI: 10.1016/j.cma.2022.115600.

[70] J. Nocedal and S. Wright. *Numerical Optimization*. New York: Springer-Verlag GmbH, 2006. DOI: 10.1007/978-0-387-40065-5.

[71] M. R. Pfaller, M. C. Varona, J. Lang, C. Bertoglio, and W. A. Wall. "Using parametric model order reduction for inverse analysis of large nonlinear cardiac simulations". In: *International Journal for Numerical Methods in Biomedical Engineering* 36.4 (2020). DOI: 10.1002/cnm.3320.

[72] C. Picioreanu, F. Blauert, H. Horn, and M. Wagner. "Determination of mechanical properties of biofilms by modelling the deformation measured using optical coherence tomography". In: *Water Research* 145 (2018), pp. 588–598. DOI: 10.1016/j.watres.2018.08.070.

[73] C. Picioreanu, M. C. M. van Loosdrecht, and J. J. Heijnen. "Mathematical modeling of biofilm structure with a hybrid differential-discrete cellular automaton approach". In: *Biotechnology and Bioengineering* 58.1 (1998), pp. 101–116. DOI: 10.1002/(sici)1097-0290(19980405)58:1<101::aid-bit11>3.0.co;2-m.

[74] C. E. Rasmussen and C. K. I. Williams. *Gaussian Processes for Machine Learning*. Cambridge, Massachusetts: the MIT Press, 2006.

[75] S. Rausch. "Computational and Experimental Modeling of Lung Parenchyma". Dissertation. München: Technische Universität München, 2012. URL: http://nbn-resolving.de/urn/resolver.pl?urn:nbn:de:bvb:91-diss-20120723-1107652-1-3.

[76] C. P. Robert. *The Bayesian Choice*. Springer, New York, 2007. DOI: 10.1007/0-387-71599-1.

[77] B. Schott. "Stabilized Cut Finite Element Methods for Complex Interface Coupled Flow Problems". Dissertation. München: Technische Universität München, 2017. URL: http://nbn-resolving.de/urn/resolver.pl?urn:nbn:de:bvb:91-diss-20170331-1304754-1-5.

[78] B. Schott, C. Ager, and W. A. Wall. "Monolithic cut finite element–based approaches for fluid-structure interaction". In: *International Journal for Numerical Methods in Engineering* 119.8 (2019), pp. 757–796. DOI: 10.1002/nme.6072.

[79] P. Stoodley, I. Dodds, J. Boyle, and H. Lappin-Scott. "Influence of hydrodynamics and nutrients on biofilm structure". In: *Journal of Applied Microbiology* 85.S1 (1998), 19S–28S. DOI: 10.1111/j.1365-2672.1998.tb05279.x.

[80] P. Stoodley, K. Sauer, D. G. Davies, and J. W. Costerton. "Biofilms as Complex Differentiated Communities". In: *Annual Review of Microbiology* 56.1 (2002), pp. 187–209. DOI: 10.1146/annurev.micro.56.012302.160705.

[81] P. Stoodley, Z. Lewandowski, J. D. Boyle, and H. M. Lappin-Scott. "Oscillation characteristics of biofilm streamers in turbulent flowing water as related to drag and pressure drop". In: *Biotechnology and Bioengineering* 57.5 (1998), pp. 536–544. DOI: 10.1002/(SICI)1097-0290(19980305)57:5<536::AID-BIT5>3.0.CO;2-H.

[82] P. Stoodley, Z. Lewandowski, J. D. Boyle, and H. M. Lappin-Scott. "Structural deformation of bacterial biofilms caused by short-term fluctuations in fluid shear: An in situ investigation of biofilm rheology". In: *Biotechnology and Bioengineering* 65.1 (1999), pp. 83–92. DOI: 10.1002/(sici)1097-0290(19991005)65:1<83::aid-bit10>3.0.co;2-b.

[83] Y. Sudhakar and W. A. Wall. "A strongly coupled partitioned approach for fluid-structure-fracture interaction". In: *International Journal for Numerical Methods in Fluids* 87.2 (2018), pp. 90–108. DOI: 10.1002/fld.4483.

[84] D. Taherzadeh, C. Picioreanu, and H. Horn. "Mass Transfer Enhancement in Moving Biofilm Structures". In: *Biophysical Journal* 102.7 (2012), pp. 1483–1492. DOI: 10.1016/j.bpj.2012.02.033.

[85] D. Taherzadeh, C. Picioreanu, U. Küttler, A. Simone, W. A. Wall, and H. Horn. "Computational study of the drag and oscillatory movement of biofilm streamers in fast flows". In: *Biotechnology and Bioengineering* 105.3 (2010), pp. 600–610. DOI: 10.1002/bit.22551.

[86] A. Tarantola. *Inverse Problem Theory and Methods for Model Parameter Estimation*. SIAM Society for Industrial and Applied Mathematics, Philadelphia, 2005.

[87] G. Tierra, J. P. Pavissich, R. Nerenberg, Z. Xu, and M. S. Alber. "Multicomponent model of deformation and detachment of a biofilm under fluid flow". In: *Journal of The Royal Society Interface* 12.106 (2015), p. 20150045. DOI: 10.1098/rsif.2015.0045.

[88] S. Tinkl. "Towards a predictive computational growth model for aneurysms". Dissertation. München: Technische Universität München, 2015. URL: http://nbn-resolving.de/urn/resolver.pl?urn:nbn:de:bvb:91-diss-20161209-1230842-1-0.

[89] M. Vaillant, J. Glaunès, G. Christensen, and M. Sonka. "Surface Matching via Currents". In: *Information Processing in Medical Imaging*. Berlin, Heidelberg: Springer, 2005, pp. 381–392.

[90] M. Vert, Y. Doi, K.-H. Hellwich, M. Hess, P. Hodge, P. Kubisa, M. Rinaudo, and F. Schué. "Terminology for biorelated polymers and applications (IUPAC Recommendations 2012)". In: *Pure and Applied Chemistry* 84.2 (2012), pp. 377–410. DOI: 10.1351/PAC-REC-10-12-04.

[91] A.-T. Vuong, L. Yoshihara, and W. Wall. "A general approach for modeling interacting flow through porous media under finite deformations". In: *Computer Methods in Applied Mechanics and Engineering* 283 (2015), pp. 1240–1259. DOI: 10.1016/j.cma.2014.08.018.

[92] A.-T. Vuong. "A Computational Approach to Coupled Poroelastic Media Problems". Dissertation. München: Technische Universität München, 2016. URL: http://nbn-resolving.de/urn/resolver.pl?urn:nbn:de:bvb:91-diss-20161214-1341399-1-5.

[93] M. Wagner and H. Horn. "Optical coherence tomography in biofilm research: A comprehensive review". In: *Biotechnology and Bioengineering* 114.7 (2017), pp. 1386–1402. DOI: 10.1002/bit.26283.

[94] M. Wagner, D. Taherzadeh, C. Haisch, and H. Horn. "Investigation of the mesoscale structure and volumetric features of biofilms using optical coherence tomography". In: *Biotechnology and Bioengineering* 107.5 (2010), pp. 844–853. DOI: 10.1002/bit.22864.

[95] H. Willmann, J. Nitzler, S. Brandstäter, and W. A. Wall. "Bayesian calibration of coupled computational mechanics models under uncertainty based on interface deformation". In: *Advanced Modeling and Simulation in Engineering Sciences* 9.24 (2022). DOI: 10.1186/s40323-022-00237-5.

[96] H. Willmann and W. A. Wall. "Inverse analysis of material parameters in coupled multi-physics biofilm models". In: *Advanced Modeling and Simulation in Engineering Sciences* 9.7 (2022). DOI: 10.1186/s40323-022-00220-0.

[97] P. Wriggers. *Nonlinear Finite Element Methods*. Berlin, Heidelberg: Springer-Verlag GmbH, 2008. DOI: 10.1007/978-3-540-71001-1.

[98] L. Yoshihara, M. Coroneo, A. Comerford, G. Bauer, T. Klöppel, and W. A. Wall. "A combined fluid-structure interaction and multi-field scalar transport model for simulating mass transport in biomechanics". In: *International Journal for Numerical Methods in Engineering* 100.4 (2014), pp. 277–299. DOI: 10.1002/nme.4735.

[99] O. C. Zienkiewicz, R. L. Taylor, and D. D. Fox. *The finite element method for solid and structural mechanics*. Oxford: Butterworth-Heinemann, 2013.

[100] O. C. Zienkiewicz, R. L. Taylor, and J. Z. Zhu. *The finite element method : its basis and fundamentals*. Oxford: Butterworth-Heinemann, 2013.

[101] O. C. Zienkiewicz, R. Taylor, and P. Nithiarasu. *The finite element method for fluid dynamics*. Oxford: Butterworth-Heinemann, 2014.

A Paper A

Inverse analysis of material parameters in coupled multi-physics biofilm models

Harald Willmann, Wolfgang A. Wall

published in

Advanced Modeling and Simulation in Engineering Sciences

Willmann and Wall *Adv. Model. and Simul. in Eng. Sci.(2022)9:7*
https://doi.org/10.1186/s40323-022-00220-0

Advanced Modeling and Simulation in Engineering Sciences

RESEARCH ARTICLE Open Access

Inverse analysis of material parameters in coupled multi-physics biofilm models

Harald Willmann and Wolfgang A. Wall

*Correspondence:
harald.willmann@tum.de
Institute for Computational Mechanics, Technical University of Munich, Boltzmannstr. 15, 85748 Garching b. München, Germany

Abstract

In this article we propose an inverse analysis algorithm to find the best fit of multiple material parameters in different coupled multi-physics biofilm models. We use a nonlinear continuum mechanical approach to model biofilm deformation that occurs in flow cell experiments. The objective function is based on a simple geometrical measurement of the distance of the fluid biofilm interface between model and experiments. A Levenberg-Marquardt algorithm based on finite difference approximation is used as an optimizer. The proposed method uses a moderate to low amount of model evaluations. For a first presentation and evaluation the algorithm is applied and tested on different numerical examples based on generated numerical results and the addition of Gaussian noise. Achieved numerical results show that the proposed method serves well for different physical effects investigated and numerical approaches chosen for the model. Presented examples show the inverse analysis for multiple parameters in biofilm models including fluid-solid interaction effects, poroelasticity, heterogeneous material properties and growth.

Keywords: Inverse analysis, Fluid-solid interaction, Biofilm, Coupled multi-physics

Introduction

Microorganisms tend to live in aggregates rather than dispersed single cells and surround themselves with a network of extracellular polymeric substances (EPS) as a survival strategy. This is called the biofilm matrix [1]. Amongst others it provides them with mechanical resistance against external forces acting on them through a surrounding fluid flow. There is a broad variety of biofilm occurrence. Depending on whether they are intentionally grown or unwillingly observed there are opposing interests when it comes to biofilm control in engineered systems. The prerequisite in all cases however is to have good knowledge about their behavior. In engineering good knowledge is represented by the availability of accurately parameterized models that allow the generation of reliable model predictions.

There has been a variety of efforts to estimate relevant material parameters of biofilms. The reader is referred to [2,3] and [4] as they all give an overview of practiced testing methods for parameter estimation for different physical aspects. Therein a variety of mostly intrusive test strategies and results can be found.

As it is still unknown how much influence the environment of the biofilm has on its mechanical properties [5], an effort towards improved in situ testing methods has been

made. The long term goal of the methods developed in this work is to develop a non-destructive testing protocol for biofilms to estimate material parameters that can later be used to predict biofilm behavior and develop strategies to control their appearance and growth. Optical coherence tomography (OCT) currently seems to be the prime option to scan the geometrical representation of biofilms in flow cell experiments under variable load [6]. This has led to new insights into biofilm mechanics research [7,8]. The advantage is, that automated growth and test protocols [9] can be developed with this technique and therein the biofilm can be kept in the same environment for the whole test cycle.

First parameter estimation approaches are described in [10]. A common scalar approach for determining stiffness and shear resistance is first presented therein. This type of analysis, if it is applicable, is quick to use and serves with estimates of the values in the relevant order of magnitude. While such approaches in the end might not be sufficient for predictions with suffient accuracy, they can favorably be used to assess good initial guesses for more advanced approaches like the presented inverse analysis algorithm. It has been shown in [8] that fully resolved fluid-solid interaction (FSI) simulations can be used to determine one material parameter from modeling flow cell experiments with linear solid mechanics. This has the advantage that in general no specific shape characteristics of the biofilm are required for the parameter estimation.

The present work proposes an inverse analysis algorithm incorporating different numerical models for non destructive experiments with in situ measurement via OCT. The intuitive approach followed in this work is to model the experimental setup as accurately as possible and then try to find the set of parameters that fits experimental data best, in present case via a Levenberg-Marquardt optimization. In order to best analyze and present the properties of the approach, we create a well defined, i.e. clean environment and hence use artificially generated results via forward numerical analysis and the addition of Gaussian noise as a first step and to particularly isolate important effects arising in this kind of analysis. The honest analysis and discussion of strengths and weaknesses of this type of inverse analysis approach is the main motivation to present this as standalone work.

The focus in this work is specifically set on flow cell experiments, like the ones presented in [7] and [11]. In this type of experiments a biofilm is situated in a transparent channel, the flow cell. The biofilm is grown on the channel floor and supplied with a solution of nutrients in the fluid. Once a substantial patch of biofilm has formed, it can be exposed to varying loads in order to observe its deformation. The mechanical load on the biofilm is controlled exclusively via the fluid volume inflow rate into the flow cell and for growth the composition of solutes in the fluid supply. OCT provides precise measurements of biofilm geometries, but it is limited in the image capturing speed, especially when it comes to three dimensional scans [6]. Empty flow cells were designed as channels with rectangular profile with cross sections in the millimeter range in recent experiments. Exemplarily those had the dimensions of $50\,\text{mm} \times 5\,\text{mm} \times 0.45\,\text{mm}$ in [9] or $124\,\text{mm} \times 2\,\text{mm} \times 1\,\text{mm}$ in [7].

Experimental results show different shapes of biofilms for different flow rates through flow cells [11]. Even under automated cultivation and measurement, a certain level of variability can be found [9]. The appearing nearly arbitrary shapes of biofilm surfaces pose the question in which way the model results should be compared to experimental results. The variety in biofilm appearance impedes the accessibility to simple or even scalar comparisons for parameter estimation. When it comes to quantifying flow cell

experiments, the load on the biofilm is sometimes represented by the fluid shear stress next to the wall of the empty flow cell. It is known [8,12] and quite obvious that this shear stress is not fully representative for the load on the biofilm, as the analyzed biofilm patches in published analyses take up a significant portion of the height of the flow channel. The flow rate itself is a more representative quantity. It can also be represented by average inflow velocity or Reynolds number in the fluid flow through the empty channel. Because of the irregular shapes of biofilms, an interplay of forces and local effects in the fluid flow is affecting biofilm deformation in flow cells significantly. This is addressed in this work by full geometrical resolution of flow cell experiments and a consideration of fluid-biofilm interaction at the interface.

In order to be self contained, this article provides a very brief introduction to physical models applicable to different aspects of biofilm mechanics and a brief summary on numerical approximations. In the next step a method for comparing different surfaces is presented and the optimization used to minimize the deviation of model predictions and experimental results is demonstrated. Then the presented algorithm is tested on different cases and the results are discussed. Finally general remarks and the interpretation of the informative value of results achieved with the presented algorithm are discussed. The article is then brought to a conclusion.

Biofilm modeling

Properties and performance of inverse analysis approaches depend strongly on the model used to represent the experiments that are used to drive the inverse analysis. Results of an inverse analysis can never be better than the physical model incorporated. In the given setting of inverse analysis the numerical model of the experiment is referred to as the forward model. The forward model must include all physical aspects that are relevant. In the same sense all the aspects a model covers should be represented in the experimental data used. The choice of a suitable forward model therefore depends on the type of data used and the type of application for parameters to be determined. The best case is that the model used for modeling the experiment in an inverse analysis is the same as the one, the parameters are aimed to be used with to make valid predictions for biofilm behavior in the future.

In the following we briefly sketch models and methods that we have developed in the past and that are used in this work. Modeling approaches to fluid-solid interaction with scalar transport have been proposed in [13] and have been extended to include biofilm growth in [14]. Porous properties of biofilms and porous flow through them are known for a long time [15]. For solving fluid-poroelasticity interaction (FPI) a novel method was developed in [16] and applied to a kind of finger shaped biofilm example therein. The presented workflow works independent of the material model. We exemplarily choose Saint-Venant Kirchhoff or Neo-Hookean material models in our examples.

The inverse analysis algorithm proposed in this paper is obviously not limited to the kind of models presented here. It can also be applied for other models, like one that describes damage in the sense of detachment [17] or viscoelastic behavior [18].

Physical models

The analyzed type of fluid-biofilm interaction includes significant deformations and potentially rotations of subdomains. Therefore the application of nonlinear kinematics is essential. In addition the observations made include a variety of effects of biofilm physics and the according equations for fluid-poroelasticity interaction, scalar transport of potential nutrients and growth are summarized in the following subsections. For the sake of brevity the presentation is limited to the strong field equations. The respective boundary conditions are implicitly assumed to be well defined. Details can be found in the referenced specific literature.

Fluid field

For the fluid field the general Navier-Stokes equations for incompressible flow of a Newtonian fluid are appropriate. In order to allow for deforming domains, that are essential for fluid-solid interaction, they are given in arbitrary Lagrangean-Eulerian (ALE) formulation as

$$\rho^{\mathrm{F}} \frac{\partial \boldsymbol{v}^{\mathrm{F}}}{\partial t} + \rho^{\mathrm{F}} (\boldsymbol{c}^{\mathrm{F}} \cdot \nabla) \boldsymbol{v}^{\mathrm{F}} - 2\mu^{\mathrm{F}} \nabla \cdot \boldsymbol{\epsilon}(\boldsymbol{v}^{\mathrm{F}}) + \nabla p^{\mathrm{F}} = \rho^{\mathrm{F}} \hat{\boldsymbol{b}}^{\mathrm{F}} \qquad \text{in } \Omega^{\mathrm{F}} \times (0, T) \tag{1a}$$

$$\nabla \cdot \boldsymbol{v}^{\mathrm{F}} = 0 \qquad \text{in } \Omega^{\mathrm{F}} \times (0, T). \tag{1b}$$

These equations relate fluid velocity $\boldsymbol{v}^{\mathrm{F}}$, ALE convective velocity $\boldsymbol{c}^{\mathrm{F}}$, fluid pressure p^{F}, fluid density ρ^{F}, fluid dynamic viscosity μ^{F} and a body force $\hat{\boldsymbol{b}}^{\mathrm{F}}$ in the fluid domain $\Omega^{\mathrm{F}} \times (0, T)$. Herein the strain rate tensor $\boldsymbol{\epsilon}(\boldsymbol{v}^{\mathrm{F}})$ is a short expression for

$$\boldsymbol{\epsilon}(\boldsymbol{v}^{\mathrm{F}}) = \frac{1}{2} \left(\nabla \boldsymbol{v}^{\mathrm{F}} + \left(\nabla \boldsymbol{v}^{\mathrm{F}} \right)^{\mathrm{T}} \right). \tag{2}$$

The ALE formulation is one popular approach to model fluid-solid interactions with a moving mesh to ensure the continuity between fluid and solid in case of a moving interface and therein the ALE convective velocity $\boldsymbol{c}^{\mathrm{F}}$ is the fluid velocity relative to the moving mesh.

Solid field

For modeling the nonlinear behavior of solids also allowing for large deformations, the general balance of momentum in reference configuration

$$\rho_0^{\mathrm{S}} \boldsymbol{a}^{\mathrm{S}} = \nabla_0 \cdot (\boldsymbol{F} \cdot \boldsymbol{S}) + \rho_0^{\mathrm{S}} \hat{\boldsymbol{b}}_0^{\mathrm{S}} \quad \text{in } \Omega_0^{\mathrm{S}} \times (0, T) \tag{3}$$

applies. It relates the solid density in reference configuration ρ_0^{S}, solid displacement $\boldsymbol{d}^{\mathrm{S}}$, deformation gradient $\boldsymbol{F}$, second Piola-Kirchhoff stress tensor $\boldsymbol{S}$ and the body force in reference configuration $\hat{\boldsymbol{b}}_0^{\mathrm{S}}$ in the solid domain $\Omega_0^{\mathrm{S}} \times (0, T)$. The solid acceleration $\boldsymbol{a}^{\mathrm{S}}$ is the second material time derivative of the displacement $\boldsymbol{a}^{\mathrm{S}} = \dfrac{\mathrm{d}^2 \boldsymbol{d}^{\mathrm{S}}}{\mathrm{d}t^2}$.

Fluid-solid interface

On the fluid-solid interface $\Gamma^{\mathrm{F,S}} \times (0, T)$ balance of tractions $\boldsymbol{h}_\Gamma^{\mathrm{S}}$ and the equality of velocities, stemming from a no slip condition between fluid and solid, need to hold. The solid velocity $\boldsymbol{v}^{\mathrm{S}}$ is the first material time derivative of the displacement $\boldsymbol{v}^{\mathrm{S}} = \dfrac{\mathrm{d}\boldsymbol{d}^{\mathrm{S}}}{\mathrm{d}t}$.

$$\boldsymbol{h}_\Gamma^{\mathrm{S}} = -\boldsymbol{h}_\Gamma^{\mathrm{F}} \qquad \text{on } \Gamma^{\mathrm{F,S}} \times (0, T) \tag{4a}$$

$$\boldsymbol{v}_\Gamma^{\mathrm{S}} = \boldsymbol{v}_\Gamma^{\mathrm{F}} \qquad \text{on } \Gamma^{\mathrm{F,S}} \times (0, T) \tag{4b}$$

Scalar transport

A scalar transport model in the coupled fluid-solid model is used for nutrient distribution during the flow cell experiment. The solution of this type of systems has been presented in [13] and [14]. The scalar transport equation is stated for the fluid (5a) and the solid (5b) domain.

$$\frac{\partial \Phi^{\mathrm{F}}}{\partial t} + \boldsymbol{c}^{\mathrm{F}} \cdot \boldsymbol{\nabla} \Phi^{\mathrm{F}} - \boldsymbol{\nabla} \cdot \left(D^{\mathrm{F}} \boldsymbol{\nabla} \Phi^{\mathrm{F}} \right) = 0 \quad \text{in } \Omega^{\mathrm{F}} \times (0, T) \tag{5a}$$

$$\frac{\mathrm{d}\Phi^{\mathrm{S}}}{\mathrm{d}t} + \Phi^{\mathrm{S}} \left(\boldsymbol{\nabla} \cdot \boldsymbol{v}^{\mathrm{S}} \right) - \boldsymbol{\nabla} \cdot \left(D^{\mathrm{S}} \boldsymbol{\nabla} \Phi^{\mathrm{S}} \right) + R^{\mathrm{S}} = 0 \quad \text{in } \Omega^{\mathrm{S}} \times (0, T) \tag{5b}$$

For the domains the concentration of the solute is described as Φ^{K} in fluid and solid domains. The respective diffusion coefficients are described as D^{K}, with $\mathrm{K} \in \mathrm{F, S}$ being the index for quantities in one of the phases. R^{S} is the reaction rate. In this work a Monod kinetic relates to nutrient consumption of the biofilm which therefore only appears in the solid domain.

$$R^{\mathrm{S,M}} = K_1^{\mathrm{R}} \frac{\Phi^{\mathrm{S}}}{K_2^{\mathrm{R}} + \Phi^{\mathrm{S}}} \tag{6}$$

This kinetic includes two coefficients, which are the reaction rate K_1^{R} and the half saturation K_2^{R}. The negative normal flux on the interface is computed as

$$h_\Gamma^{\mathrm{K}} = D^{\mathrm{K}} \boldsymbol{\nabla} \Phi^{\mathrm{K}} \cdot \boldsymbol{n}_\Gamma^{\mathrm{K}} \tag{7}$$

for phases K with the respective unit normal $\boldsymbol{n}_\Gamma^{\mathrm{K}}$. On the fluid-solid interface the concentrations and fluxes of the phases K must be equal.

$$\Phi^{\mathrm{S}} = \Phi^{\mathrm{F}} \qquad \text{on } \Gamma^{\mathrm{F,S}} \times (0, T) \tag{8a}$$

$$h^{\mathrm{S}} = h^{\mathrm{F}} \qquad \text{on } \Gamma^{\mathrm{F,S}} \times (0, T) \tag{8b}$$

In this formulation (8b) the fluxes on the interface must be related to the same normal direction on the interface. The scalar transport is only one way coupled to the fluid-solid interaction as the deformation of the solid and the fluid velocity will influence the concentration solution, but the concentration does not really influence solid or fluid field solutions.

Surface growth

We introduce growth or erosion according to [14]. It is assumed that growth or erosion is localized on the biofilm surface and influenced by nutrient flux and surface tractions.

$$\boldsymbol{d}_{\mathrm{g}}^{\mathrm{S}} = \Delta t^{\mathrm{g}} \left(K_1^{\mathrm{g}} h^{\mathrm{S}} - K_2^{\mathrm{g}} \left| \left(\boldsymbol{\sigma}^{\mathrm{S}} \cdot \boldsymbol{n}^{\mathrm{S}} \right) \cdot \boldsymbol{n}^{\mathrm{S}} \right| - K_3^{\mathrm{g}} \left| \sum_{i=1}^{2} \left(\boldsymbol{\sigma}^{\mathrm{S}} \cdot \boldsymbol{n}^{\mathrm{S}} \right) \cdot \boldsymbol{t}_i^{\mathrm{S}} \right| \right) \boldsymbol{n}^{\mathrm{S}} \tag{9}$$

With $\boldsymbol{n}^{\mathrm{S}}$ being the outward pointing normal on the biofilm surface and $\boldsymbol{t}_i^{\mathrm{S}}$ two respective orthogonal unit tangents. This is a relatively simple phenomenological model wherein stress inhibits growth or erodes the biofilm [14] and the nutrient flux into the biofilm domain is the cause for growth. The normal flux contributes to growth with the factor K_1^{g} and the erosion is determined with the factors K_2^{g} due to the normal stress component

and K_3^{g} due to the tangential stress components. Δt^{g} describes the timespan the biofilm is exposed to given growth conditions and $\boldsymbol{d}_{\mathrm{g}}^{\mathrm{S}}$ the resulting displacements of the surface because of growth.

Poroelasticity field

The poroelasticity model, that is used, relies on the assumption of a homogenized mixture between a fluid phase with Darcy flow and a solid structure. Porosity ϕ acts as volume ratio of void that is filled with a fluid phase. This is well described in [19] and a fully coupled numerical model for the field equations was developed in [20]. The coupled system of equations for the poroelastic mixture is derived as

$$\left.\frac{\partial \phi}{\partial t}\right|_{\boldsymbol{X}^{\mathrm{P}}} + \phi \nabla \cdot \boldsymbol{v}^{\mathrm{pS}} + \nabla \cdot \left[\phi \left(\boldsymbol{v}^{\mathrm{pF}} - \boldsymbol{v}^{\mathrm{pS}}\right)\right] = 0 \qquad \text{in } \Omega^{\mathrm{P}} \times (0, T) \quad (10a)$$

$$\rho^{\mathrm{pF}} \left.\frac{\partial \boldsymbol{v}^{\mathrm{pF}}}{\partial t}\right|_{\boldsymbol{X}^{\mathrm{P}}} - \rho^{\mathrm{pF}} \boldsymbol{v}^{\mathrm{pS}} \cdot \nabla \boldsymbol{v}^{\mathrm{pF}} + \nabla p^{\mathrm{pF}} - \rho^{\mathrm{pF}} \hat{\boldsymbol{b}}^{\mathrm{pF}} + \mu^{\mathrm{pF}} \phi \boldsymbol{k}^{-1} \cdot \left(\boldsymbol{v}^{\mathrm{pF}} - \boldsymbol{v}^{\mathrm{pS}}\right) = \boldsymbol{0} \qquad \text{in } \Omega^{\mathrm{P}} \times (0, T) \quad (10b)$$

$$\tilde{\rho}_0{}^{\mathrm{pS}} \boldsymbol{a}^{\mathrm{pS}} - \nabla_0 \cdot \left(\boldsymbol{F} \cdot \boldsymbol{S}^{\mathrm{P}}\right) - \tilde{\rho}_0{}^{\mathrm{pS}} \hat{\boldsymbol{b}}_0^{\mathrm{P}} - J \phi \boldsymbol{F}^{-\mathsf{T}} \cdot \nabla_0 p^{\mathrm{pF}} - \mu^{\mathrm{pF}} J \phi^2 \boldsymbol{k}^{-1} \cdot \left(\boldsymbol{v}^{\mathrm{pF}} - \boldsymbol{v}^{\mathrm{pS}}\right) = \boldsymbol{0} \qquad \text{in } \Omega_0^{\mathrm{P}} \times (0, T). \quad (10c)$$

In (10) the indices $(\bullet)^{\mathrm{pS}}$ for the porous structure phase, also called skeleton and $(\bullet)^{\mathrm{pF}}$ for the fluid phase are used. $J = \det \boldsymbol{F}$ is generally known as the Jacobian determinant being the determinant of the deformation gradient $\boldsymbol{F}$. The time derivates $\left.\frac{\partial (\bullet)}{\partial t}\right|_{\boldsymbol{X}^{\mathrm{P}}}$ in (10) are evaluated in the reference configuration of the porous domain with the reference coordinate $\boldsymbol{X}^{\mathrm{P}}$ held constant. The skeleton velocity $\boldsymbol{v}^{\mathrm{pS}}$ and skeleton acceleration $\boldsymbol{a}^{\mathrm{pS}}$ are the first and second material time derivatives of the skeleton displacement $\boldsymbol{d}^{\mathrm{pS}}$. With the presented formulation the porosity needs an initial value ϕ_0 for each material point and then changes according to the skeleton displacement field of the fully coupled model during deformation. $\tilde{\rho}_0{}^{\mathrm{pS}} = (1 - \phi_0)\rho_0^{\mathrm{pS}}$ represents the macroscopic averaged initial density of the skeleton and $\boldsymbol{k} = (J)^{-1} \boldsymbol{F} \cdot \boldsymbol{K} \cdot (\boldsymbol{F})^{\mathsf{T}}$ is the spatial permeability computed from the permeability $\boldsymbol{K}$ in reference configuration, which is determined with the Kozeny-Carman formula.

$$\boldsymbol{K} = \boldsymbol{I} K \frac{1 - \phi_0^2}{\phi_0^3} \frac{(J\phi)^3}{1 - (J\phi)^2} \quad (11)$$

The porous composite strain energy function is

$$\psi^{\mathrm{P}}(\boldsymbol{E}, J(1-\phi)) = \psi^{\mathrm{P,skel}}(\boldsymbol{E}) + \psi^{\mathrm{P,vol}}(J(1-\phi)) + \psi^{\mathrm{P,pen}}(\boldsymbol{E}, J(1-\phi)). \quad (12)$$

Therein $\psi^{\mathrm{P,skel}}$ is the contribution from the skeleton, $\psi^{\mathrm{P,vol}}$ accounts for the volume change due to changing fluid pressure and the penalty part $\psi^{\mathrm{P,pen}}$ guarantees positive porosity. Those are

$$\psi^{\mathrm{P,vol}} = \kappa \left[J\,(1-\phi)\,/\,(1-\phi_0) - 1 - \ln\left(J\,(1-\phi)\,/\,(1-\phi_0)\right)\right], \quad (13a)$$

$$\psi^{\mathrm{P,pen}} = \eta \left[-\ln(J\phi/\phi_0) + J\phi/\phi_0 - 1/\phi_0\right] \quad (13b)$$

as in [20] with the initial porosity ϕ_0. This formulation allows usage of any hyperelastic material model for the skeleton part of the strain energy function $\psi^{\mathrm{P,skel}}$. We choose the

scaling parameters as penalty parameter $\eta = 1.0$ and bulk modulus $\kappa = 100$ accoring to [20] for the presented example.

Fluid-poroelastic solid interaction

A consistent approach to tackle the interaction of a Newtonian fluid and a poroelastic solid is presented in [16]. The method presented therein is directly applied in this work. On the interface

$$\boldsymbol{\sigma}^{\mathrm{F}} \cdot \boldsymbol{n}^{\mathrm{F}} - \boldsymbol{\sigma}^{\mathrm{P}} \cdot \boldsymbol{n}^{\mathrm{F}} = \mathbf{0} \qquad \text{on } \Gamma^{\mathrm{F,P}} \times (0, T) \tag{14a}$$

$$\boldsymbol{n}^{\mathrm{F}} \cdot \boldsymbol{\sigma}^{\mathrm{F}} \cdot \boldsymbol{n}^{\mathrm{F}} + p^{\mathrm{P^F}} = 0 \qquad \text{on } \Gamma^{\mathrm{F,P}} \times (0, T) \tag{14b}$$

$$\left[\boldsymbol{v}^{\mathrm{F}} - \boldsymbol{v}^{\mathrm{P^S}} - \phi \left(\boldsymbol{v}^{\mathrm{P^F}} - \boldsymbol{v}^{\mathrm{P^S}}\right)\right] \cdot \boldsymbol{n}^{\mathrm{F}} = 0 \qquad \text{on } \Gamma^{\mathrm{F,P}} \times (0, T) \tag{14c}$$

$$\left[\boldsymbol{v}^{\mathrm{F}} - \boldsymbol{v}^{\mathrm{P^S}} - \beta_{\mathrm{BJ}} \phi \left(\boldsymbol{v}^{\mathrm{P^F}} - \boldsymbol{v}^{\mathrm{P^S}}\right) + \kappa \boldsymbol{n}^{\mathrm{F}} \cdot \boldsymbol{\sigma}^{\mathrm{F}}\right] \cdot \boldsymbol{t}_i^{\mathrm{F}} = 0 \qquad \text{on } \Gamma^{\mathrm{F,P}} \times (0, T) \tag{14d}$$

must hold. The conditions describe a balance of tractions between the porelastic mixture and the pure fluid (14a), equality of fluid pressure in the poroelastic and fluid domain (14b), the continuity equation for the normal fluid flow (14c) and the so called Beavers-Joseph conditions [21] for the coupling of the tangential components $i = 1, 2$ in directions $\boldsymbol{t}_i^{\mathrm{F}}$ of the fluid velocities (14d). Therein the interface permeability κ

$$\kappa = \left(\alpha_{\mathrm{BJ}} \mu^{\mathrm{F}} \sqrt{3}\right)^{-1} \sqrt{\mathrm{tr}\,(\boldsymbol{k})} \tag{15}$$

is used. The Beavers-Joseph constants α_{BJ}, β_{BJ} regulate this tangential velocity dependency in (14d). They are both chosen to $\alpha_{\mathrm{BJ}} = \beta_{\mathrm{BJ}} = 1$ in the presented example.

Numerical approximation

For all numerical models a nonlinear finite element method (FEM) based approach is used. For time integration a one-step-theta approach is used. For the pure FSI examples we use a monolithic arbitrary Langrangean-Eulerian (ALE) approach just as in [13] and [14]. For the mesh deformation the ALE fields can be treated as a quasi-elastostatic pseudo solid. Monolithic methods are preferable for FSI problems in many biological applications as they might contain fields with similar density with soft solids, represented here by low Young's modulus [22].

ALE Methods can be problematic when it comes to a change in the topology or large mesh displacements. An alternative approach to overcome difficulties associated with these cases are fixed grid methods. For the fluid-poroelasticity interaction examples presented, a CutFEM based approach [16] is used. For FSI problems an approach based on the so called CutFEM has been developed in recent years [23]. It is capable to solve FSI problems with a fixed fluid grid. For a fixed fluid grid the fluid equation (1a) must be replaced by the Euler formulation with zero grid velocity. Thus, the ALE convective velocity $\boldsymbol{c}^{\mathrm{F}}$ is replaced by the fluid velocity $\boldsymbol{v}^{\mathrm{F}}$ for the fixed grid. The idea is to cut out the parts of the fluid mesh that are covered by the solid and solve the fluid field on the remaining discretization including partially cut elements at the interface. To sustain a proper fluid mesh with uncut elements in the interface vicinity also a hybrid method of ALE and CutFEM was developed in [24]. CutFEM based FSI approaches enable the treatment of cases when it comes to a change in topology like for partial or full detachment or on the other side self contact [25,26].

For the growth algorithm there is the need for multiple time scales as the FSI dynamics acts in the range of seconds and the growth processes take place in the range of days. For this multi-scale approach in time a quasi steady or periodic state for the fluid-solid-scalar interaction is reached with smaller time steps. Based on the FSI and scalar transport solution the nutrient flux and interface tractions are evaluated and surface growth is applied with the much longer growth time step. This procedure is then advanced until the full growth time period is reached. After the growth step an ALE relaxation of the mesh is necessary for the domains on both sides of the interface fluid and biofilm, to distribute the displacements smoothly on the whole domains and thereby reduce mesh distortion [14].

Surface distance measure

We set inverse analysis as a special optimization problem and in the application of optimizers the quantity that is minimized is called objective function [27]. In inverse analysis the objective function somehow describes the difference between experimental observation and forward model output. In this context it turns out that the measure that is used to quantify this difference is a key question in inverse analysis. The result of an inverse analysis always depends on the approach used for this measure. Hence, detailed information about the measurement approach need to be combined with the achieved results for presentation and interpretation. This also makes it obvious that the selection or design of a suitable measure is crucial and must be well considered. One important contribution of this work is to propose a simple geometric measurement for the objective function in this kind of experimental settings for biofilm parameter estimation problems, that is suitable for any optimizer.

As OCT measurements of experiments only contain information if a point in space is likely covered by biofilm or not, there is no pointwise displacement information available. Comparable pointwise displacements from the observed experiment would need to be somehow computed first. But in order to do so, some additional assumptions would need to be introduced, which in turn spoil or bias the outcome. In addition those assumptions - being more or less physical - might even substantially complicate the inverse problem or they might point to “unphysical” scenarios. Because of this we argue that it is not the best idea to compare the forward model evaluations to a field of selected point displacements, which are themselves the result of a postprocessing operation, but rather refer to some primary information, which, in the case of flow cell experiments and OCT, is the surface shape. Evaluating this information is performed as depicted in Fig. 1.

Given an observed result of an OCT measurement the first step is to determine a representation of the fluid-biofilm interface Γ_{obs}, by some sort of image segmentation. Image segmentation is a topic on its own and not the focus of this work. For the purpose of this paper, it is enough to assume that the data is already suitably segmented, which can also mean a segmentation done by hand. On the observed interface Γ_{obs} the analyst is to choose significant points, meaning points where the interface underwent significant displacements during the experiment. These measurement points are depicted as crosses in Fig. 1. The distribution and number of measurement points is up to the choice of the analyst as it depends on many aspects. The number should at least be greater than the number of parameters, that are to be determined in the inverse analysis for the optimizer

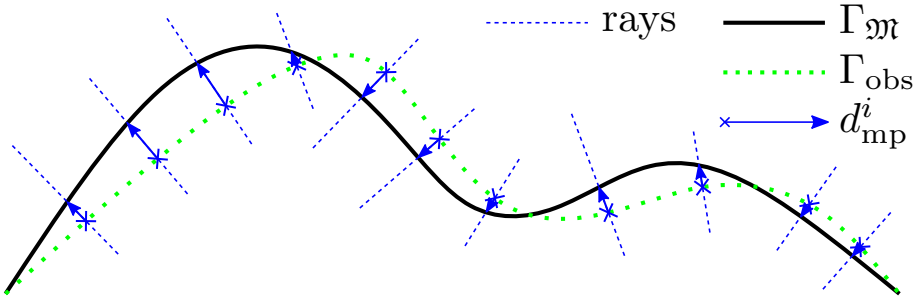

Fig. 1 Prototype sketch for pointwise distances d^i_{mp} from measurement points on the deformed interface Γ_{obs}, observed from experiment, to $\Gamma_{\mathfrak{M}}$ resulting from forward model evaluation, in given measurement directions depicted as rays

to work well. The actual choice of measurement points should in our impression be made towards regions, where the validity of all model assumptions is trusted the most. That means it should favor points away from potentially uncertain boundary conditions and potentially uncertain flow conditions in the channel and towards regions, where the spatial resolution of OCT and the quality of the captured images is trusted the best. Secondly, given the forward model and the parameters analyzed, the measurement points should be chosen in a way that all the different parameters can show significant effect in the resulting distances.

For every point selected, an individual search direction for the intersection with the result for the displaced fluid-biofilm interface from the forward model evaluations $\Gamma_{\mathfrak{M}}$ must be decided. These are depicted as rays in Fig. 1. A general recommendation is the normal direction. Nevertheless again the quality of the image decides if a confident guess for that normal can be made. Given the fact, that OCT scans are generated from above the experiment, the vertical direction is another reasonable choice.

With both the measurement points and the associated directions at hand the thereby defined rays must be intersected with the deformed interface resulting from forward model evaluations $\Gamma_{\mathfrak{M}}$. As the resulting distance for every measurement point d^i_{mp} is based solely on a geometrical measure, it has no inherently conclusive sign. Therefore it is defined positive if the intersection point is on the side of the biofilm with respect to Γ_{obs} and negative if it lies towards the outside. In the case of multiple intersection points the lowest resulting distance is used.

The presented choice of comparative measure for the interfaces including both measurement point location and measurement direction circumvents known drawbacks of the closest point projection described in [28]. With the proposed method the distance measurements are uniquely defined as the search direction is predefined. This can be very useful as, if two or more candidates for the closest point on $\Gamma_{\mathfrak{M}}$ to a measurement point exist, a gradient based optimization with a finite difference approximation as the one presented, can be heavily deteriorated. The capturing of irrelevant shape characteristics must be prevented by a good choice of measurements points by the user.

Overall the presented measurement method is considered rather hands-on, as the observed interface location must only be determined for the measurement points. For our type of problems, this is also a clear advantage compared to the usage of global surface

comparisons as for example the ones presented in [29] and [30]. For global approaches for surface comparison a full representation of the surface must be available and therefore must be constructed from the data. A global measurement approach also poses higher demands on the image segmentation than the presented method. Nevertheless in the case of optimal data acquisition and the assumption that the experiment is modeled optimally, the presented measurement is also fully automatable using factual normals e.g. for every triangle of a triangulation of the observed deformed biofilm surface Γ_{obs}.

Levenberg-Marquardt optimization

For the minimization of the objective function defined by a suitable comparison of observed experiments and a forward model we use a Levenberg-Marqaurdt approach for optimization. Levenberg-Marquardt optimizers go back to the works of Levenberg [31] and Marquardt [32]. A good overview of the actual algorithm is shown in [33]. A Levenberg-Marquardt optimizer is in general a deterministic method. As a gradient based method it represents a local optimizer and is applicable for inverse analysis if the dimension of the inverse problem is low enough and the initial guess is good enough. In the selected numerical examples we will shed some light on the applicability for different numbers of parameters and initial guesses for our target applications. In the past we have already succesfully applied such algorithms for identification of constitutive laws and parameters of hyper- and visco-elastic biomechanical problems (see e.g. for problems with single type of experiments [34,35] and also the combination of different experiments on the same specimen [36]).

In order to have a rather self contained paper we will briefly sketch the algorithm in the following. The Levenberg-Marquardt method is used to minimize a least squares objective function

$$f(x) = \frac{1}{2}\sum_{j=1}^{\mathrm{n_r}} r_j^2(\boldsymbol{x}) = \frac{1}{2}\sum_{j=1}^{\mathrm{n_r}} \left(\mathfrak{M}(\boldsymbol{x})_j - (y_{\text{obs}})_j\right)^2 \tag{16}$$

with forward model results $\mathfrak{M}(\boldsymbol{x})_j$ at potentially different times for $\mathrm{n_x}$ unknown parameters in the parameter vector $\boldsymbol{x}$ and $\mathrm{n_r}$ observed experimental measurements $(y_{\text{obs}})_j$. The algorithm uses the regularization parameter μ and is started from an initial guess $\boldsymbol{x}^0$, μ^0. The core algorithm is to iterate the update rule for the parameter vector

$$\boldsymbol{x}^{k+1} = \boldsymbol{x}^k + \Delta\boldsymbol{x}^{k+1} \tag{17}$$

with the parameter step computed by

$$\Delta\boldsymbol{x}^{k+1} = -\left(\boldsymbol{J}^{\mathsf{T}}\cdot\boldsymbol{J} + \mu\,\mathrm{diag}\left(\boldsymbol{J}^{\mathsf{T}}\cdot\boldsymbol{J}\right)\right)^{-1}\boldsymbol{J}^{\mathsf{T}}\boldsymbol{r} \tag{18}$$

until predefined convergence criteria are met. The iteration index k is omitted in $\boldsymbol{J}^k$, μ^k and $\boldsymbol{r}^k$ from here, as it is clear that terms should be computed exclusively at current step k. We propose that the vector of punctual distances d^i_{mp}, potentially also collected over different time steps, between the forward model result surface and the observed experimental surface measured in the way presented should be directly used as residuals and arranged in the residual vector $\boldsymbol{r}$ of length $\mathrm{n_r}$. In the least squares formulation of the objective function (16) this means $r_j = \mathfrak{M}(\boldsymbol{x})_j - (y_{\text{obs}})_j = d^j_{\text{mp}}$.

$$\boldsymbol{r} = \left[d^1_{\text{mp}} \ \ldots \ d^{\mathrm{n_r}}_{\text{mp}}\right]^{\mathrm{T}} \tag{19}$$

The Levenberg-Marquardt method makes good use of the vector shape of the residual for finding the parameters for the next step. The algorithm uses the partial derivatives of the residual components with respect to the parameters as the Jacobian

$$\boldsymbol{J} = \begin{bmatrix} \frac{\partial r_1}{\partial x_1} & \cdots & \frac{\partial r_1}{\partial x_{\mathrm{n_x}}} \\ \vdots & \ddots & \vdots \\ \frac{\partial r_{\mathrm{n_r}}}{\partial x_1} & \cdots & \frac{\partial r_{\mathrm{n_r}}}{\partial x_{\mathrm{n_x}}} \end{bmatrix}. \tag{20}$$

In absence of actual gradient information, the Jacobian is approximated by finite differences. For that, $\mathrm{n_x}+1$ simulations per iteration are necessary to be computed. One model evaluation is conducted with the current parameter set $\boldsymbol{x}$ $(= \boldsymbol{x}^k)$. $\mathrm{n_x}$ further model evaluations are computed with the i^{th} parameter perturbed to

$$\tilde{x}_i = x_i + \alpha + \beta x_i \quad \Rightarrow \delta x_i = \tilde{x}_i - x_i = \alpha + \beta x_i. \tag{21}$$

Resulting $\mathrm{n_x}$ perturbations of the parameter are written as vectors $\boldsymbol{x}_i$. The approximations of the partial derivatives

$$\frac{\partial r_j}{\partial x_i} \approx \frac{\delta r_j}{\delta x_i} = \frac{r_j(\boldsymbol{x}_i) - r_j(\boldsymbol{x})}{\alpha + \beta x_i} \tag{22}$$

are then arranged into the approximation of the Jacobian

$$\boldsymbol{J} \approx \begin{bmatrix} \frac{\delta r_1}{\delta x_1} & \cdots & \frac{\delta r_1}{\delta x_{\mathrm{n_x}}} \\ \vdots & \ddots & \vdots \\ \frac{\delta r_{\mathrm{n_r}}}{\delta x_1} & \cdots & \frac{\delta r_{\mathrm{n_r}}}{\delta x_{\mathrm{n_x}}} \end{bmatrix} = \begin{bmatrix} \frac{r_1(\boldsymbol{x}_1) - r_1(\boldsymbol{x})}{\alpha + \beta x_1} & \cdots & \frac{r_1(\boldsymbol{x}_{\mathrm{n_x}}) - r_1(\boldsymbol{x})}{\alpha + \beta x_{\mathrm{n_x}}} \\ \vdots & \ddots & \vdots \\ \frac{r_{\mathrm{n_r}}(\boldsymbol{x}_1) - r_{\mathrm{n_r}}(\boldsymbol{x})}{\alpha + \beta x_1} & \cdots & \frac{r_{\mathrm{n_r}}(\boldsymbol{x}_{\mathrm{n_x}}) - r_{\mathrm{n_r}}(\boldsymbol{x})}{\alpha + \beta x_{\mathrm{n_x}}} \end{bmatrix}. \tag{23}$$

To assess how much the current step has improved the result, the gradient based error $\mathrm{err}^k_{\mathrm{grad}}$

$$\left(\left\| \boldsymbol{J}^{\mathsf{T}} \boldsymbol{r} \right\|_2 \right)^k := \mathrm{err}^k_{\mathrm{grad}} \tag{24}$$

can be used. In order to simply evaluate how close the current model solution is to the experiment, the residual error $\mathrm{err}^k_{\mathrm{res}}$ can be computed as

$$\left(\frac{\|\boldsymbol{r}\|_2}{\sqrt{\mathrm{n_r}}} \right)^k := \mathrm{err}^k_{\mathrm{res}}. \tag{25}$$

The regularization parameter is updated according to

$$\mu^{k+1} = \mu^k \frac{\left(\left\| \boldsymbol{J}^{\mathsf{T}} \boldsymbol{r} \right\|_2 \right)^k}{\left(\left\| \boldsymbol{J}^{\mathsf{T}} \boldsymbol{r} \right\|_2 \right)^{k-1}} \tag{26}$$

only if the current step is closer than the previous step.

$$\mathrm{err}^k_{\mathrm{grad}} < \mathrm{err}^{k-1}_{\mathrm{grad}}, \mathrm{err}^k_{\mathrm{res}} < \mathrm{err}^{k-1}_{\mathrm{res}} \tag{27}$$

Treating the regularization parameter in this adjusting way is the only form of adaptivity in the algorithm. In general it helps to find a suitable step size by reducing the regularization especially close to the optimum.

So far the presented Levenberg-Marquardt method shares the property with its family of optimizers to be unbounded. No information about the validity of parameters is introduced so far. Often material parameters come with a valid interval, or constraints, that need to be fulfilled. The pure algorithm presented so far is not constrained, so potentially if the Jacobian indicates further decrease of the residual into a given direction, the algorithm suggests parameters $\boldsymbol{x}^{k+1}$, that cannot be used in the model. On top of the Levenberg-Marquardt algorithm we want to be able to set constraints on every parameter.

$$\boldsymbol{x}_{\text{min}} < \boldsymbol{x}^k < \boldsymbol{x}_{\text{max}} \tag{28}$$

To achieve this property an additional check is introduced. If any suggested parameter in $\boldsymbol{x}^{k+1}$ is out of bounds, the step is declined, the regularization parameter is doubled $\mu^k = 2\mu^k$ and a new step $\boldsymbol{x}^{k+1}$ is proposed. To avoid useless model evaluations the algorithm is terminated if μ^k grows unreasonably high $\mu^k > \mu^0 \cdot 10^6$. In that case no parameter result can be found.

The algorithm is terminated if a certain convergence criterion is met or if a maximum number of iterations is n_{max} reached

$$\epsilon_{\text{grad}} > \text{err}^k_{\text{grad}} \tag{29a}$$

$$\epsilon_{\text{res}} > \text{err}^k_{\text{res}} \tag{29b}$$

$$k > \text{n}_{\text{max}}. \tag{29c}$$

For real experimental data, comparison to ϵ_{grad} is the better suited criterion, because the residual error in the data is unknown. This way iterations are stopped, when the gradient does not indicate significant decent in the residual measure. As err_{grad} has by definition (24) no unique physical unit as it depends on different parameters in $\boldsymbol{x}$, physical units are omitted for this quantity. Overall the algorithm is deterministic and a local optimizer. So, if more than one local optimum exists within or outside of the bounds, there is no guarantee to find a global optimum even for a continuous and bounded problem.

Numerical examples

In the following numerical examples we want to show that given inverse problems in biofilm physics are well solvable with the presented measure for the similarity of surfaces and the Levenberg-Marquardt approach. The general setup is representing a prototype flow cell experiment, wherein a solid representing the biofilm is exposed to a certain volume flow rate from the left and is therefore deformed towards the right. As already stated above, the performance of an inverse analysis depends on a number of things beside the method itself, like the question how well the numerical model represents reality in the experimental setup. Hence in order to get a better impression of the quality of a specific method for a certain type of application, it is advantageous to test such methods on "clean data" first. A common approach to generate such data is to use the numerical model in a forward analysis with some chosen parameters and potentially add some noise to the results, in order to generate artificial experimental or measurement data to be used in the following inverse analyses.

The numerical examples were computed using the referenced methods implemented in the inhouse multi-physics C++ code BACI [37] and a tailored python framework QUEENS [38]. The presented inverse analysis algorithm was newly implemented in QUEENS during

this work. QUEENS is used to run and manage forward model evaluation and conduct the inverse analysis. The intersections of the rays representing the measurement directions and the mesh based forward model results have been found with the python package for vtk [39].

Although the methods are implemented and fully capable of handling three dimensional geometries, for the sake of presentation the examples are limited to two dimensional effects in purely 2D and quasi 2D (i.e. 3D with just one layer of elements in the third dimension and according boundary conditions) examples. For the finite difference scheme (21) $\alpha = 10^{-5}$, $\beta = 10^{-3}$ are chosen for all examples. The fluid is modeled with $\mu^{\mathrm{F}} = 10^{-3}\,\mathrm{Pa\ s}$ and $\rho^{\mathrm{F}} = 10^{3}\,\mathrm{kg/m^3}$ for water. The material models for biofilms share the density of water. The flow cell experiments are modeled to last several seconds. The focus is set on the quasi static case, meaning that the biofilm is free of oscillatory or inertia effects in the observed reference results from forward model evaluation. For that, the inflow rate is applied smoothly with a cosine based function in multiple steps of an increasing volume inflow and then held constant. The inflow is assumed to be the result of laminar channel flow and therefore chosen to have a parabolic profile. This is how the inflow boundary condition can be reduced to a single quantity, the volume inflow rate. On the right hand side boundary a horizontal outflow is enforced, to reflect, that it is no free outflow, but the channel continues downstream from the modeled region.

Homogeneous biofilm

As a first and most simple example the presented inverse analysis algorithm is performed for a fully homogeneous solid model of a biofilm interacting with the fluid flow. The shape of the biofilm domain in the simulated model is arbitrary and inspired by experiments shown in [7,8]. The modeled biofilm patch is held in place on the channel floor with a no-slip condition on its lower, straight boundary. A parabolic fluid flow profile with flow rate $100\,\mathrm{mm^2/s}$ from the left boundary of the purely two-dimensional channel with $2\,\mathrm{mm} \times 1\,\mathrm{mm}$ is ramped up for 10 s. After 15 s a quasi steady deformation state was observed and thus the deformed state is regarded at that time.

For the presented FSI examples a Saint-Venant-Kirchhoff material is used like in other biofilm related works [17,40]. Its behavior is governed by two parameters, namely Young's modulus E and the Poisson's ratio ν. This material is linear in the Green-Langrange strains and second Piola-Kirchhoff stresses and for cases with small deformations can be related to the classical Hooke constitutive law, which is standard in linear continuum mechanics and also used in other biofilm mechanics studies [8]. The biofilm is obviously three-dimensional and it is assumed that its behavior is not changing much in the out of plane direction, which is reflected by using a plain strain assumption for the reduction to two dimensions.

First, the reference result with parameters $\mathrm{E} = 400\,\mathrm{Pa}$ and $\nu = 0.3$ in the biofilm model is computed and the field solutions shown in Fig. 2 are obtained. The biofilm domain fills the volume between the channel floor and its upper surface, that is the fluid-biofilm interface. In Fig. 2b additionally the interface tractions acting on the biofilm, resulting from the fluid-solid coupling, are displayed as arrows. The simplistic assumption commonly used in biofilm mechanics of a constant tangential force on the whole fluid biofilm interface would be distinctively inaccurate in this example, as it can be observed that the interface

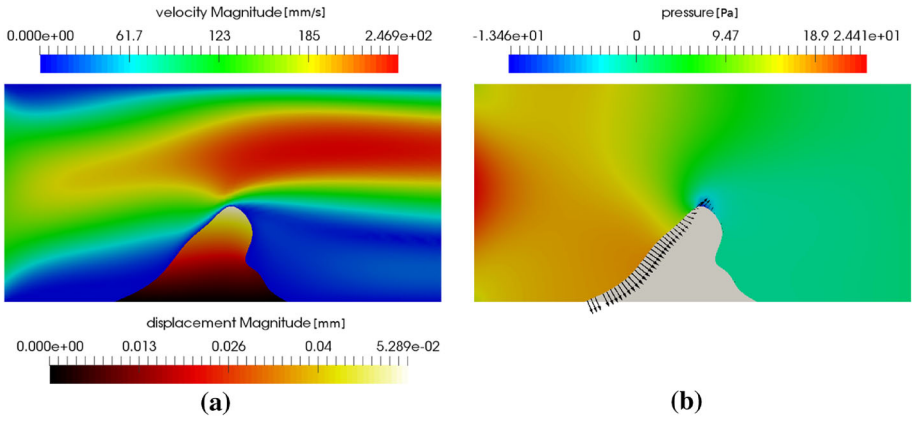

Fig. 2 Field solutions of the reference simulation illustrating the deformed geometry. **a** Fluid velocity magnitude and structure displacement magnitude. **b** Fluid pressure solution and interface tractions on the biofilm as black arrows

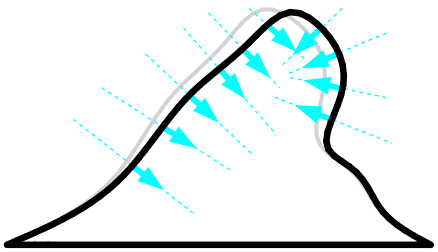

Fig. 3 Measurement points and directions as arrows indicating the positive directions for homogeneous FSI example on the edges of the deformed geometry of the reference result (black) and initial geometry (gray)

Table 1 Initial guesses for different inverse analysis runs in homogeneous example

Color	E^0[Pa]	ν^0[–]
Blue	200	0.4
Orange	200	0.0
Green	400	0.45
Red	400	0.0
Purple	600	0.4
Brown	600	0.0
Pink	400	−0.3
Gray	400	−0.6
Olive	400	−0.9
Cyan	1000	0.0
Black	1000	0.4

tractions are predominantly normal to the interface. The tangential component of the interface tractions varies strongly at the interface. The resulting change in biofilm shape is illustrated in Fig. 3 by the edges of the biofilm domain.

To apply the inverse analysis algorithm, pairs of significant points and the measurement directions on the deformed interface must be chosen. Those are chosen as shown in Fig. 3 on the deformed interface of the reference solution. The points where the rays (dotted lines) cut the interface in Fig. 3 represent the location of the measurement points and the

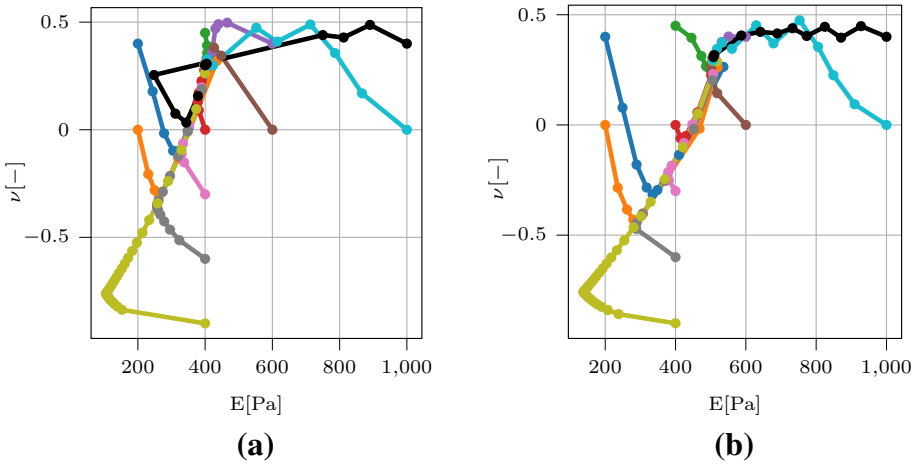

Fig. 4 Path in parameters space towards optimum for data sets **a** without noise and **b** with Gaussian noise with standard deviation $\sigma = 10^{-2}$ mm added to the measurements with one marker per iteration

arrows indicate the direction in which the distance measure is evaluated as positive for respective forward model outputs $\Gamma_{\mathfrak{M}}$. The points are evenly distributed in regions with significant displacement on the upstream and downstream side of the biofilm. Directions are chosen to be normal on the displaced geometry.

With the given prerequisites the inverse analysis of the two material parameters Young's modulus E and the Poisson's ratio ν is conducted with different initial guesses listed in Table 1. The cases with negative Poisson's ratio are included as there is some speculation in the literature wether biofilms are so called auxetic materials. Resulting search paths in the parameter space are shown in Fig. 4 with the associated colors, which are consequently used throughout this example. In Fig. 4 and all following plots each marker represents one Levenberg-Marquardt iteration.

To assess the impact of noise in the data on the inverse analysis result, different scales of normally distributed (Gaussian) noise with standard deviations σ of 10^{-4} mm, 10^{-3} mm and 10^{-2} mm have been added to the measured points representing the experimental data. As compared to the displacement field of the reference result shown in Fig. 2a with a maximum displacement Magnitude $\approx 5.3 \cdot 10^{-2}$ mm, that is about a fifth of that or lower. For all data sets the algorithm has been run for the same initial guesses. The results are summarized in Table 2 for statistics over all algorithm runs with all different initial guesses for the individual noise levels and the noise free case. With increasing noise on the data the remaining residual error err_{res} increases. Means of the parameter results drift away from the ones used for the reference forward model evaluation and the respective standard deviations in the parameter results increase.

The actual resolution of OCT measurements is in the range of μm [6,9]. In this simplest of the presented examples and this primitive uncertainty estimation in Table 2 it appears that the expected accuracy for the inverse analysis with this level of noise reaches at best the first two digits of the parameter results.

From the residual and gradient based errors over the iterations, plotted in Fig. 5, it can be seen that those quantities decrease steeply for the noise free case, when the parameters come close to the local optimum. Only the step size used in (21) for the finite difference

Table 2 Mean values and standard deviations (std) over all runs with different initial guesses per data set with added Gaussian noise with standard deviation σ

σ [mm]	mean err_{res} [mm]	std err_{res} [mm]	mean E [Pa]	std E [Pa]	mean ν [−]	std ν [−]
0.000e+00	7.122e-08	3.120e-08	4.000e+02	1.226e-03	3.000e-01	6.889e-06
1.000e-04	1.478e-04	6.576e-09	3.999e+02	8.615e-03	3.015e-01	6.881e-05
1.000e-03	9.296e-04	2.686e-09	4.080e+02	1.168e-02	3.782e-01	1.153e-04
1.000e-02	8.208e-02	5.892e-09	5.062e+02	5.044e-01	2.998e-01	3.591e-03

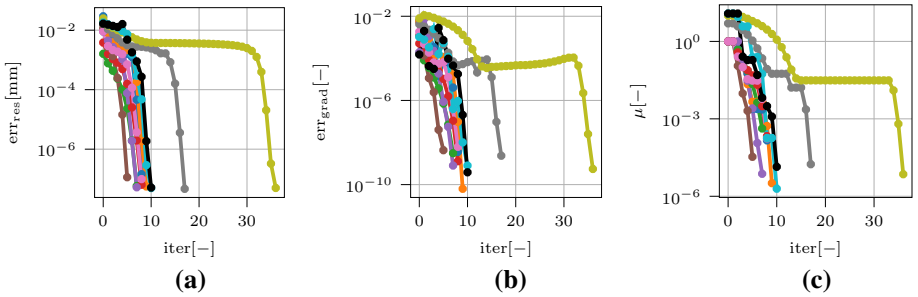

Fig. 5 Development of **a** residual error err_{res}, **b** gradient based error err_{grad} and **c** regularization parameter μ for inverse analysis runs with different initial guesses over iterations

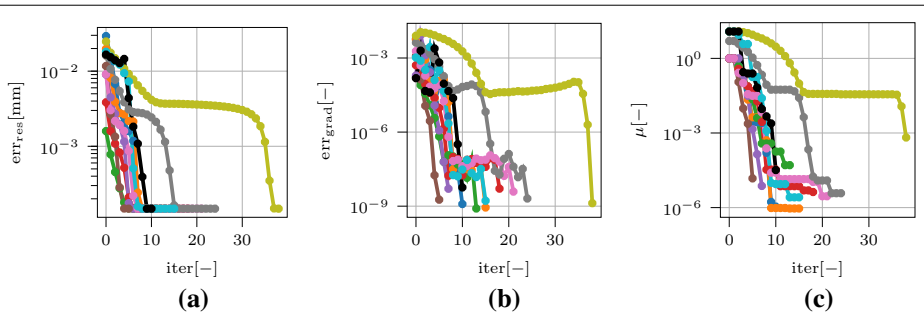

Fig. 6 Development of **a** residual error err_{res}, **b** gradient based error err_{grad} and **c** regularization parameter μ for inverse analysis runs with different initial guesses over iterations, with Gaussian noise with standard deviation $\sigma = 10^{-4}$ mm added to the measurements

approximation limits the accuracy in this setting. For the noisy data it can be seen in Fig. 6 that there is a clear limit to the achievable residual errors err_{res} and some diffuse barrier for the gradient based errors err_{grad} already for the slightest noise. To show this effect the convergence criteria were intentionally not adapted, although it is obvious from Fig. 7 for $\sigma = 10^{-3}$ mm that $\epsilon_{\text{grad}} = 10^{-6}$ would have been a good choice, because there is a distinct level for err_{grad} that cannot be reached even with many more iterations due to a low convergence criterion ϵ_{grad}. For the data set with largest noise level shown in Fig. 8 the gradient based error couldn't be reduced to a tight convergence criterion of $\epsilon_{\text{grad}} = 10^{-8}$, but an adapted value of $\epsilon_{\text{grad}} = 10^{-6}$ did lead to convergence for all initial guesses. It can be further observed that the numbers of iterations until a feasible level of err_{grad} is reached does not vary much for the same initial guesses. From the third column of graphs in Figs. 5, 6, 7, 8, that show the regularization parameter, it can be observed, that as expected the regularization adapts towards low values close to the result, to accelerate the progress of the iterations for all inverse analysis runs.

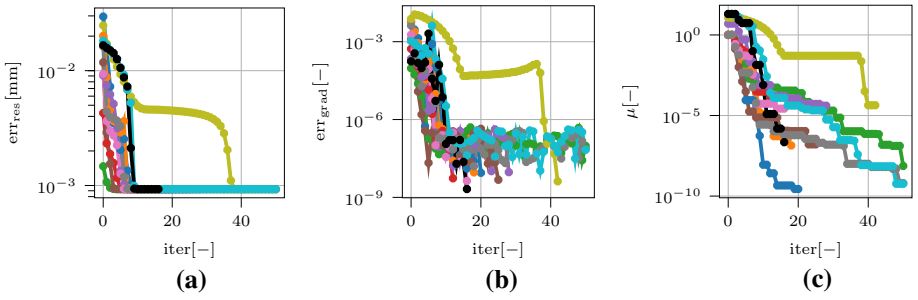

Fig. 7 Development of **a** residual error $\mathrm{err_{res}}$, **b** gradient based error $\mathrm{err_{grad}}$ and **c** regularization parameter μ for inverse analysis runs with different initial guesses over iterations, with Gaussian noise with standard deviation $\sigma = 10^{-3}$ mm added to the measurements

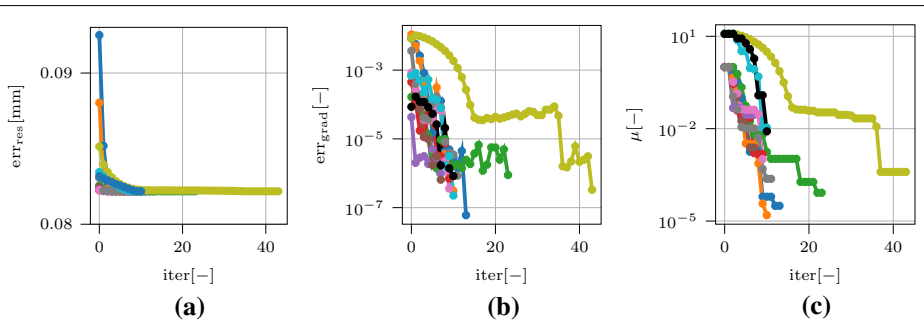

Fig. 8 Development of **a** residual error $\mathrm{err_{res}}$, **b** gradient based error $\mathrm{err_{grad}}$ and **c** regularization parameter μ for inverse analysis runs with different initial guesses over iterations, with Gaussian noise with standard deviation $\sigma = 10^{-2}$ mm added to the measurements

The path in parameter space and therefore the assumed overall shape of the residual error $\mathrm{err_{res}}$ in parameter space does not change significantly for higher noise levels, as seen in Fig. 4, although the level of remaining residual error changes in orders of magnitude. Nevertheless, the reached optimum changes significantly for the Young's modulus $\mathrm{E} = 506.2$ Pa instead of 400 Pa for the maximal noise level, but is rather insensitive for the Poisson's ratio. It is obvious and also shown in Fig. 8 that for the data set with the highest noise the level of remaining error is also the highest, but the algorithm still converges to the same local optimum for all chosen initial guesses. Mind that error plots are all presented in logarithmic scaling. So although there is far less progress in the residual error for noisy data, the algorithm finds the shifted optimum repeatedly for all initial guesses.

Looking at the "olive" green and gray lines in Figs. 4 and 5 it can also be observed, that the residual error is low and rather immobile in a local vicinity of the starting points with low Young's moduli and significantly negative Poisson's ratios. Especially for the initial guess of $\mathrm{E} = 400$ Pa, $\nu = -0.9$, i.e. the "olive" green line, convergence is inhibited by this indifferent shape of the residual error for low Young's modulus E and negative Poisson's ratios $\nu < 0$. But there is a physical explanation for this as with this type of interface location based measurement, quite similar surfaces can be obtained via large bending due to a low value for E or by lateral deformation resulting from negative ν.

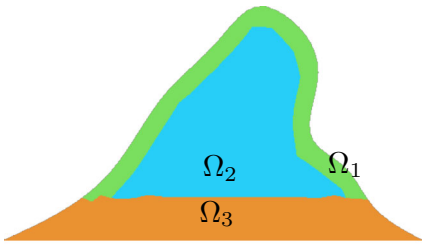

Fig. 9 Subdomains for heterogeneous example

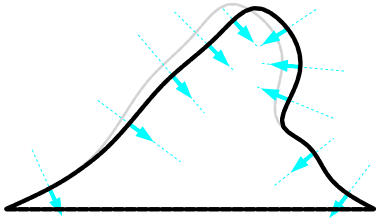

Fig. 10 Measurement points and directions as arrows indicating the positive directions for heterogeneous FSI example on the edges of the deformed geometry of the reference result (black) and initial geometry (gray)

Heterogeneous biofilm

As indicated in the literature [12,41,42] biofilm material properties depend on growth regimes, age and on induced flow rates. This implicates a layer like structure that a biofilm might develop under varying conditions. An arbitrary showcase example model, with subdomains as depicted in Fig. 9, is used to show that the presented method is applicable to determine different material parameters for different subdomains.

The material parameters in this reference solution are: $E_1 = 500\,\text{Pa}$, $\nu_1 = 0.2$, $E_2 = 200\,\text{Pa}$, $\nu_2 = 0.1$, $E_3 = 1000\,\text{Pa}$, $\nu_3 = 0.3$ in a Saint-Venant-Kirchhoff material model. The geometry used for the homogeneous biofilm model is reused here. The channel geometry and fluid volume inflow are controlled in the same way. The deformation of the biofilm under given load due to the interacting fluid forces can be seen in Fig. 10.

Measurement points and directions are also introduced in Fig. 10 on the deformed geometry. It must be taken care to measure all the influences of all subdomains and therefore two measurement points were chosen on the interface of the stiffer footing layer. Measurement was conducted normal to the observed interface.

At first it is verified that with the noise free artificial measurement data, the method allows recovering the correct material parameters. For that a short summary of algorithm runs with different initial guesses listed in Table 3 is plotted in Fig. 11 with the respective colors. Resulting search paths for number of parameters $n_x > 2$ can no longer be interpreted visually with respect to the response surface in err_{res}. Therefore search paths are plotted individually for the parameters. For these plots one color codes one inverse analysis run. In Fig. 11 it can be observed that the inverse analysis is able to find the reference parameters for noise free data for different initial guesses. It was observed that this problem converges faster if Young's modulus E is underestimated in the initial guess. These algorithm runs are the ones with the highest number of parameters presented. It is obvious in the plots, that the search paths for all parameters are interdependent. This is

Table 3 Initial guesses for different inverse analysis runs in heterogeneous example

Color	$E^0_{\{1,2,3\}}$[Pa]	$\nu^0_{\{1,2,3\}}$[−]
Blue	300	0.0
Orange	500	0.3
Green	600	0.0

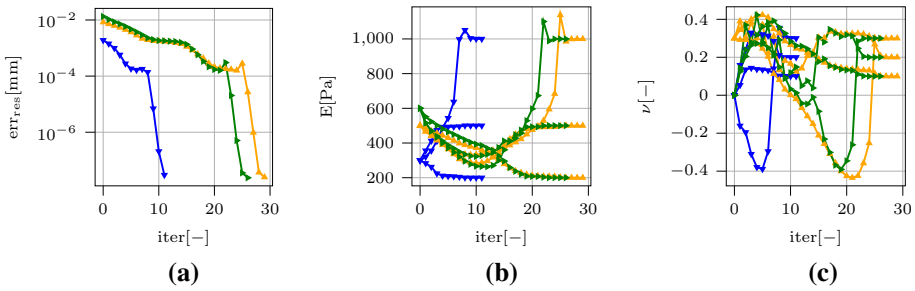

Fig. 11 Result of Inverse analysis for noise free data. Development of **a** residual error $\mathrm{err}_{\mathrm{res}}$, **b** Young's modulus E, **c** Poisson's ratio ν over iterations for different initial guesses

also expected from the algorithm as for every iteration a finite difference approximation of the partial derivatives in all parameters is used to find the next step. The great increase in convergence speed seen in Fig. 11a below $\mathrm{err}_{\mathrm{res}} = 10^{-4}$ mm is a hint, that a very local optimum is found, as also the parameters do not change much for those respective last iterations.

Real OCT resolution is in the range of μm [6,9], so the following examples will be run after Gaussian noise with standard deviation 10^{-3} mm was added to the generated artificial measurement data.

Remark 1 (Estimation of initial guess) For this setting several arbitrary initial guesses did not lead to convergence of the method for the noisy data. That is why the problem is first run with a reduced set of parameters. To do so and set an application oriented scenario, where the heterogeneous character is unknown and the individual parameters are unknown, the domain is assumed to be homogeneous and the material parameters that fit that assumption are searched for. This also helps to loosen the strong one-to-one relationship between generated data and forward model evaluations. The results are displayed in Fig. 12.

In Fig. 13 it shows that the convergence criterion of $\mathrm{err}_{\mathrm{grad}} < 10^{-9}$mm could not be met. So the result must somehow be concluded from the iterations. It is recommended to judge by an adjusted, but still objective convergence criterion. Therefore the data criterion is adjusted to $\mathrm{err}_{\mathrm{grad}} < 10^{-6}$mm. With adjusted convergence criterion the averaged result for two different initial pairs of values, listed in Table 4, is $E = 323$ Pa and $\nu = 0.0656$. For E that is well in between the parameters used for the reference data and for ν that is below all the original values. From this simple numerical experiment we can already conclude that the achievable level of gradient based error $\mathrm{err}_{\mathrm{grad}}$ cannot be predicted and hence the convergence criteria must be tuned to the data used. Nevertheless the result achieved with the algorithm is conclusive even if the algorithm did not converge under too strict criteria.

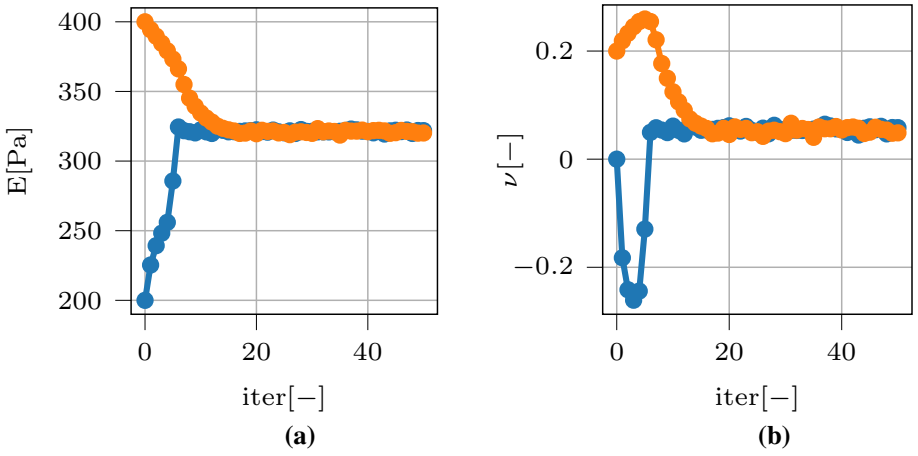

Fig. 12 Result of inverse analysis for added Gaussian noise with $\sigma = 10^{-3}$ mm. **a** Young's modulus E **b** Poisson's ratio ν for two different initial guesses

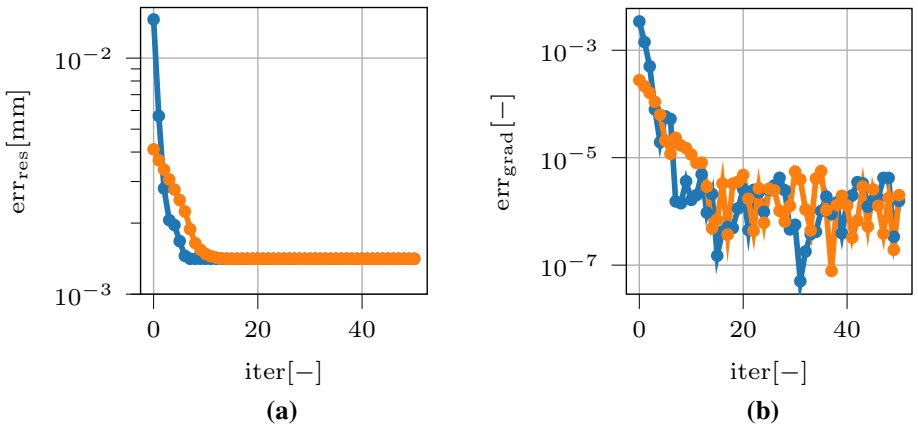

Fig. 13 Errors for inverse analysis with homogeneous assumption on heterogeneous reference results with added Gaussian noise with $\sigma = 10^{-3}$ mm. **a** residual error $\mathrm{err}_{\mathrm{res}}$, **b** gradient based error $\mathrm{err}_{\mathrm{grad}}$ for two different initial guesses

Table 4 Initial guesses for different inverse analysis runs in heterogeneous example with simplification to homogeneous assumption

Color	E^0[Pa]	ν^0[−]
Blue	200	0.0
Orange	400	0.2

In the next step it can be assumed that the domain is in fact heterogeneous and ν is equal for all subdomains. To set this example $\nu_1 = \nu_2 = \nu_3 = 0.1$ is rounded from the result with the assumption of a homogeneous domain in Remark 1 and $E = 300$ Pa is picked as an initial guess for an inverse analysis for E in the three subdomains. This results in a distribution of $E_1 = 497$ Pa, $E_2 = 226$ Pa, $E_3 = 510$ Pa. The correct tendency in stiffness in the subdomains is apparent. Only in the footing layer the result is far off the reference value. Most likely the influence of the stiffness of the footing layer is not conclusive enough towards the shape based surface comparison. The remaining residual

error is $\text{err}_{\text{res}} = 8.98 \cdot 10^{-4}$ mm. That is lower than the solution with the homogeneous approach and even lower than the residual for a model evaluation with the parameters used for the noise free reference result. This means the added noise has altered the data in a way, that it does no longer represent the reference result in the position of the optimum. If as a further step this result is used as an initial guess for a new optimization for all six Parameters, the residual error can be lowered to $\text{err}_{\text{res}} = 7.43 \cdot 10^{-4}$ mm with the result $\text{E}_1 = 273\,\text{Pa}$, $\nu_1 = -0.60$, $\text{E}_2 = 192\,\text{Pa}$, $\nu_2 = -0.10$, $\text{E}_3 = 491\,\text{Pa}$, $\nu_3 = 0.39$. It appears this type of problem and the measurement only via interface deformation favors the assumption, that the material is auxetic, i.e. $\nu < 0.0$. It appears that in this numeric experiment the field of residual error has flipped and the optimum has shifted towards softer, auxetic materials. It is a further conclusion that optimizing for E only is more robust, than the combination of both E and ν at once because a negative ν can compensate a E that is too low in the surface measure. That means that lateral expansion will fill the gap to the optimum for too much bending. Auxetic materials are very rare and mostly occur in specially designed materials with very unique microstructures. As long as that is not proven for the material of interest it is a valid assumption that ν is positive. If nevertheless an optimization result is obtained, that does not seem trustworthy, e.g. negative Poisson's ratio, different initial guesses or even different type of optimizers should be applied and resulting optima compared by their respective residual value err_{res} and plausibility. If the noise in the measurement was too high, or the data not conclusive enough, an increase in data for the specimen might be necessary.

It is known that inverse analysis not only depends on the physical problem at hand as well as on the forward models used, but also on the type and amount of measurement information. For the above type of problems, simply more and other measurement input would be needed in order to allow for identification of all values for Young's modulus and Poisson ratio at the same time. More data could be gathered in form of different snapshots in the same experiment with different load levels or an increase in measurement points. Basically that can be measurements for different settings of the experiments with different load (inflow volume rate) states and developments or different measurement points based on the presented shape comparison. If available, that can also be different measurements from potentially different imaging techniques.

Two-phase poroelastic biofilm

The porous nature of biofilms is well documented. Measurements from OCT scans allow an estimation of biofilm porosity [6]. In the following the attempt to determine porosity via inverse analysis will be presented. The reference result that serves as dummy experiment is set up in a similar manner to previous FSI examples. The biofilm and channel geometry are the same. We switch to the quasi two-dimensional setting with thickness 0.01 mm and use the same inflow rate $100\,\text{mm}^2/\text{s} \cdot 0.01\,\text{mm} = 1\,\text{mm}^3/\text{s}$ over the height of the left boundary. All displacements and velocities in thickness direction are restricted to zero. Further parameters to the fluid-poroelasticity interaction are arbitrarily chosen as permeability $K = 10^{-4}\,\text{mm}^2$ and Poisson's ratio $\nu = 0.3$. The fluid phase in the poroelastic domain also has the properties of water. For the reference result the parameters $\text{E} = 300\,\text{Pa}$ and a homogeneous initial porosity of $\phi_0 = 0.25$ are used in a Neo-Hookean material model. As we are using a fully coupled two-phase poroelastic model, porosity changes

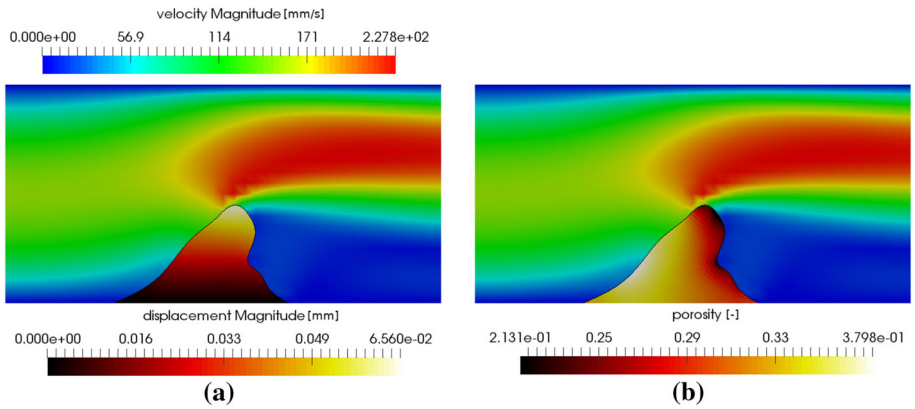

Fig. 14 Solution of the reference simulation for the porous example. Fluid velocity magnitude and **a** skeleton displacement and **b** porosity

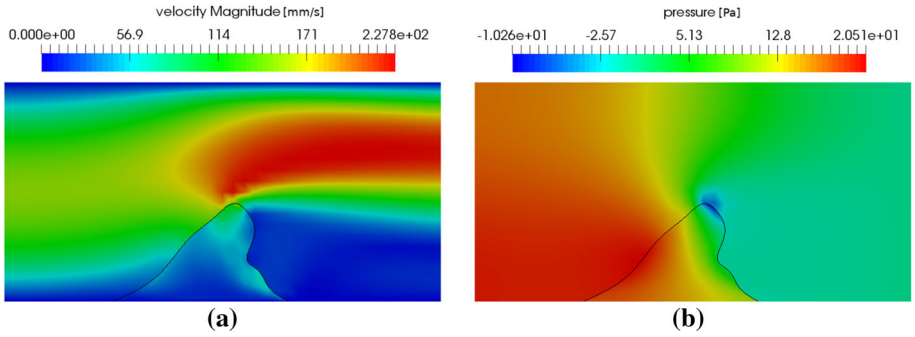

Fig. 15 Results for **a** fluid velocity and **b** fluid pressure of reference simulation illustrated on the deformed geometry both for "external" flow field and fluid inside the porous medium

due to deformations caused by interaction forces from the external flow field but also due to pressure within the porous medium itself. The solution for the velocity magnitude, displacement magnitude and porosity of the biofilm are shown in Fig. 14. It is observed that the biofilm bends with the flow to the right. This is depicted in Fig. 16 where the edges of the initial and deformed geometry ale plotted on top of each other. The porosity opens up in the stretched upstream part and is reduced in compressed downstream regions (see Fig. 14b). The results for velocity and pressure solution of the fluid, inside and outside of the biofilm, are depicted in Fig. 15.

The measurement points used for the inverse analysis are displayed in Fig. 16 on the deformed geometry. They are chosen where the most significant deformation of the interface shape is expected. Knowing, that the varying porosity is coupled to the biofilm deformation one measurement point is chosen on the lower right bump of the geometry. On that basis the inverse analysis is conducted for different initial guesses listed in Table 5. The paths in parameter space are shown in Fig. 17, wherein each marker represents one Levenberg-Marquardt iteration. For two initial guesses, namely the blue and green line, the algorithm converges to the reference parameters and for one initial guess, displayed in orange, the algorithm had to be terminated without result.

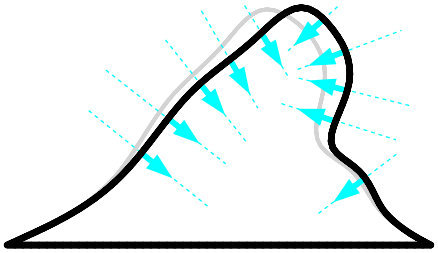

Fig. 16 Measurement points and directions as arrows indicating the positive directions for poroelastic biofilm example on the edges of the deformed geometry of the reference result (black) and initial geometry (gray)

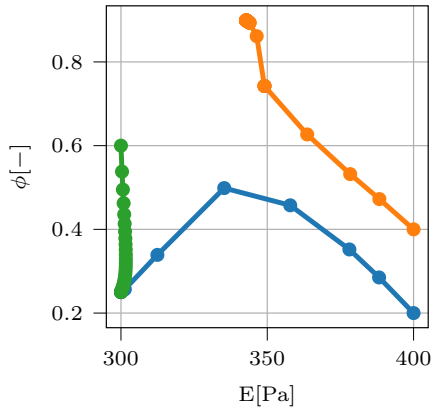

Fig. 17 Path in parameter space towards optimum for porous example

Table 5 Initial guesses for different inverse analysis runs in two-phase poroelastic example

Color	E^0[Pa]	ϕ^0[−]
Blue	400	0.2
Orange	400	0.4
Green	300	0.6

It appears that the measured deformation of the interface is not fully conclusive towards the biofilm material porosity, as higher porosity, due to the interplay between porosity and Young's modulus, also lowers the effective stiffness of the porous medium. And as the porosity is naturally bounded $\phi \in [0, 1]$, the algorithm tends towards the upper bound. Since the gradient indicates further improvement towards this bound, the algorithm gets stuck in the applied upper bound of $\phi_{\max} = 0.9$ and the upper limit for the adaptive regularization parameter terminates iterations. Nevertheless, if the initial guess for Young's modulus is good enough, the optimum can still be found, although it takes many steps. It can be observed in Fig. 18, that also the convergence speed depends strongly on the path in parameter space and therefore obviously also on the quality of the initial guess. Along the first (blue) path the analysis converges in nine steps, whereas the one with a higher starting value for the porosity (green) takes 27.

It would also be desirable to include more parameters into the inverse analysis and, for example, to additionally optimize for permeability K or Poisson's ratio ν in the same algorithm. However this short example is only meant to serve as a proof of concept for the

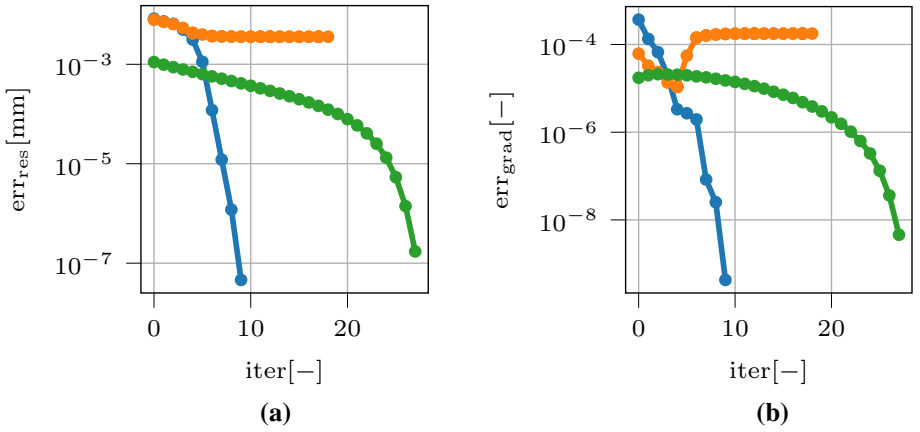

Fig. 18 Result of inverse analysis for porous setting **a** residual error $\mathrm{err_{res}}$ **b** gradient based error $\mathrm{err_{grad}}$ over iterations

suggested approach. In case many parameters and their interplay need to be considered, it definitely makes sense to also include sensitivity analysis and probably also consider probabilistic based (inverse) analysis approaches.

Surface growth of biofilm

This last example demonstrates that the method is also applicable to identify parameters in growth models as the one developed and used in [14]. The inflow rate $0.1\,\mathrm{mm^2/s} \cdot 0.01\,\mathrm{mm} = 10^{-3}\,\mathrm{mm^3/s}$, that is induced from the left side, is much lower in this example as it is applied over a long time period providing growth conditions for the biofilm. Growth processes take place on a different time scale than dynamic FSI and this is accounted for in the temporal multi-scale approach detailed in [14]. The geometry of the problem is chosen as the one presented in [14] to sustain comparability. The flow channel has the dimensions $0.6\,\mathrm{mm} \times 0.3\,\mathrm{mm} \times 0.01\,\mathrm{mm}$ in a quasi twodimensional model with no displacement or velocity in thickness direction. The biofilm is represented by a finger like structure of 0.04 mm width and 0.1 mm height that ends up with a semi circular tip. The inflow velocity profile is parabolic according to the other examples. The FSI time period is 5 s and the fluid inflow rate is increased smoothly. The growth time period is one day. The material parameters for the Saint-Venant-Kirchhoff material are $\mathrm{E} = 100\,\mathrm{Pa}$ and $\nu = 0.3$. They are assumed to be known from a deformation experiment. Like in [14] the concentration of the scalar species at the inflow is chosen in the range of oxygen dissolved in water as $\Phi^{\mathrm{F}}_{\mathrm{in}} = 2.5 \cdot 10^{-11}\,\mathrm{mol/mm^3}$. The reaction rates in (6) are assumed as $K^{\mathrm{R}}_1 = 3.0 \cdot 10^{-11}\,\mathrm{mol/(mm^3\,s)}$, $K^{\mathrm{R}}_2 = 3.0 \cdot 10^{-12}\,\mathrm{mol/mm^3}$. The Diffusion coefficient for both phases is $D^{\mathrm{S}} = D^{\mathrm{F}} = 2.5 \cdot 10^{-3}\,\mathrm{mm^2/s}$. The scalar in the scalar transport problem represents a dummy nutrient for the biofilm and will be referred to as such in the following.

Model equation (9) shows that the used growth model depends on three different parameters, namely K^{g}_1 as the factor for growth on the domain boundaries scaling with the actual nutrient flux, K^{g}_2 as the factor for inhibition of growth due to normal stresses and K^{g}_3 as the factor for inhibition of growth due to shear stresses. They all appear linearly in the chosen surface growth model. For the reference result the parameters $K^{\mathrm{g}}_1 = 6 \cdot 10^4\,\mathrm{mm^3/mol}$, $K^{\mathrm{g}}_2 = 5 \cdot 10^{-2}\,\mathrm{mm^2\,s/g}$ and $K^{\mathrm{g}}_3 = 8 \cdot 10^{-2}\,\mathrm{mm^2\,s/g}$ were used. The reference solution is

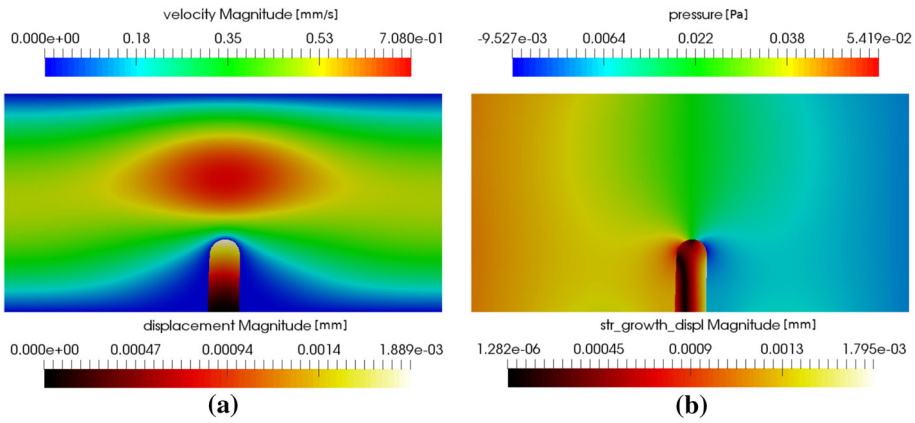

Fig. 19 Solution of the reference simulation illustrating the flow field and the deformed biofilm structure. **a** Fluid velocity and solid displacement field, **b** Fluid pressure and growth magnitude on interface as well as ALE displacements within biofilm domain

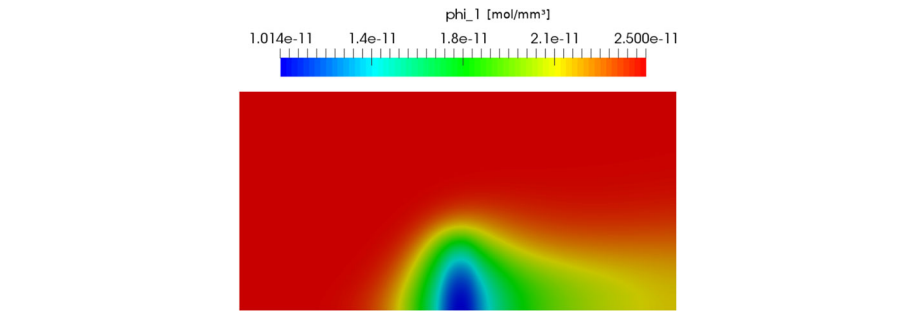

Fig. 20 Solution of the prototype nutrient concentration distribution

shown in Fig. 19 for the fluid velocity and pressure and displacements due to hyperelastic deformation and growth and for the scalar transport species concentration in Fig. 20. The edges of the deformed (bended and grown) biofilm and the initial shape are plotted in Fig. 21.

The changes in biofilm geometry due to displacements and due to growth range in the same order of magnitude. In Fig. 19b surface growth is displayed at the interface along with the solid ALE field on the biofilm domain. This gives a more intuitive overview of the growth deformation, although the ALE field has no physical meaning and the plotted growth stems from a pure surface growth model. The solid ALE displacement field is a reaction to the displacements on the interface induced by growth (9). The displacements are prescribed to the interface nodes of the solid ALE field which is subsequently solved. Figure 19b shows the displacement solution of that solid ALE field which includes the growth displacements on the interface. The nutrient that is transported through the flow is consumed in the biofilm domain according to the reaction rate in (6). This produces a gradient over the interface and therefore nutrient flux, that leads to growth. On the upstream side the growth because of nutrient supply and the inhibition of growth because of higher tractions are more balanced, whereas on the downstream side, where the fluid

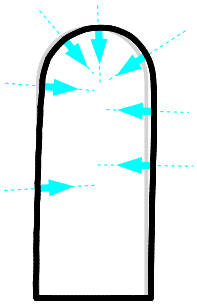

Fig. 21 Measurement points and directions as arrows indicating the positive directions for biofilm example with surface growth on the edges of the actual grown and deformed geometry of the reference result (black) and initial geometry (gray)

Table 6 Initial guesses for different inverse analysis runs in growth example

Color	$(K_1^g)^0 \left[\frac{mm^3}{mol}\right]$	$(K_2^g)^0 \left[\frac{mm^2\,s}{g}\right]$	$(K_3^g)^0 \left[\frac{mm^2\,s}{g}\right]$
Blue	10^4	10^{-2}	10^{-2}
Orange	10^5	10^{-1}	10^{-1}
Green	10^3	10^{-3}	10^{-3}
Red	$3 \cdot 10^4$	$8 \cdot 10^{-2}$	$5 \cdot 10^{-2}$

induces lower tractions, a larger growth is observed at the interface, although the nutrient flux is lower. Over the finger tip the erosive effects of the traction can be observed.

The interface deformations are measured in the points displayed in Fig. 21 on the fully deformed geometry. The distribution of the measurement points is based on the anticipated different regimes - for growth and FSI - on the upstream, downstream and tip side. There must be points in regions with large growth resulting from high nutrient flux or low interface tractions, in regions with high tangential components of the interface tractions and regions with high normal components of the interface tractions.

Initial guesses used for the inverse analysis of the growth parameters are listed in Table 6 and results obtained are plotted in Fig. 22. The errors plotted in Fig. 23 decline over the optimization iterations. It is observed that the search path depends on all growth parameters at once. That means that the residual error err_{res}, as the norm over surface distances, does not measure the three contributions of the parameters to growth and erosion independently in this analysis. This problem setting allows to have initial guesses further away from the optimum, as long as growth is significantly smaller than the dimensions of the biofilm domain. The parameters from the reference data are the result of the inverse analysis for all analyzed initial guesses.

Discussion

Beside the discussion on presented examples also some general remarks and discussions regarding general aspects of the approach that cannot be shown in examples are added for the completeness of the presentation. Further, anticipated general aspects regarding the application of the method are summarized.

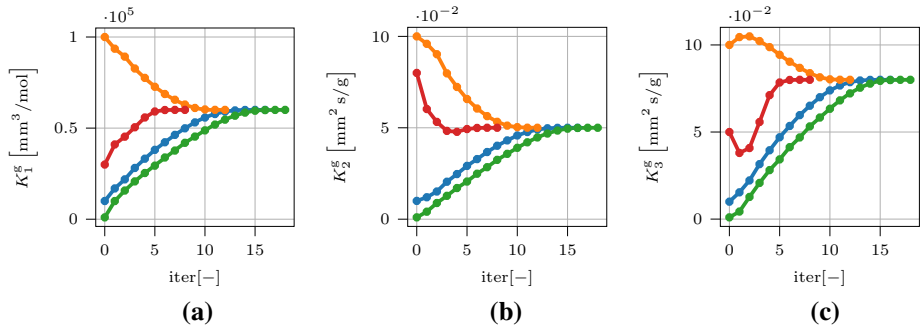

Fig. 22 Result of inverse analysis over iterations for growth parameters **a** K_1^g, **b** K_2^g, **c** K_3^g

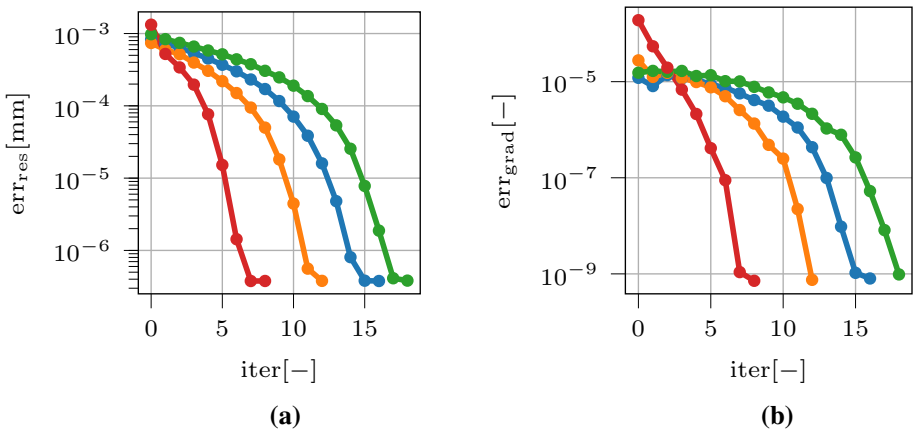

Fig. 23 Errors over iterations for growth inverse analysis **a** residual error $\mathrm{err}_{\mathrm{res}}$, **b** gradient based error $\mathrm{err}_{\mathrm{grad}}$

General discussion of the approach

Significance of parameters

We have looked at coupled models, that displayed different shapes of residual errors over model iterations in parameter space with the given measure of the biofilm surface shape. In several combinations, compensation effects in the parameters occurred (e.g. E and ν or E and ϕ). The presented approach can only be used if the information to all parameters analyzed are actually at least somehow represented in the data and also show effect in the biofilm surface shape in at least partially independent patterns. For presented physical biofilm models the key parameters could nevertheless be determined in example inverse analyses.

Model response

Presented method is not designed to explore the full parameter space, which would be interesting for the global view on the plausibility of combinations of parameters in the whole parameters space for given data. For exploring the residual error on an interval in the parameter space there is a great variety of random or quasi random sampling methods. To efficiently get an global estimation of the objective function in the full parameter space regression methods like for example Gaussian processes [43] on respective sample results can be applied. The advantage of the presented method is, that it is not necessary to

explore the whole parameter space but to find a local minimum with a limited number of iterations and therefore limited amount of forward model evaluations.

Deterministic character

It should be emphasized that the Levenberg-Marquardt optimization is a deterministic approach and there is a risk that the numerical model used for an analysis is not stable along the full search path and especially in the vicinity of the optimum. If the forward model cannot be evaluated and therefore no measurable results retrieved, the finite differences cannot be computed and the algorithm must be terminated, as there is no strategy for following iterations. This drawback further restricts the choice of initial guesses to a set of parameters with which the forward model can be solved.

Computational cost

The computational cost of the algorithm is dominated by the cost for the forward model evaluations. Therefore it scales at least linearly with increasing number of parameters n_x, as more simulations are required per iteration for the finite difference approximation of the Jacobian. Additionally, a higher dimension in parameters of the inverse problem leads to more complex objective functions and therefore potentially longer search paths. In the same sense a higher number of parameters n_x will potentially lead to a smaller region around the optimum for the individual parameters from which the initial guess has to be chosen to be able to find an optimum. In presented examples the algorithm converged or failed in 20-40 iterations.

High number of parameters

From all of the above points it becomes clear that the presented method does not scale arbitrarily well for high number of parameters. The more parameters involved in the model, the more likely it is, that they are differently significant to the forward model solutions and possibly interact in their contribution to the objective function. The objective function gets more complex with higher number of parameters and the probability, that it becomes multimodal, i.e. more than one local optimum exists, increases. The more complex the objective function is, the more likely it is, that the search path leads to parameter regions, where the forward model cannot be evaluated and the inverse analysis yields no result. Higher number of parameters also leads to higher computational cost of a finite difference approximation and search paths grow longer in more complex objective functions increasing the number of finite difference approximations necessary. Overall it is expected that the cost and general applicability of the proposed method scale poorly for high parameter dimensions. For example the inverse analysis of subdomain shapes and therefore an element-wise definition of material parameters can be considered as very high dimensional in general. To overcome the described problems with high dimensions so called Patched Basis Functions can be defined to find the subdomain patches [44].

Comments on application

Importance of initial guess

The presented algorithm includes a local optimizer and it cannot find a reasonable solution for every given combination of parameters as initial guesses. The availability of a good

initial guess is crucial, as it decides if the method converges and also how many mostly costly forward model evaluations are required. Nevertheless the presented algorithm itself can help to find a good initial guess, when it is used with a reduced set of parameters. In the application with real experiments it is unknown if an optimum that was found with one initial guess using the presented approach is a global optimum with regard to given data. Hence inverse analysis results must always be carefully interpreted with respect to plausibility of the results. In doubt it is always possible to validate results by using a second and significantly different initial guess and compare the results.

Model selection

Deterministic inverse analysis is used to find a point estimate only, representing a local best fit of parameters in a chosen forward model. It does not provide a general answer to what type of measurement error is inherent in the data and also not if the forward model used for optimization is itself a good choice or should be improved. This statement is not restricted to the material model but also holds for the physical model and the boundary conditions used for the forward model. In the case of raw flow cell experiment results for example, the best choice for a specific hyperelastic material model is unknown and a Saint-Venant-Kirchhoff material model with its two parameters is just one very simple choice. The selection of a suitable forward model is up to the analyst with presented approach, but also could be included in the inverse analysis by identifying the best parameters for different models and comparing the overall approximative error (like also done in e.g. [34]). If one does that it is very important to relate the approximative quality to the number of parameters in the model (e.g. by the Bayesian or the Akaike information criterion) as we are seeking a predictive model and not just a fit to some data points (see e.g. [34] or [45]).

OCT imaging

The presented measure used for the objective function works independent of the physical model and the spatial dimension of the model. An important feature is that it can easily be used tailored to the data gained from OCT. For example, in the unloaded state a three dimensional scan of a biofilm can be used to build a mesh for computational evaluation and the objective function can be defined with so called B-Scans from the loaded and therefore deformed biofilm, whenever speed of image acquisition is the limit to measurement quality. B-Scans are two dimensional plane scans of the flow cell [7] and naturally faster to acquire than three dimensional images which are just stacks of multiple B-Scans.

Combination of data

Only examples that include information of the initial non deformed geometry of the biofilm incorporated in the forward model mesh and one quasi steady state solution are shown for the sake of concise presentation. But obviously also applications with model evaluations in different time steps or load steps to asses nonlinear material parameters in more complex material models or viscous effects of the biofilm can be easily treated. In such applications, questions of scales and weights of the contribution to the residual $\boldsymbol{r}$ in the objective function must be answered, to not blindly weigh highest displacements the highest. Nevertheless it has been shown in [36] that also results from different experiments

on the same specimen can be scaled and used in a single Levenberg-Marquardt based inverse analysis.

Time scales

In the application of the method, the experiments and results should be grouped in meaningful sets by the time scales involved. One use case can be to first analyze a deformation experiment in the flow cell and determine material parameters in a simple material model and as a second step use other experiments with a more extensive model like additional growth and determine the growth parameters (like in the growth example). In this scenario the growth and hyperelastic material parameters can be regarded as decoupled as time scale for growth is orders of magnitude larger than the time scale for fluid-solid interaction under constant fluid inflow rate.

Convergence criterion

A convergence criterion based on combined maximal number of algorithm iterations and a maximum gradient based error presented itself as a good choice. Even with the presented artificially generated data it was not easily predictable how low the remaining residual error between measured deviation of forward model outcome and experiment observation is. Especially if artificial noise was added to the data, it showed that there was an individual distinct level of residual error, when no better set of parameters could be found. This is also obvious as the noisy data does not define a real physical solution and hence an error has to show up. This combination of convergence criteria can therefore be recommended and needs to be tuned to the specific application depending on the unknown structure of uncertainties in the experiment result data and the cost of forward model evaluations.

Conclusion

An inverse analysis method for biofilms has been presented and successfully tested on several selections of significant parameters in different aspects and models of biofilm physics. The algorithm works with a local best fit for parameter estimates in given forward models related to experimental results in the sense of least squares. A simple hands-on measure for the comparison of shapes of biofilms in deformation experiments has been presented and tested. It has been shown for a variety of different meaningful models for biofilms, like homogeneous, heterogeneous, poroelastic and biofilm models including surface growth, that the presented approach allows the inverse analysis for multiple key parameters at once. As the presented measure for the difference of a biofilm surface between experiment and model evaluations is based purely on their shapes, the approach can without restrictions be used for further different physical models, like ones for detachment, self contact and viscoelasticity.

Acknowledgements

Funding by the German Research Foundation (DFG) with project number WA 1521/22 for this work is gratefully acknowledged. The basis version of the software QUEENS was provided by the courtesy of AdCo Engineering^{GW} GmbH, which is gratefully acknowledged. We thank our project partners at Karlsruhe Institute of Technology (KIT) L. Gierl, M. Wagner and H. Horn for the collaboration that has helped to develop a method that is in the end applicable to real data acquired from experiments.

Author contributions
HW implemented the inverse analysis approach, run the simulations, prepared the figures and primarily drafted the manuscript. WAW worked out the general conception of the project. Both authors contributed to the discussion of results and prepared and approved the final manuscript.

Funding
German Research Foundation (DFG) with project number WA 1521/22.

Availability of data and materials
The research code is hosted on a private GitLab repository at Leibniz Rechenzentrum (LRZ) in Garching. The generated numerical results and digital data are held on machines that are backed up on servers managed by the LRZ in Garching. The datasets used and/or analysed during the current study are available from the corresponding author on reasonable request.

Declarations

Competing interests
The authors declare that they have no competing interests.

Received: 12 October 2021 Accepted: 3 May 2022
Published online: 15 June 2022

References

1. Flemming H-C, Wingender J. The biofilm matrix. Nat Rev Microbiol. 2010;8(9):623–33. https://doi.org/10.1038/nrmicro2415.
2. Böl M, Ehret AE, Albero AB, Hellriegel J, Krull R. Recent advances in mechanical characterisation of biofilm and their significance for material modelling. Crit Rev Biotechnol. 2013;33(2):145–71. https://doi.org/10.3109/07388551.2012.679250.
3. Gloag ES, Fabbri S, Wozniak DJ, Stoodley P. Biofilm mechanics: Implications in infection and survival. Biofilm. 2020;2:100017. https://doi.org/10.1016/j.bioflm.2019.100017.
4. Boudarel H, Mathias J-D, Blaysat B, Grédiac M. Towards standardized mechanical characterization of microbial biofilms: analysis and critical review. npj Biofilms Microbiomes. 2018;4:17. https://doi.org/10.1038/s41522-018-0062-5.
5. Guélon T, Mathias J-D, Stoodley P. Advances in biofilm mechanics. Springer Series on Biofilms, pp. 111–139. Springer, Berlin, Heidelberg; 2011. https://doi.org/10.1007/978-3-642-19940-0_6.
6. Wagner M, Horn H. Optical coherence tomography in biofilm research: a comprehensive review. Biotechnol Bioeng. 2017;114(7):1386–402. https://doi.org/10.1002/bit.26283.
7. Blauert F, Horn H, Wagner M. Time-resolved biofilm deformation measurements using optical coherence tomography. Biotechnol Bioeng. 2015;112(9):1893–905. https://doi.org/10.1002/bit.25590.
8. Picioreanu C, Blauert F, Horn H, Wagner M. Determination of mechanical properties of biofilms by modelling the deformation measured using optical coherence tomography. Water Res. 2018;145:588–98. https://doi.org/10.1016/j.watres.2018.08.070.
9. Gierl L, Stoy K, Faíña A, Horn H, Wagner M. An open-source robotic platform that enables automated monitoring of replicate biofilm cultivations using optical coherence tomography. npj Biofilms Microbiomes. 2020;6:18. https://doi.org/10.1038/s41522-020-0129-y.
10. Stoodley P, Lewandowski Z, Boyle JD, Lappin-Scott HM. Structural deformation of bacterial biofilms caused by short-term fluctuations in fluid shear: an in situ investigation of biofilm rheology. Biotechnol Bioeng. 1999;65(1):83–92.
11. Wagner M, Taherzadeh D, Haisch C, Horn H. Investigation of the mesoscale structure and volumetric features of biofilms using optical coherence tomography. Biotechnol Bioeng. 2010;107(5):844–53. https://doi.org/10.1002/bit.22864.
12. Stoodley P, Cargo R, Rupp CJ, Wilson S, Klapper I. Biofilm material properties as related to shear-induced deformation and detachment phenomena. J Ind Microbiol Biotechnol. 2002;29(6):361–7. https://doi.org/10.1038/sj.jim.7000282.
13. Yoshihara L, Coroneo M, Comerford A, Bauer G, Klöppel T, Wall WA. A combined fluid-structure interaction and multi-field scalar transport model for simulating mass transport in biomechanics. Int J Numer Meth Eng. 2014;100(4):277–99. https://doi.org/10.1002/nme.4735.
14. Coroneo M, Yoshihara L, Wall WA. Biofilm growth: a multi-scale and coupled fluid-structure interaction and mass transport approach. Biotechnol Bioeng. 2014;111(7):1385–95. https://doi.org/10.1002/bit.25191.
15. de Beer D, Stoodley P, Lewandowski Z. Liquid flow in heterogeneous biofilms. Biotechnol Bioeng. 1994;44(5):636–41. https://doi.org/10.1002/bit.260440510.
16. Ager C, Schott B, Winter M, Wall WA. A nitsche-based cut finite element method for the coupling of incompressible fluid flow with poroelasticity. Comput Methods Appl Mech Eng. 2019;351:253–80. https://doi.org/10.1016/j.cma.2019.03.015.
17. Böl M, Möhle RB, Haesner M, Neu TR, Horn H, Krull R. 3d finite element model of biofilm detachment using real biofilm structures from CLSM data. Biotechnol Bioeng. 2009;103(1):177–86. https://doi.org/10.1002/bit.22235.
18. Klapper I, Rupp CJ, Cargo R, Purvedorj B, Stoodley P. Viscoelastic fluid description of bacterial biofilm material properties. Biotechnol Bioeng. 2002;80(3):289–96. https://doi.org/10.1002/bit.10376.
19. Coussy O. Poromechanics. Chichester: Wiley; 2003. https://doi.org/10.1002/0470092718.
20. Vuong A-T, Yoshihara L, Wall WA. A general approach for modeling interacting flow through porous media under finite deformations. Comput Methods Appl Mech Eng. 2015;283:1240–59. https://doi.org/10.1016/j.cma.2014.08.018.
21. Beavers GS, Joseph DD. Boundary conditions at a naturally permeable wall. J Fluid Mech. 1967;30(1):197–207. https://doi.org/10.1017/S0022112067001375.

22. Küttler U, Gee M, Förster C, Comerford A, Wall WA. Coupling strategies for biomedical fluid-structure interaction problems. Int J Numer Methods Biomed Eng. 2010;26(3–4):305–21. https://doi.org/10.1002/cnm.1281.
23. Schott B, Ager C, Wall WA. Monolithic cut finite element–based approaches for fluid-structure interaction. Int J Numer Meth Eng. 2019;119(8):757–96. https://doi.org/10.1002/nme.6072.
24. Schott B, Ager C, Wall WA. A monolithic approach to fluid-structure interaction based on a hybrid eulerian-ALE fluid domain decomposition involving cut elements. Int J Numer Meth Eng. 2019;119(3):208–37. https://doi.org/10.1002/nme.6047.
25. Ager C, Seitz A, Wall WA. A consistent and versatile computational approach for general fluid-structure-contact interaction problems. Int J Numer Methods Eng. 2020. https://doi.org/10.1002/nme.6556.
26. Ager C, Schott B, Vuong A-T, Popp A, Wall WA. A consistent approach for fluid-structure-contact interaction based on a porous flow model for rough surface contact. Int J Numer Meth Eng. 2019;119(13):1345–78. https://doi.org/10.1002/nme.6094.
27. Nocedal J, Wright S. Numerical Optimization. New York: Springer-Verlag GmbH; 2006. https://doi.org/10.1007/978-0-387-40065-5.
28. Imperiale A, Routier A, Durrleman S, Moireau P. Improving efficiency of data assimilation procedure for a biomechanical heart model by representing surfaces as currents. In: Ourselin S, Rueckert D, Smith N, editors. Functional imaging and modeling of the heart. Berlin, Heidelberg: Springer; 2013. p. 342–51. https://doi.org/10.1007/978-3-642-38899-64_1.
29. Vaillant M, Glaunés J, Christensen G, Sonka M. Surface matching via currents. In: Information processing in medical imaging. Berlin, Heidelberg: Springer; 2005. p. 381–392
30. Kehl S, Gee MW. Calibration of parameters for cardiovascular models with application to arterial growth. Int J Numer Methods Biomed Eng. 2016;33(5):2822. https://doi.org/10.1002/cnm.2822.
31. Levenberg K. A method for the solution of certain non-linear problems in least squares. Q Appl Math. 1944;2(2):164–8. https://doi.org/10.1090/qam/10666.
32. Marquardt DW. An algorithm for least-squares estimation of nonlinear parameters. J Soc Ind Appl Math. 1963;11(2):431–41. https://doi.org/10.1137/0111030.
33. Moré JJ. The levenberg-marquardt algorithm: implementation and theory. In: Numerical analysis. Berlin, Heidelberg: Springer; 1978. p. 105–116. https://doi.org/10.1007/BFb0067700
34. Rausch SMK, Martin C, Bornemann PB, Uhlig S, Wall WA. Material model of lung parenchyma based on living precision-cut lung slice testing. J Mech Behav Biomed Mater. 2011;4(4):583–92. https://doi.org/10.1016/j.jmbbm.2011.01.006.
35. Bel-Brunon A, Kehl S, Martin C, Uhlig S, Wall WA. Numerical identification method for the non-linear viscoelastic compressible behavior of soft tissue using uniaxial tensile tests and image registration - application to rat lung parenchyma. J Mech Behav Biomed Mater. 2014;29:360–74. https://doi.org/10.1016/j.jmbbm.2013.09.018.
36. Birzle AM, Martin C, Uhlig S, Wall WA. A coupled approach for identification of nonlinear and compressible material models for soft tissue based on different experimental setups – exemplified and detailed for lung parenchyma. J Mech Behav Biomed Mater. 2019;94:126–43. https://doi.org/10.1016/j.jmbbm.2019.02.019.
37. BACI: A Comprehensive Multi-Physics Simulation Framework. https://baci.pages.gitlab.lrz.de/website/. Accessed 16 Jun 2021
38. Biehler J, Nitzler J, Wall WA, Gravemeier V. QUEENS—a software platform for uncertainty quantification, physics-informed machine learning, Bayesian optimization, inverse problems and simulation analytics: user guide. AdCoEngineering^{GW} 2019.
39. Schroeder W, Martin K, Lorensen B. The visualization toolkit?: an object-oriented approach to 3D graphics. Clifton Park, NY: Kitware; 2006.
40. Taherzadeh D, Picioreanu C, Küttler U, Simone A, Wall WA, Horn H. Computational study of the drag and oscillatory movement of biofilm streamers in fast flows. Biotechnol Bioeng. 2010;105(3):600–10. https://doi.org/10.1002/bit.22551.
41. Klapper I, Dockery J. Mathematical description of microbial biofilms. SIAM Rev. 2010;52(2):221–65. https://doi.org/10.1137/080739720.
42. Wang Q, Zhang T. Review of mathematical models for biofilms. Solid State Commun. 2010;150(21–22):1009–22. https://doi.org/10.1016/j.ssc.2010.01.021.
43. Rasmussen CE, Williams CKI. Gaussian processes for machine learning. Cambridge, MA: MIT Press Ltd; 2006.
44. Schoeder S, Olefir I, Kronbichler M, Ntziachristos V, Wall WA. Optoacoustic image reconstruction: the full inverse problem with variable bases. Proc R Soc A Math Phys Eng Sci. 2018;474(2219):20180369. https://doi.org/10.1098/rspa.2018.0369.
45. Nagler A, Bertoglio C, Stoeck CT, Kozerke S, Wall WA. Maximum likelihood estimation of cardiac fiber bundle orientation from arbitrarily spaced diffusion weighted images. Med Image Anal. 2017;39:56–77. https://doi.org/10.1016/j.media.2017.03.005.

Publisher's Note

B Paper B

Bayesian calibration of coupled computational mechanics models under uncertainty based on interface deformation

Harald Willmann, Jonas Nitzler, Sebastian Brandstäter,
Wolfgang A. Wall

published in

Advanced Modeling and Simulation in Engineering Sciences

Willmann *et al. Advanced Modeling and Simulation in Engineering Sciences(2022)9:24*
https://doi.org/10.1186/s40323-022-00237-5

Advanced Modeling and Simulation in Engineering Sciences

RESEARCH ARTICLE Open Access

Bayesian calibration of coupled computational mechanics models under uncertainty based on interface deformation

Harald Willmann[1*], Jonas Nitzler[1,2], Sebastian Brandstäter[1,3] and Wolfgang A. Wall[1]

*Correspondence: harald.willmann@tum.de
[1]Institute for Computational Mechanics, Technical University of Munich, Boltzmannstr. 15,, 85748 Garching b. München, Germany
[2]Professorship for Data-driven Materials Modeling, Technical University of Munich, Boltzmannstr. 15, 85748 Garching b. München, Germany
[3]Institute for Continuum and Material Mechanics, University of Technology Hamburg, Eißendorfer Str. 42, 21073 Hamburg, Germany

Abstract

Calibration or parameter identification is used with computational mechanics models related to observed data of the modeled process to find model parameters such that good similarity between model prediction and observation is achieved. We present a Bayesian calibration approach for surface coupled problems in computational mechanics based on measured deformation of an interface when no displacement data of material points is available. The interpretation of such a calibration problem as a statistical inference problem, in contrast to deterministic model calibration, is computationally more robust and allows the analyst to find a posterior distribution over possible solutions rather than a single point estimate. The proposed framework also enables the consideration of unavoidable uncertainties that are present in every experiment and are expected to play an important role in the model calibration process. To mitigate the computational costs of expensive forward model evaluations, we propose to learn the log-likelihood function from a controllable amount of parallel simulation runs using Gaussian process regression. We introduce and specifically study the effect of three different discrepancy measures for deformed interfaces between reference data and simulation. We show that a statistically based discrepancy measure results in the most expressive posterior distribution. We further apply the approach to numerical examples in higher model parameter dimensions and interpret the resulting posterior under uncertainty. In the examples, we investigate coupled multi-physics models of fluid–structure interaction effects in biofilms and find that the model parameters affect the results in a coupled manner.

Keywords: Bayesian calibration, Inverse analysis, Coupled problems, Fluid–structure interaction, Interface shape, Biofilm

Introduction

In this article we present a robust approach for Bayesian calibration [1,2] of coupled computational mechanical models based on the deformation of an interface or boundary. In the most general case, the search for a set of parameters leading to a desired model result can be understood as an *inverse problem* [3]. Basic elements are a computational

mechanics model $\mathfrak{M}$, also called the *forward model*, with model parameters $\boldsymbol{x}$ that are considered as inputs to the forward problem. The model parameters can be prescribed in the model and they are expected to significantly influence the associated model response. The inverse problem is characterized by the task to find one or multiple model parameters that result in a desired model behavior. In this paper, we are interested in a special case of desired model behavior which is given in form of observed experimental data. Here, we want to find suitable model parameters such that the model response is close to the experimental data in a given metric. This category of inverse problems is also known as a *calibration* or *parameter identification* problem.

We want to distinguish two different viewpoints on the calibration problem. We refer to the first one as the *deterministic* calibration approach, which poses the calibration task as an optimization problem by minimizing a discrepancy function over the forward model parameters, between the forward system response and the experimental data. Following the deterministic optimization approach, the problems are often ill-posed. The second viewpoint is the probabilistic Bayesian calibration approach, that we follow in this article. In contrast to the aforementioned optimization, the Bayesian approach adopts a statistical viewpoint. It seeks the *posterior* probability density for the input parameters. This density quantifies the probability of resulting forward model system outputs to match the experimental data best, in a specified norm. Instead of a single point estimate as in the optimization problem, the posterior distribution returns the unique probability density for all inputs in the input space. This allows to answer a plethora of additional research questions. A Bayesian, statistical viewpoint does not only provide a powerful mathematical framework for the formulation of the inverse problem but also helps with the design and interpretation of very flexible discrepancy measures between simulation output and experimental observation. Those can be formulated in form of reproducing kernel Hilbert space (RKHS) norms as demonstrated in this article. The Bayesian setting allows for the incorporation of available prior knowledge which is especially advantageous in the small data regime, induced by expensive simulation runs or limited experimental data. The Bayesian formulation provides a consistent mathematical framework that can naturally deal with different sources of uncertainty such as they might arise from partially unknown experimental conditions, as also studied in this work.

The scenario where a mechanical structure changes its shape under mechanical load, but no displacements of individual material points can be determined is the focus of the presented approach. Such scenarios appear when only the shape and changes in shape of a structure can be observed, e.g., in the form of image data. In that case only information about the shape of a boundary or interface is reliably accessible, without further details on correspondence of material points in simulation and experimental data. For such scenarios that have been studied before [4] for, e.g., cardiac mechanics [5] or arterial growth [6], we want to investigate and discuss the effect of different definitions for discrepancy measures between simulated and observed interface deformations of objects. Especially regarding bio-materials the main interest is to determine material properties as they act in-situ, i.e., in the natural environment. Traditional material testing often defines standardized testing methods where the specimen must be isolated and installed in a specific testing device. For very sensitive materials the isolation of a specimen can already change the properties of the material of interest significantly. Often such scenarios occur with coupled physics as, e.g., fluid–structure interaction (FSI) problems, as an isolation of the specimen would interfere

with the coupling. That is why a comparison between deformations in the computational model and an observed deformation in an in-situ experiment is required to test such sensitive materials.

While the presented approach will be useful for any kind of (coupled) mechanical model, our focus will be on the particularly challenging problem class of *fluid–structure interaction* (FSI). A specific motivation for us is our research on biofilms and respective experiments conducted with such biofilms. Biofilms grow with aggregates of microorganisms that form a structure of extracellular polymeric substances to withstand environmental influences. This is also known as the biofilm matrix [7]. Amongst others due to its soft consistency, the determination of mechanical properties of biofilms is an open field of research and different intrusive and non-intrusive attempts have been made to quantify the material behavior [8–10]. The better understanding and analysis of biofilm material properties is essential to better explain biofilm behavior and to enable the development of reliable and predictive computational modeling. Well parameterized mechanical models enable engineers to make valid predictions of biofilm behavior, e.g., deformation, growth or erosion and use those to develop biofilm-prone systems. This means to either avoid invasive biofilms or improve productive biofilm systems. Biofilms usually develop on surfaces exposed to fluid flows and therefore a mechanical model must include the FSI between biofilm surface and the fluid. As the capability of computational mechanical models of fluid–solid interaction increases, the inclusion of such models in deterministic inverse analysis of biofilms has emerged in recent years [11,12]. One of the best approaches to acquire image data of biofilms is via optical coherence tomography (OCT) in flow cell experiments, as used in, e.g., [11,13,14]. This type of experiments is favorable in means of mechanical testing as it is non-destructive and the biofilm can be kept in the same environment for the whole cultivation and test process. Recent advances in automated biofilm cultivation and design of flow cell experiments [15] have already shown that a variety in biofilm shapes is inevitable even for reproducible environmental conditions and therefore a flexible method of comparing biofilm shapes is required for conclusive inverse analysis. Recently, Bayesian estimation and uncertainty quantification (UQ) have been used for models of urea hydrolysis by biofilms [16].

The rest of the article is structured as follows. First, the theoretical concepts of the Bayesian approach for an efficient model calibration under uncertainty will be presented. The technical details and realization of our approach are then outlined. Eventually, we demonstrate and discuss the calibration procedure of numerical models in examples of biofilm motivated fluid-solid interaction models for generated data in two to six input dimensions. Results and key aspects of the workflow are then concluded.

Continuous formulation of the Bayesian calibration problem under uncertainty

Our Bayesian calibration approach is based on the continuous formulation of Bayes' rule. Therefore first the general formulation of the Bayesian calibration is introduced and subsequently extended to include the effects of uncertainties. As a necessary step, the formulation of a likelihood model is described and specific choices for the measure of discrepancy between interface shapes are introduced.

Standard formulation for Bayesian calibration

We assume that we have a computational forward model $\mathfrak{M}(\boldsymbol{x}, C)$ for a real-world process, i.e., in our case a single- or multi-field continuum mechanical problem, whose response depends on the choice of inputs $\boldsymbol{x}$ and the choice of (e.g., spatio-temporal) coordinates C. In general, observations are compared in more than one location and point in time and therefore the coordinates are written as a matrix C with vector entries for each comparison. Consequently, the observations for all coordinates are a matrix $Y_{\text{obs},C}$ as well with vector entries for each coordinate vector. In our case for the comparison of interface deformations, the observations are locations of the interface that define its shape for one or more points in time. The input parameters $\boldsymbol{x}$ are the quantities of interest in the calibration process. The vector $\boldsymbol{x}$ denotes a collection of model parameters that are subject to calibration and might represent, e.g., material parameters, boundary or initial conditions. The observed data $Y_{\text{obs},C}$ might additionally be subject to unknown measurement noise.

In the Bayesian framework, the calibration problem is interpreted as an update of a prior belief about the parameters, encoded by a *prior density* $p(\boldsymbol{x})$, by a so-called *likelihood model* $p\left(Y_{\text{obs},C}|\mathfrak{M}(\boldsymbol{x}, C)\right)$. The likelihood model expresses the probability density to observe the experimental data $Y_{\text{obs},C}$ at coordinate C given a specific choice of model with input $\boldsymbol{x}$ evaluated at the same coordinates C. As the expression $p\left(Y_{\text{obs},C}|\mathfrak{M}(\boldsymbol{x}, C)\right)$ is only a valid density in $Y_{\text{obs},C}$ but not in the model inputs $\boldsymbol{x}$ one mostly refers to it as the so-called *likelihood function*. The likelihood function relates the output $\mathfrak{M}(\boldsymbol{x}, C)$ of the computational model $\mathfrak{M}$ with the observation $Y_{\text{obs},C}$, given a specific choice of parameters $\boldsymbol{x}$. The value of $p\left(Y_{\text{obs},C}|\mathfrak{M}(\boldsymbol{x}, C)\right)$ at a specific $\boldsymbol{x}$ can be interpreted as the probability density of the observations $Y_{\text{obs},C}$ for the given model choice $\mathfrak{M}(\boldsymbol{x}, C)$ or as a score value for the parameter choice $\boldsymbol{x}$. The product of the likelihood function and the prior can be evaluated point-wise in the parameter space $\Omega_{\boldsymbol{x}}$, yielding a function that we call the *unnormalised posterior* $p\left(Y_{\text{obs},C}|\mathfrak{M}(\boldsymbol{x}, C)\right)p(\boldsymbol{x})$. Normalizing this expression by $\int p\left(Y_{\text{obs},C}|\mathfrak{M}(\boldsymbol{x}, C)\right)p(\boldsymbol{x})\,\mathrm{d}\boldsymbol{x}$ such that we get a valid density that integrates to one, yields the *posterior* distribution $p\left(\boldsymbol{x}|Y_{\text{obs},C}\right)$. The posterior distribution can be interpreted as an updated prior distribution, after the knowledge of the experimental data $Y_{\text{obs},C}$ has been incorporated and related to the forward model $\mathfrak{M}(\boldsymbol{x}, C)$.

An advantage of the Bayesian viewpoint on calibration is the possibility to encode prior knowledge of the unknown parameters or inputs $\boldsymbol{x}$ in the so-called *prior* distribution $p(\boldsymbol{x})$. Prior knowledge is information about the parameters that is available before seeing the data. Often, at least a vague understanding about which values are possible or realistic is available (e.g., the Young's modulus must be positive $E > 0\,\text{Pa}$). This knowledge and additional valuable expert knowledge can be incorporated as prior and therefore the solution of the calibration complies with it.

We can then pose the calibration problem as a Bayesian inference task by applying Bayes' rule [17]

$$\underbrace{p\left(\boldsymbol{x}|Y_{\text{obs},C}\right)}_{\text{posterior}} = \frac{\overbrace{p\left(Y_{\text{obs},C}|\mathfrak{M}(\boldsymbol{x}, C)\right)}^{\text{likelihood}}\overbrace{p(\boldsymbol{x})}^{\text{prior}}}{\underbrace{\int p\left(Y_{\text{obs},C}|\mathfrak{M}(\boldsymbol{x}, C)\right)p(\boldsymbol{x})\,\mathrm{d}\boldsymbol{x}}_{\text{evidence}}} \propto \underbrace{p\left(Y_{\text{obs},C}|\mathfrak{M}(\boldsymbol{x}, C)\right)p(\boldsymbol{x})}_{\text{unnormalized posterior}}. \tag{1}$$

In (1), the *posterior* $p\left(\boldsymbol{x}|Y_{\text{obs},C}\right)$ represents the unique solution of the Bayesian calibration task in the form of a probability density. It is a probability distribution over the input parameters $\boldsymbol{x}$ assigning a probability density to each input vector of how well the forward model $\mathfrak{M}(\boldsymbol{x}, C)$ evaluated with that model parameter combination represents the observation. The interest of the analyst is to find high posterior values and learn for which inputs they occur. The posterior density is usually not known in closed form, due to the implicit dependency on $\boldsymbol{x}$ in the forward model $\mathfrak{M}(\boldsymbol{x}, C)$ within the likelihood function. Nevertheless, the posterior density can be evaluated point-wise, which implies a forward simulation run for the particular choice of $\boldsymbol{x}$.

For computationally expensive models, a grid-based evaluation of the posterior in the entire input space $\Omega_{\boldsymbol{x}}$ is unfeasible. Due to the curse of dimensionality, this problem becomes especially amplified for $\dim(\boldsymbol{x}) \gg 1$. The numerical approximation of the posterior is hence usually conducted using more advanced algorithms which aim to exploit regions in the input space with high posterior density. In this work, we use the sequential Monte Carlo (SMC) method for this purpose but postpone a more detailed discussion of that algorithm and its numerical realization to the dedicated sections, to first focus on the continuous presentation of the Bayesian calibration problem.

The denominator $\int p\left(Y_{\text{obs},C}|\mathfrak{M}(\boldsymbol{x}, C)\right) p(\boldsymbol{x})\,\mathrm{d}\boldsymbol{x}$, respectively *evidence* in (1) acts as a normalizing constant for the posterior, such that it becomes a valid density function in $\boldsymbol{x}$ which integrates to one on $\Omega_{\boldsymbol{x}}$. Nevertheless, the evidence is mostly not computed explicitly, as it involves potentially high dimensional integration over $\Omega_{\boldsymbol{x}}$. Consequently, most numerical algorithms operate on the *unnormalized posterior* or its logarithm and take care of the normalization in an easier to compute post-processing step. Given the posterior distribution or a numerical representation in form of samples or an approximating distribution, further statistics or point estimates can be calculated and derived.

Remark 1 (Marginalization) Sometimes one might be interested in the density over a subset of variables, averaging over the remaining parameters. This can be achieved by so-called *marginalization*. A *marginal* represent a projection of the high-dimensional density, e.g., $p\left(\boldsymbol{x}_i, \boldsymbol{x}_j\right)$, for a selected subset of parameters $\boldsymbol{x}_i$, and reflects the average effect of all other parameters $\boldsymbol{x}_j$ on the density over parameter subset $\boldsymbol{x}_i$. The marginal distribution is then expressed by the following integration

$$p(\boldsymbol{x}_i) = \int p\left(\boldsymbol{x}_i, \boldsymbol{x}_j\right) \mathrm{d}\boldsymbol{x}_j = \int p\left(\boldsymbol{x}_i|\boldsymbol{x}_j\right) p\left(\boldsymbol{x}_j\right) \mathrm{d}\boldsymbol{x}_j = \mathbb{E}_{\boldsymbol{x}_j}\left[p\left(\boldsymbol{x}_i|\boldsymbol{x}_j\right)\right]. \tag{2}$$

One example are projections of a higher-dimensional posterior $p\left(\boldsymbol{x}_i, \boldsymbol{x}_j|Y_{\text{obs},C}\right)$ to a marginal posterior $p\left(\boldsymbol{x}_i|Y_{\text{obs},C}\right)$ such that the analyst can investigate the posterior in $\boldsymbol{x}_i$ averaged over the effect of $\boldsymbol{x}_j$. This enables us to regard and print marginal posterior distributions with $i < 3$ in result plots.

Bayesian calibration under uncertainty

After the basic concepts of Bayesian calibration have been presented, we want to extend the ideas to the case of non-controllable, uncertain conditions that influence the model $\mathfrak{M}$. Those are summarized in the vector $\boldsymbol{\theta}$. We assume that $\boldsymbol{\theta}$ is not part of the model input variables $\boldsymbol{x}$ that we want to calibrate. Instead, it represents inherently uncertain external conditions, e.g., of the experimental set-up, that we cannot fully control at the

time of the analysis. Furthermore, we assume that these conditions are subject to uncertainties expressed by a distribution $p(\boldsymbol{\theta})$ and that the computational forward model is also dependent on $\boldsymbol{\theta}$ in the sense of $\mathfrak{M}(\boldsymbol{x}, \boldsymbol{\theta}, C)$.

The calibration problem under uncertainty can then be formulated in two steps [18,19]. First, we naively compose a Bayesian calibration problem in analogy to (1), with the only difference that the model is also dependent on $\boldsymbol{\theta}$. Consequently, the posterior $p\left(\boldsymbol{x}|\boldsymbol{\theta}, Y_{\text{obs},C}\right)$ is conditionally dependent on $\boldsymbol{\theta}$, as demonstrated in (3a). In a second step, we can then average over the effect of the uncertain conditions $\boldsymbol{\theta}$ by taking the expectation of the previous posterior $\mathbb{E}_{\boldsymbol{\theta}}\left[p\left(\boldsymbol{x}|\boldsymbol{\theta}, Y_{\text{obs},C}\right)\right]$ with respect to the density $p(\boldsymbol{\theta})$ as shown in (3b). The resulting modified posterior, which accounts for the average effect of the additional uncertainty introduced by $\boldsymbol{\theta}$ is then denoted by $q\left(\boldsymbol{x}|Y_{\text{obs},C}\right)$ and is different from the former posterior $p\left(\boldsymbol{x}|Y_{\text{obs},C}\right)$ which did not incorporate these additional uncertainties.

$$p\left(\boldsymbol{x}|\boldsymbol{\theta}, Y_{\text{obs},C}\right) \propto p\left(Y_{\text{obs},C}|\mathfrak{M}(\boldsymbol{x}, \boldsymbol{\theta}, C)\right) p(\boldsymbol{x}) \tag{3a}$$

$$\begin{aligned} q\left(\boldsymbol{x}|Y_{\text{obs},C}\right) = \mathbb{E}_{\boldsymbol{\theta}}\left[p\left(\boldsymbol{x}|\boldsymbol{\theta}, Y_{\text{obs},C}\right)\right] &= \int \underbrace{p\left(\boldsymbol{x}|\boldsymbol{\theta}, Y_{\text{obs},C}\right) p(\boldsymbol{\theta})}_{\substack{\text{extended posterior:} \\ p\left(\boldsymbol{x},\boldsymbol{\theta}|Y_{\text{obs},C}\right)}} \mathrm{d}\boldsymbol{\theta} \\ &\propto \int \underbrace{p\left(Y_{\text{obs},C}|\mathfrak{M}(\boldsymbol{x}, \boldsymbol{\theta}, C)\right) p(\boldsymbol{x}) p(\boldsymbol{\theta})}_{\text{unnormalized extended posterior}} \mathrm{d}\boldsymbol{\theta} \end{aligned} \tag{3b}$$

Another interpretation of (3b) is the marginalization of the *extended posterior* $p\left(\boldsymbol{x}, \boldsymbol{\theta}|Y_{\text{obs},C}\right)$ with respect to the uncertain conditions $\boldsymbol{\theta}$. Later-on, we show that the sequential Monte Carlo (SMC) algorithm allows simple operations on the *unnormalized extended posterior*, analogous to the *unnormalized posterior* from (1) if no additional uncertainties are present. SMC offers the possibility to conduct the necessary marginalization of $\boldsymbol{\theta}$ as a cheap post-processing step.

Remark 2 (Point estimates and moments of the posterior) Given a potentially high dimensional and complex posterior density, there is often the desire to represent its characteristics by simpler, e.g., scalar quantities. The most intuitive approach, especially coming from the mindset of deterministic optimization, is to look for the maximum a posteriori (MAP) estimate. It represents the combination of parameters that lead to the highest posterior density. Further, the maximum likelihood estimate (ML) is interesting to isolate the model feedback from prior assumptions. It is analog to the MAP for the assumptions of uniform priors. Also statistics of the posterior as the posterior mean (PM) and variance can be used for its simplified quantification. Other than point estimates, also a region of values with highest posterior density can be determined. This region is then characterized by holding a certain probability mass fraction of the posterior and is often called *percentile*.

Selecting a likelihood model

The evaluation of the likelihood function represents the computationally expensive part of the Bayesian calibration as a forward simulation run has to be conducted for every evaluation of the likelihood with respect to $\mathfrak{M}(\boldsymbol{x}, \boldsymbol{\theta}, C)$. The likelihood is a probabilistic model for the discrepancy $\mathfrak{D}$ between experimental data $Y_{\text{obs},C}$ and forward model output $\mathfrak{M}(\boldsymbol{x}, \boldsymbol{\theta}, C)$, written as $\mathfrak{D} = \mathfrak{D}(Y_{\text{obs},C}, \mathfrak{M}(\boldsymbol{x}, \boldsymbol{\theta}, C))$. It usually models the statistical behavior of experimental noise and modeling errors. It returns the probability density of the

experimental data for a given choice of simulation model. This means that it is centered around the forward model results. Usually, only one experiment is observed.

While many different likelihood models exist [20,21], we chose the common case of a conditionally independent Gaussian likelihood model with static noise-variance σ_{N}^2. This choice implies that we assume that the scattering of the measured data $Y_{\mathrm{obs},C}$ can be well-explained by a normal distribution which is centered around the simulation output Y_C with variance σ_{N}^2. Here conditional independence means that the measured noise in y_{obs,c_1} does not influence the noise in y_{obs,c_2}, with c_1 and c_2 being two different coordinates.

The conditionally independent Gaussian static likelihood model is given by

$$p\left(Y_{\mathrm{obs},C}|\mathfrak{M}\left(\boldsymbol{x},\boldsymbol{\theta},C\right)\right)=\frac{1}{\sqrt{\left(2\pi\sigma_{\mathrm{N}}^2\right)^n}}\exp\left(-\frac{\mathfrak{D}^2\left(\mathfrak{M}\left(\boldsymbol{x},\boldsymbol{\theta},C\right),Y_{\mathrm{obs},C}\right)}{2\sigma_{\mathrm{N}}^2}\right), \tag{4}$$

wherein n is the dimension of the measurement $Y_{\mathrm{obs},C}$. In the simplest case it is the total number of individual measurements. As most inverse iterators operate on the logarithm of the densities for better numerical condition, we also provide the logarithmic version of (4), which is often abbreviated by $\mathcal{L}(\boldsymbol{x},\boldsymbol{\theta})$ resulting in

$$\mathcal{L}(\boldsymbol{x},\boldsymbol{\theta})=-\frac{n}{2}\log(2\pi\sigma_{\mathrm{N}}^2)-\frac{\mathfrak{D}^2}{2\sigma_{\mathrm{N}}^2}. \tag{5}$$

Discrepancy measures between interfaces

In selecting a likelihood model the immediate question arises about how to define a discrepancy measure $\mathfrak{D}$ between the forward model and experimental results. This becomes especially intricate when the experimental images do not provide real displacements for individual material points, i.e., in this sense prohibit a point-wise correspondence of the geometrical objects. This constraint almost only allows for comparisons of edges, boundaries and interfaces in the image data that can usually be identified depending on their contrast. This step is called *segmentation* of the image data. More detailed information on segmentation approaches etc. are out of scope for this work. As a result of the segmentation process one obtains a geometric representation of interfaces between different subdomains in the images.

In the following, we present three different discrepancy measures that can be used when working with such kind of image data, namely *Euclidean distance at measurement points*, *closest point projection distance* and *reproducing kernel Hilbert space norm*. Figure 1 shows sketches of the discussed distance measure definitions in 2D. The sketches in Fig. 1 are related to the type of problem, of fluid–biofilm interaction, exemplarily analyzed in the numerical examples. The methods are not bound to this type of problem and can be applied to different topologies or isolated shape characteristics.

Euclidean distance at measurement points The first approach is an Euclidean distance measure as presented in [12]. At several selected points on the experimentally observed biofilm surface, specific directions are chosen and the distance to the corresponding deformed interface resulting from the forward model simulation is measured. As discussed in [12] measurement points should be selected in regions of significant, characteristic displacements. Measurement directions should be chosen normal to the observed interface. (See Fig. 1a with predefined directions in blue.) These distances are summarized in a vector of length n_{mp}. They represent the distance measure between the forward model evaluation and the experimental observation. The resulting distance measure $\mathfrak{D}_{\mathrm{mp}}$ is then

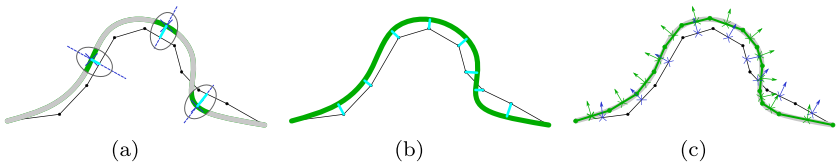

Fig. 1 Exemplary 2D sketches for different types of discrepancy measures between experiment (green) and discretized forward model (black). Portions of the observed interface that are accounted for are given in green and unconsidered portions are given in gray. **a** Euclidean distances d^i_{mp} at measurement points in preset directions in light blue, **b** closest point projection distances d^i_{cpp} for all nodes in light blue, **c** triangulation centers $\boldsymbol{c}_i$ as crosses and normal vectors $\boldsymbol{n}_i$ of equal length as arrows for triangulations of the experimentally observed interface in green and the forward model result in blue. Detailed explanation in text below

defined via the L_2-norm of the distance vector

$$\mathfrak{D}_{\text{mp}} = \left\| \begin{bmatrix} d^1_{\text{mp}} \\ \vdots \\ d^{n_{\text{mp}}}_{\text{mp}} \end{bmatrix} \right\|_2 . \tag{6}$$

This procedure is especially well suited if the observed experimental measurements have different reliability throughout the regarded interface, e.g., due to the particular physics or imaging peculiarities as only a point-wise and no full representation of the interface must be measured (i.e., the gray parts in Fig. 1a are not part of the analysis). By a meaningful selection of measurement points, where significant deformation takes place and the data is trusted, the analyst has direct control over which data is being processed.

Closest point projection Another approach for a distance between curves or surfaces is the closest point projection distance for a selected number of points on the interface in the discretized forward model. In the case of finite element models, a suitable choice for the points are the Gauss points or the mesh nodes, as pictured and used here, on the regarded interface. The closest point projection distance to the experimental result is determined based on the segmented image of the interface, as shown in Fig. 1b, and used in the distance vector with the length of the number of interface nodes n_{in}. Afterwards, we define the L_2-norm of the distance vector as the distance measure $\mathfrak{D}_{\text{cpp}}$ with

$$\mathfrak{D}_{\text{cpp}} = \left\| \begin{bmatrix} d^1_{\text{cpp}} \\ \vdots \\ d^{n_{\text{in}}}_{\text{cpp}} \end{bmatrix} \right\|_2 . \tag{7}$$

We choose the discretization of the finite element model and define the distance vector then by computing the distance of the closest point projection w.r.t. the experimental surface or interface.

Inner product in reproducing kernel Hilbert space (RKHS) A third, statistically motivated discrepancy measure is formulated as a *reproducing kernel Hilbert space (RKHS)* norm. It does not only take into account the location of discretization points, but also the orientation of the surface elements in space. Before presenting our specific variant, a more general mathematical foundation of the measure is outlined in the following.

Distance measures $\mathfrak{D}$ between two curves (or surfaces) $\boldsymbol{f}_1, \boldsymbol{f}_2$, can be elegantly defined by an inner product of the distance function $\boldsymbol{d_f}(\boldsymbol{s}) = \boldsymbol{f}_1 - \boldsymbol{f}_2$ in an associated Hilbert space $\mathcal{H}$ as demonstrated in (8a). Simply speaking, a Hilbert space is a vector space and can be seen as the natural extension of the Euclidean space to arbitrary dimensions. The

inner product directly induces a norm according to (8b).

$$\langle \boldsymbol{d_f}(\boldsymbol{s}), \boldsymbol{d_f}(\boldsymbol{s})\rangle_{\mathcal{H}} = \int \boldsymbol{d_f}(\boldsymbol{s})\boldsymbol{w}(\boldsymbol{s})\boldsymbol{d_f}(\boldsymbol{s})d\boldsymbol{s} \tag{8a}$$

$$\mathfrak{D}_{\mathcal{H}} = \left\|\boldsymbol{d_f}(\boldsymbol{s})\right\|_{\mathcal{H}} = \sqrt{\langle \boldsymbol{d_f}(\boldsymbol{s}), \boldsymbol{d_f}(\boldsymbol{s})\rangle_{\mathcal{H}}} \tag{8b}$$

Here, $\boldsymbol{w}(\boldsymbol{s}) > 0$ is an optional weighting function. A special case of a Hilbert space $\mathcal{H}$ is the so-called *reproducing kernel Hilbert space (RKHS)*, here denoted by $\mathcal{V}$. We omit a full description of RKHSs and only present the most important concepts in this work but point the interested reader to [22] for a comprehensive derivation and description of the latter. Some further details of the RKHS framework are presented in the appendix. An RKHS $\mathcal{V}$ is a Hilbert space that is equipped with a *reproducing kernel* $\boldsymbol{k}(\boldsymbol{x}, \boldsymbol{y})$ and the inner product

$$\langle \boldsymbol{d_f}(\boldsymbol{x}), \boldsymbol{d_f}(\boldsymbol{x})\rangle_{\mathcal{V}} = \int \boldsymbol{d_f}(\boldsymbol{x})\boldsymbol{k}(\boldsymbol{x}, \boldsymbol{x}')\boldsymbol{d_f}(\boldsymbol{x}')d\boldsymbol{x}d\boldsymbol{x}' \tag{9a}$$

$$\mathfrak{D}_{\mathcal{V}} = \left\|\boldsymbol{d_f}(\boldsymbol{x})\right\|_{\mathcal{V}} = \sqrt{\langle \boldsymbol{d_f}(\boldsymbol{x}), \boldsymbol{d_f}(\boldsymbol{x})\rangle_{\mathcal{V}}}. \tag{9b}$$

The inner product of the difference in the normal vectors of two functions describing two interfaces in (10b) results in a sensitive distance measure that also accounts for the orientation of the interfaces. The distance of the function values is encoded in the kernel function which expresses the statistical correlation between the functions. For the kernel we choose the radial basis function (RBF) in (10b) which takes the location vectors, respectively the function values $\boldsymbol{f}(\boldsymbol{s})$ as arguments and returns their correlation. The expression is also known under the term *surface currents* [23] and was already successfully applied for inverse analysis in [6,24]

$$\boldsymbol{d_n}(\boldsymbol{s}) = \boldsymbol{n_{f_1}}(\boldsymbol{s}) - \boldsymbol{n_{f_2}}(\boldsymbol{s}) \tag{10a}$$

$$\mathfrak{D}_{\mathcal{V},\mathrm{sc}} = \sqrt{\langle \boldsymbol{d_n}, \boldsymbol{d_n}\rangle_{\mathcal{V}}},$$

$$\text{with } k\left(\boldsymbol{f}_1, \boldsymbol{f}_2\right) = \exp\left(-\frac{\left\|\boldsymbol{d_f}\right\|_2^2}{2\sigma_{\mathrm{W}}^2}\right) \tag{10b}$$

We want to highlight that (9a) allows for many other definitions of $\boldsymbol{d}$ and $\boldsymbol{k}$ which can be used to emphasize special features of the investigated data. Further examples would be outside the scope of this article. But they might be interesting to emphasize other special features of the investigated data.

The discrete representation of (10b), e.g., in a finite element simulation, for surfaces or curves are expressed in form of respective elements and meshes. In the simplest case those are interface triangles, resulting from linear tetrahedral elements in 3D, or interface lines, resulting from linear elements in the two-dimensional case. The interface triangles or lines have normal vectors $\boldsymbol{n}_{e_i\boldsymbol{f}_1,i}$,$\boldsymbol{n}_{e_j\boldsymbol{f}_2,j}$ and element-surface centers $\boldsymbol{c}_{e_i\boldsymbol{f}_1,i}$ and $\boldsymbol{c}_{e_j\boldsymbol{f}_2,j}$. Normals and center points can be directly determined from the discretization. The difference vector of the two normal vectors is written as $\boldsymbol{d}_{\boldsymbol{n},e} = \boldsymbol{n}_{e_i\boldsymbol{f}_1,i} - \boldsymbol{n}_{e_j\boldsymbol{f}_2,j}$. The approximation for (10b) follows as a double sum over the elements from $\boldsymbol{f}_1$ and elements from $\boldsymbol{f}_2$

$$\begin{aligned}\mathfrak{D}^2_{\mathcal{V},\mathrm{sc}} \approx \langle \boldsymbol{d}_{\boldsymbol{n},e}, \boldsymbol{d}_{\boldsymbol{n},e}\rangle_{\mathcal{V}} = \sum_{i=1}\sum_{j=1}\Big[&\boldsymbol{n}_{e_i\boldsymbol{f}_1,i}\cdot k\left(\boldsymbol{c}_{e_i\boldsymbol{f}_1,i}, \boldsymbol{c}_{e_j\boldsymbol{f}_2,j}\right)\boldsymbol{n}_{e_j\boldsymbol{f}_2,j}\\ &- 2\boldsymbol{n}_{e_i\boldsymbol{f}_1,i}\cdot k\left(\boldsymbol{c}_{e_i\boldsymbol{f}_1,i}, \boldsymbol{c}_{e_j\boldsymbol{f}_2,j}\right)\boldsymbol{n}_{e_j\boldsymbol{f}_2,j} + \boldsymbol{n}_{e_i\boldsymbol{f}_1,i}\cdot k\left(\boldsymbol{c}_{e_i\boldsymbol{f}_1,i}, \boldsymbol{c}_{e_j\boldsymbol{f}_2,j}\right)\boldsymbol{n}_{e_j\boldsymbol{f}_2,j}\Big]\end{aligned} \tag{11}$$

Using the mechanism of an RKHS for a definition of a surface distance measure has some advantages, that we want to emphasize. First, such a measure allows comparing the whole geometry rather than distances at selected points. It is further a more flexible approach with exchangeable kernel and therefore associated RKHS. It provides a solid mathematical foundation and still gives the analyst the flexibility of choosing an appropriate kernel that will emphasize geometrical features of choice. The kernel parameters that can be referred to as hyperparameters can be made subject to optimization in the calibration approach and therefore the RKHS approach allows seamless integration into a probabilistic framework.

Remark 3 (RKHS interpretation) The interpretation of a distance measure as an RKHS with respective norm allows a conclusive mathematical foundation. In fact also the Euclidean distance and the closest point projection distance can be interpreted as different RKHS. These have very specific kernels. Therefore, their re-interpretation is omitted. Generally, a multitude of RKHSs with respective kernels can be designed in an elegant mathematical manner to emphasize different characteristics of the image. One example could be to use a weighting depending on the distance to the closest Dirichlet boundary condition.

Remark 4 (Three-dimensional geometry) Although we will only present two-dimensional applications, the distance measures are equivalently applicable to three-dimensional use cases. As the evaluation of the similarity measures is the only step where geometry is evaluated, this generalization to 3D is obviously also true for the whole approach presented in this work. If accurate three-dimensional images are available from the experiment it would be preferable to use those to increase model accuracy and therefore the quality of the inverse analysis.

Bayesian calibration—realization and algorithmic aspects

After the mathematical basis for the inverse problem was presented above, we elaborate on the realization and algorithmic aspects as well as computational efficiency of the proposed approach. Several algorithms exist to find an approximation to the posterior distributions in (1) and (3b). Common strategies are particle methods that can be achieved through the Markov Chain Monte Carlo method (MCMC) [25], specifically by the well-known Metropolis-Hastings algorithm and its variants [26]. Further methods are based on Importance Sampling [27,28] and especially the family of Sequential Monte Carlo (SMC) methods [29,30]. Other, more recent strategies are based on Variational Inference [31,32], where a parameterized distribution is optimized to match the true posterior as close as possible in a given norm. Here, we choose an SMC method as an established, state-of-the-art method.

Numerical approximation via sequential Monte Carlo (SMC) sampling

An efficient approach is needed to approximate the unnormalized posteriors of the Bayesian calibration problem (1), (3b) and their normalization. While a grid-based approximation of the posterior is feasible for low dimensional parameters $\boldsymbol{x}$, the necessary amount of grid-based evaluations grows exponentially with the dimension of $\boldsymbol{x}$ and SMC methods become significantly more efficient as they exploit regions of high density. Sequential

Monte Carlo (SMC) methods are popular sampling methods to efficiently explore a probability distribution π for which no closed expression exists.

The result of the SMC sampler is a particle representation $\delta_{\boldsymbol{x}^{(i)}}$ of π with associated weights $w^{(i)}$ in the form of

$$\pi\left(\boldsymbol{x}\right) \approx \sum_{i=1}^{N} w^{(i)} \delta_{\boldsymbol{x}^{(i)}}\left(\boldsymbol{x}\right). \tag{12}$$

Therein every particle has a location and weight $\left\{\boldsymbol{x}^{(i)}, w^{(i)}\right\}_{i=1}^{N}$. It is further known [33, 34] that with this approximation any integral over an integrable function $h\left(\boldsymbol{x}^{(i)}\right)$ can be approximated by a sum that converges to the integral

$$\sum_{i=1}^{N} w^{(i)} h\left(\boldsymbol{x}^{(i)}\right) \rightarrow \int h\left(\boldsymbol{x}\right) \pi\left(\boldsymbol{x}\right) \mathrm{d}\boldsymbol{x} \qquad \text{almost surely.} \tag{13}$$

Specifically, we use an SMC method [35] which sequentially blends over from a particle representation of a predefined prior distribution to a particle representation of the actual posterior distribution. A convenient aspect of the particle representation in (12) is that they allow for a straightforward approximation of integrals (13), as they appear in marginal distributions (2). This is especially useful for Bayesian calibration under uncertainty and the associated integration in (3b). Here, the numerical integration is conducted by simply ignoring the dependency on $\boldsymbol{\theta}$ in the particle representation.

The SMC algorithm we use in this work uses an adaptive step length based on [33, 34, 36]. Herein, a control parameter ζ for the *effective sample size* (ESS) is used to control step length. The ESS is defined as

$$\mathrm{ESS} = \frac{1}{\sum_{i=1}^{N}\left(w^{(i)}\right)^2} \tag{14}$$

and is a measure for the current weight distribution. The ESS represents how well the probability density mass is distributed amongst the used particles.

The presentation of the SMC algorithm is compactly demonstrated in the pseudo-algorithm 1 and described in remark 5. For more details, the interested reader is referred to [29, 30, 34].

Remark 5 (Description of SMC algorithm) An SMC algorithm generally starts with the steps to draw an initial set of particles from the prior distribution and initially equally weigh them. Then it needs to iteratively find a suitable step size and reweigh the particles. Resampling becomes necessary if too few particles carry too much weight of the distribution and likewise many particles lose significance. The particles are sequentially rejuvenated according to the new control parameter γ and therefore new intermediate distribution (15). The rejuvenation step is carried out with a scaled covariance of the current step as demonstrated in [37] based on the acceptance rate of the Metropolis-Hastings algorithm used for rejuvenation. The Metropolis-Hastings algorithm is a Markov Chain Monte Carlo (MCMC) sampler [38], of which we omit the presentation for the sake of compactness. It is used to move the particles according to the new intermediate distribution. Reweighting, rejuvenation and possibly resampling are iteratively repeated until the intermediate distribution blends into the posterior, i.e. $\gamma = 1$, which is the necessary last step if no other suitable γ can be found. For the sake of a proper probability density, i.e. integration to 1, the resulting weights are finally normalized.

Algorithm 1 Sequential Monte Carlo algorithm with adaptive step length.

Draw N particles from prior distribution
Uniformly weight particles w_0
Set step counter $s = 1$, and control parameter $\gamma = 0$
while $\gamma < 1.0$ **do**
  Find γ_s so that $\mathrm{ESS}_s \approx \zeta \mathrm{ESS}_{s-1}$ by reweighting $w_s = w_{s-1} \frac{\pi_{(s-1),\gamma_s}}{\pi_{(s-1),\gamma_{(s-1)}}}$
  if no $\gamma_s < 1.0$ can be found **then**
    Set $\gamma = 1.0$ and reweight
    Do final step towards posterior $\pi_{n_{\mathrm{SMC}},1.0}$
  end if
  if $\mathrm{ESS}_s < \mathrm{ESS}_{\min}$ **then**
    Resample
  end if
  Rejuvenate with n_{rej} MCMC iterations on the likelihood model to get $\pi_{s,\gamma}$
  Raise step counter $s = s + 1$
end while
Normalize weights

The so-called *tempering strategy* that defines the transition from the prior to the posterior as a sequence is written as

$$\pi_{s,\gamma}(\boldsymbol{x}) = \exp(\gamma \mathfrak{L}(\boldsymbol{x})) p(\boldsymbol{x}) \tag{15}$$

with the logarithmic likelihood $\mathfrak{L}(\boldsymbol{x})$ as introduced in (5) and the prior $p(\boldsymbol{x})$. Finally, after reaching $\gamma = 1$ the particle approximation has blended over into one for the posterior distribution.

Approximation of the log-likelihood via Gaussian process regression

To efficiently evaluate the likelihood function in (15) we use a Gaussian process (GP) regression model [39] for the log-likelihood function (5) that can be trained on a controllable amount of forward model evaluations. The main idea is that for a given computational budget, represented by the number of forward model runs, the approximation error of the surrogate is considerably smaller than the error in the SMC posterior approximation for the same number of forward simulation runs. A similar approach, where the model output is directly used as data to train a Gaussian process regression model as a surrogate for Bayesian calibration was used in [1]. Gaussian processes are often used to generate regression models and therefore a brief summary of the core equations is presented in the appendix. The presented overall approach would also work with different regression approaches as linear or spline interpolation or in case of cheap enough forward models would also work directly on the forward model.

We use the log-likelihood $\mathfrak{L}(\boldsymbol{x})$ of the Bayesian calibration problem as presented in (5) to train our GP upon. This gives the advantage that the regression models do not need to fulfill positiveness constraints. This would be the case if the GP was trained on the unnormalized posterior or likelihood directly. Another advantage of learning the log-likelihood function in contrast to learning the simulation response is that the log-likelihood is a scalar function.

Training data $\mathcal{D}$ are input–output pairs of values that are known about the process and the regression model can be based on. In our case, we can evaluate the forward model with any choice of model parameters $\boldsymbol{x}$, compare it to the observed experiment and determine

the logarithm of the log-likelihood $\mathfrak{L}$ (5). To simplify notation we specify the training data outputs to a vector of log-likelihoods $\mathfrak{L}_{\text{train}}$ at different coordinates $\boldsymbol{x}_{\text{train}}$. Thus, we are free to choose any input batch $\boldsymbol{x}_{\text{train}}$ and compute resulting output $\mathfrak{L}_{\text{train}}$ according to our computational budget. The generation of the training data $\mathcal{D}$ for the Gaussian process regression causes the highest computational costs in the inverse analysis, as for every training tuple $\{\mathfrak{L}_{\text{train},i}, \boldsymbol{x}_{\text{train},i}\}$ one forward model evaluation is required, due to the dependency of the log-likelihood (5) on the forward model.

Some further advantages of the surrogate approach are an a priori controllable amount of simulation runs, which can also be conducted in parallel, in contrast to the batch-sequential model evaluations that the SMC would impose on the forward model evaluations in a direct application. Once the surrogate is generated, the SMC algorithm can run without the risk of encountering non-converging or failing forward simulations.

To generate the training data $\mathcal{D}$ we choose a space-filling design strategy, namely a quasi-random Sobol sequence [40,41]. The Sobol sequence has the advantage to have superior uniformity properties [42] and additionally allows for generating further sequential points that still share the space filling properties.

Remark 6 (Dimensions in GP approach) The number of necessary training tuples for desired surrogate accuracy is dependent on the complexity of the function, the type of (space-filling) experimental design and the dimension of the function. The required amount of training data grows exponentially with the dimension of the problem (curse of dimensionality), so that for higher dimensions (a rough guideline might be $\dim(\boldsymbol{x}) > 15$) direct sampling (using more advanced strategies that can incorporate gradient information of the model w.r.t. the inputs $\boldsymbol{x}$) becomes more efficient.

Implementation aspects

The implementation of the algorithm described above was done in the Python software framework *QUEENS* [43]. Herein, the Gaussian process regression module *GPy* [44] was used for the construction of the Gaussian process surrogates. The sequential Monte Carlo algorithm based on algorithm 1 is also implemented in *QUEENS*. For processing of forward model results the Python package *vtk* for "The Visualization Toolkit" was used [45]. Some of the following visualizations were generated with *Seaborn* [46] and *Matplotlib* [47]. Parallel axis plots are generated with plotly [48]. We furthermore use *PyTorch* [49] for the generation of the Sobol sequences. The forward models were solved with the in-house C++ research code BACI [50].

Numerical examples

In this section, we present our Bayesian calibration approach for a coupled fluid–structure interaction problem. We demonstrate the approach with generated data to better assess its individual steps. Our focus lies on the presentation of the proposed approach and some general characteristics in the resulting posteriors. In application with real-world data, the procedure can be used without any changes. The computational mechanics models in the examples are schematic models for fluid-biofilm interaction that is the motivation for our research. Therein the fluid–solid interface deforms as a consequence of the interaction. A further description of the experiments is moved to the appendix as we want to focus on the model here. In the following examples, we calibrate biofilm material properties

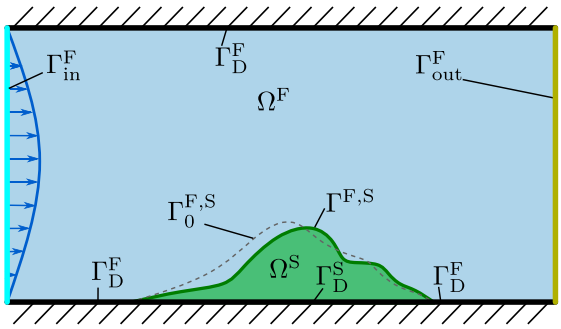

Fig. 2 Schematic of problem setup with domain and interface names. A biofilm (green domain) is grown on the flow cell floor and is interacting with a flowing liquid (blue domain) that is providing nutrients to and also deforming the biofilm which in return is changing the flow field. Undeformed (gray dotted line) and deformed biofilm interface. Inflow (teal) and outflow (yellow) boundaries of the flow cell model are also shown

under partially uncertain experimental conditions. For the numerical demonstrations we use the fluid-solid interaction (FSI) between incompressible Navier–Stokes flow and a hyperelastic nonlinear solid material model which is briefly introduced in the appendix. Although the presented calibration approach is equivalently applicable for single field problems with deformable boundaries we take the challenge of a coupled multi-physics model of FSI because we want to advertise the benefit of the approach in such applications. A variety of different models for biofilms are available and also further effects can be included (see, e.g., [12,51]), which would just lead to different forward models.

Problem setup

The calibration is performed for hyperelastic material properties of the solid domain for which we will calibrate the two parameters of a Saint-Venant Kirchhoff material model. For the given setup of FSI models for biofilms and the biofilm flow cell data, the location of the fluid-biofilm interface is the primary data available and therefore used for comparison. A schematic sketch of the problem setup is drawn in Fig. 2. For easier demonstration we first investigate a two-dimensional calibration problem ($\dim(\boldsymbol{x}) = 2$) without experimental uncertainties ($\dim(\boldsymbol{\theta}) = 0$) and then move on to more complex examples.

We chose the same problem setup as presented in [12]. The biofilm geometry is inspired by analyses done on experimental results in [11,14]. The model domain represents a two-dimensional channel with dimensions $1\,\mathrm{mm} \times 2\,\mathrm{mm}$, where horizontal fluid flow with parabolic profile is enforced from the left boundary (see $\Gamma^{\mathrm{F}}_{\mathrm{in}}$ in Fig. 2) with a maximal volume rate of $\dot{V}_{\mathrm{in}} = 100\,\mathrm{mm}^2/\mathrm{s}$. The solid biofilm (green) is attached to the channel floor. A no-slip condition for the fluid is used on the channel floor and top boundary as well as the biofilm on the channel floor (see $\Gamma^{\mathrm{F}}_{\mathrm{D}}$ and $\Gamma^{\mathrm{S}}_{\mathrm{D}}$ in Fig. 2) and a horizontal outflow is enforced on the right edge (see $\Gamma^{\mathrm{F}}_{\mathrm{out}}$ in Fig. 2). These boundary conditions are modeled via Dirichlet boundary conditions on the fluid velocity (and solid displacement accordingly) and respective free outflow in horizontal direction. The horizontal condition represents the ongoing empty channel left and right from the modeled domain.

To generate the artificial experimental data, we use a forward simulation of the fluid-biofilm interaction with a Saint-Venant-Kirchhoff material model for the solid biofilm domain. The material is characterized by two parameters, namely Young's modulus E and

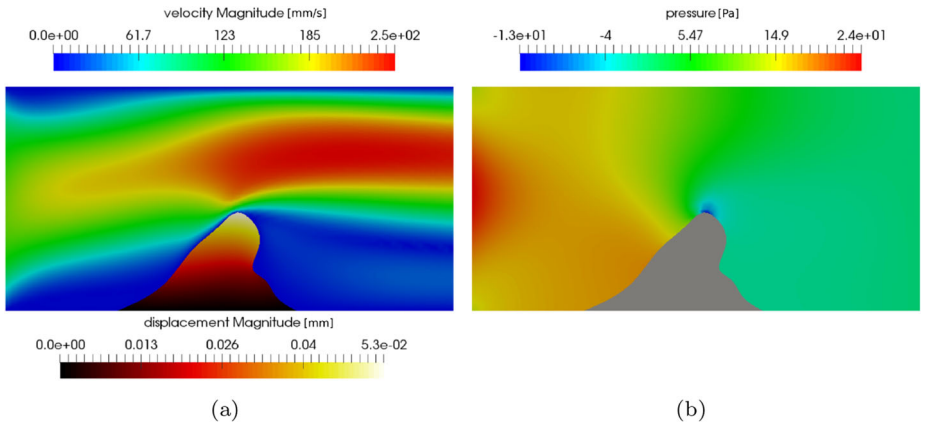

Fig. 3 Field solutions of the ground truth simulation with parameters $\boldsymbol{x}_{\text{gt}}$ on the deformed geometry. **a** Fluid velocity magnitude, solid displacement magnitude. **b** Fluid pressure solution

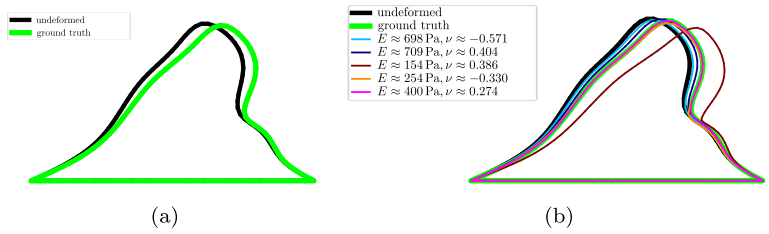

Fig. 4 Exemplary forward model results for deformed interface shapes for different input parameter samples compared to the result with ground truth $\boldsymbol{x}_{\text{gt}} = [\nu = 0.3,\ E = 400\,\text{Pa}]^{\mathsf{T}}$ as input and the undeformed state

Poisson's ratio ν. We summarize the chosen input parameters, used for the generation of the data, in form of the ground truth vector $\boldsymbol{x}_{\text{gt}} = \left[\nu = 0.3, E = 400\,\text{Pa}\right]^{\mathsf{T}}$. The fluid has a dynamic viscosity of $\mu^{\text{F}} = 10^{-3}$ Pa s and a density of $\rho^{\text{F}} = 10^{3}\,\text{kg/m}^3$ as a model for water. The biofilm has the same density as the fluid. The solution of the velocity and pressure field of the fluid and displacement field of the biofilm is depicted in Fig. 3 for the regarded quasi-steady deformed state in the ground truth forward model evaluation. As a reaction to the load imposed by the fluid inflow boundary condition, the solid bends towards the right as it is plotted in Fig. 4. In Fig. 4a we see the artificial observation data $Y_{\text{obs},C}$ as the result of the reference simulation with ground truth values $\boldsymbol{x}_{\text{gt}}$. $Y_{\text{obs},C}$ represents the deformed location (green) of the interface in this example for one single point in time C. In Fig. 4b we plot the results for some exemplary parameter combinations additionally.

Likelihood response surface for different discrepancy measures

In a first step, we compare the effect of the different discrepancy measures as introduced. We directly approximate the log-likelihood by the posterior mean function of a Gaussian process surrogate and use the discussed discrepancy measures. Additionally, we also provide the posterior standard deviation of the GP to quantify the remaining uncertainty in the surrogate. All surrogate models for the log-likelihood function resulting for the different discrepancy measures use the same training input that was sampled with a quasi-random Sobol sequence to yield a space-filling training design. The training inputs are different parameters in the forward model and the resulting forward simulations.

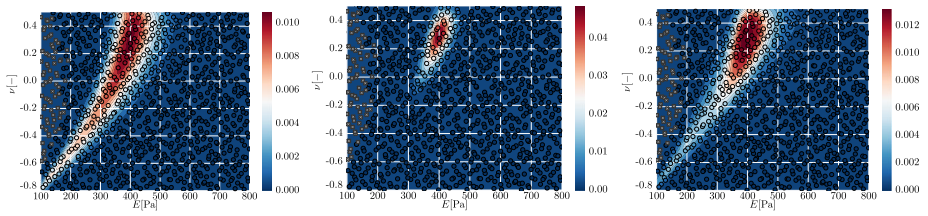

Fig. 5 Likelihoods for different surface measure distances with $n_{\text{train}} = 1000$. **a** Euclidean distance at measurement points, **b** closest point projection distances, **c** RKHS norm. Normalized for better comparability. Training samples as circles for successful and gray crosses (on the left side) for failed forward model evaluations

For an estimation of a suitable σ_{N} in the likelihood model (4) the known resolution $\approx 8\,\mu$m of OCT [14,15] is considered. The noise standard deviation is assumed to be in the same order of magnitude, such that $\sigma_{\text{N}} = 0.01$ mm is used in the following. OCT resolution and standard deviation in the likelihood model are not expected to be equal. A further discussion is omitted here, as the demonstration here works independent of the choice and an expressive value can only be found related to real data and chosen image segmentation. For the RKHS norm we need two parameters σ_{N} and σ_{W}. An estimation of the length scale σ_{W} for the RBF kernel in the RKHS approach in (10b) is made as $\sigma_{\text{W}} = 0.005$ mm, being approximately 10% of the maximal displacement magnitude (see Fig. 3(a)).

The resulting regression models for the likelihoods are shown in Fig. 5 for $n_{\text{train}} = 1000$ training points with a Matérn 3/2 kernel (see appendix on GP, Eq. (27) for details). In general, the likelihood over the parameters can be understood as a score value of how well the forward model response with respective parameters leads to similar results compared to the reference data. A discussion and interpretation of the figure will follow below. For this first comparison, we just use this large number of training points and postpone the discussion on the GP convergence over n_{train} to the case only using the RKHS norm measure. For the distribution of the measurement points in this comparison, the reader is referred to [12]. In Fig. 5 the fields of the likelihoods are determined from the logarithmic likelihoods and those fields are normalized in the plots for better comparability. Parameter combinations that led to failed forward model evaluations are marked by gray crosses in the following figures. For our setup, the failing simulations occurred for low values of Young's modulus (located on the left side of the plots) representing soft biofilm material, which lead to large mesh distortions in the ALE FSI approach. For the sake of comparability, the respective logarithmic likelihoods are plotted in Fig. 6 and the associated standard deviations in the regression models in Fig. 7.

It can be seen, that the response in the likelihoods show a high likelihood of the parameters in red for a characteristic curved shape with its peak at the expected ground truth parameters $\boldsymbol{x}_{\text{gt}} = \left[\nu = 0.3,\ E = 400\,\text{Pa}\right]^{\mathsf{T}}$. A high likelihood corresponds to a high probability density of the parameter combination to represent the reference data. This means that the corresponding values for $\boldsymbol{x}$ in this region of the input space result in simulation outputs that are very close to the observation data under the employed discrepancy measure. The likelihood falls very close to zero when moving away from the high likelihood regions, representing low similarity of the forward model result compared to the refer-

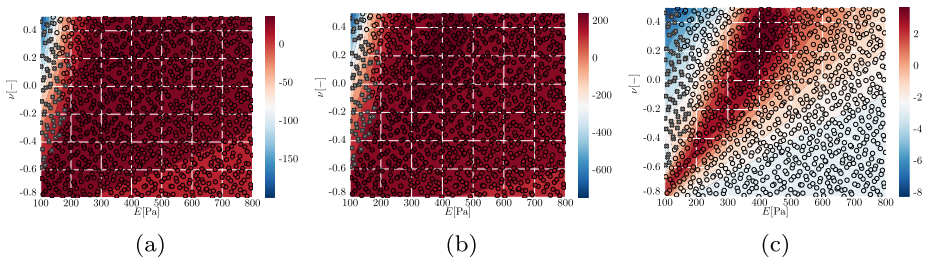

Fig. 6 Logarithmic likelihood regression model for different surface measure distances with $n_{\text{train}} = 1000$. **a** Euclidean distance at measurement points, **b** closest point projection distances, **c** RKHS norm. Training samples as circles for successful and gray crosses for failed forward model evaluations

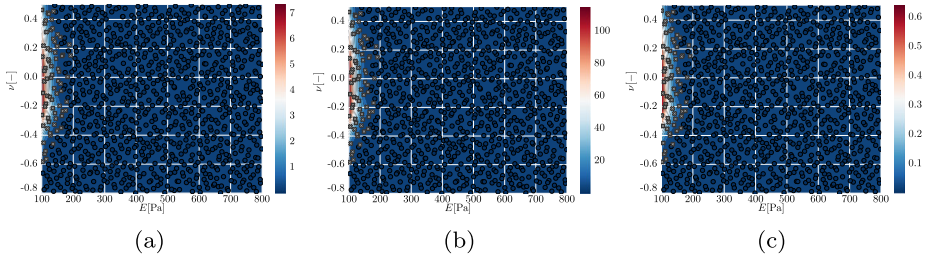

Fig. 7 Standard deviation from logarithmic likelihood regression model variance for different surface measure distances with $n_{\text{train}} = 1000$. **a** Euclidean distance at measurement points, **b** closest point projection distances, **c** RKHS norm. Training samples as circles for successful and gray crosses for failed forward model evaluations

ence data. Especially the failed simulations (gray crosses) fall in a region with very low likelihood values which renders them irrelevant for our investigations. For the rest of the input space, it can be seen in Fig. 7 that the standard deviation in the regression model is low and only rises in regions with little data.

Comparing the Euclidean distance measure in Fig. 5a and the closest point projection in Fig. 5b it can be seen, that the second one is more peaked around the maximum of the likelihood that is close to the ground truth value $\boldsymbol{x}_{\text{gt}}$. This is also a consequence of the formulation (4) and (5), as the numbers of distance measurements differ greatly with the number of measurement points $n_{\text{mp}} = 10$ and the number of interface nodes $n_{\text{in}} = 66$. The higher number of individual single point measurements generally leads to a more peaked likelihood with the same σ_{N}. It must also be stated that no further weighting of the closest point projection distances was done, so all nodal closest point projection distances are considered equally important. This includes the distances for many mesh nodes, that are close to the boundary conditions and therefore there the displacement magnitude is lower. An additional data compression approach, e.g., kernel principal component analysis [21,52] or also a selection of only a subset of the interface nodes could be used to increase comparability, but this is outside of the scope of the current article. The likelihood from the RKHS based distance measure (in Fig. 5c) combines both features to be expressive around the maximum likelihood (ML) point and still have information from more distant points. The RKHS norm measure correlates all discretized interface locations and orientations of the model to all counterparts in the observation (see (11)), therefore it is also expected to be the most detailed measure for this comparison.

The likelihood based on the forward model evaluations adequately combined with prior distributions results in the posterior (see (1)), which is a probability density of the param-

eters leading to the observations. It is favorable to have an expressive posterior and therefore expressive likelihood as a result to be able to compare posterior values for different parameter combinations and with that develop an understanding of the forward model in relation to the observations. In the case of a very flat likelihood the conclusion is that all parameter combinations are similarly well suited to explain the observations and therefore they are potentially insignificant to the forward model, at least in the range of the regarded parameter intervals. This means that all input parameters $\boldsymbol{x}$ will lead to forward model results that are very close to the observation under the employed discrepancy measure. The expressive shape of the likelihood based on the RKHS based measure underlines that this measure is well suitable in the given example to be used for Bayesian calibration. Therefore it is used in all following examples.

The presented likelihoods were generated using the different discrepancy measures (6), (7) and (11) and all yield similar characteristics in the shape of the likelihood. Therefore it can be concluded that in this setting and a fluid-biofilm interface-based measurement of a flow cell experiment an underestimation of Young's modulus E is coupled to an underestimation of Poisson's ratio ν. In applications with real experimental data, it would make sense to restrict the training points to the intervals, that are believed to contain the optimum or at least relevant values for the parameters. That could mean to restrict the Poisson's ratio to positive values, as this is what would be expected for most materials. Nevertheless, the resulting shapes representing high likelihood are very smooth for the whole tested range between ν =-0.8 and $\nu = 0.5$ and do not show a distinct border between positive and negative values. This is interesting with regard to biofilm mechanics in flow cell experiments as it shows that the estimation of E and ν is coupled for all surface comparisons that were tested. For some investigations, this also hints toward the need to incorporate additional measurements or information, e.g., prior knowledge.

Convergence over number of training points

The most costly part of the presented algorithm are the forward model evaluations that are necessary to generate the training data $\mathcal{D}$ of the GP log-likelihood regression model. While the convergence of the GP over the number of training data points is dependent on the character of the underlying function as well as on the selected design of experiments, we want to show a short qualitative convergence study for the problem at hand for the distance measure based on the RKHS inner product. In general the convergence study of a GP w.r.t. the number of training points is difficult as usually it is not feasible to increase the data point set size by orders of magnitude. Therefore other strategies, e.g., leave-one-out cross validation can be used as a proxy for the regression error [39]. The requirement towards the number of training points and the regression model is to catch the relevant shape characteristics of the likelihood.

For the application of such an approach, it is crucial to know how many forward model evaluations are required to get results efficiently. To get a first picture the Gaussian process regression model for the logarithmic likelihood is created for a series of training point set sizes n_{train}. For this qualitative study, only the RKHS norm based likelihood was used as it uses the most detailed comparison and seems to give the most expressive shape of the posterior. The likelihood parameters were set to $\sigma_{\text{W}} = 0.005\,\mu\text{m}$, $\sigma_{\text{N}}^2 = 0.0005\,\text{mm}^2$ in all following examples. The choice $\sigma_{\text{N}}^2 = 0.0005\,\text{mm}^2$ in our case relates to the discretization

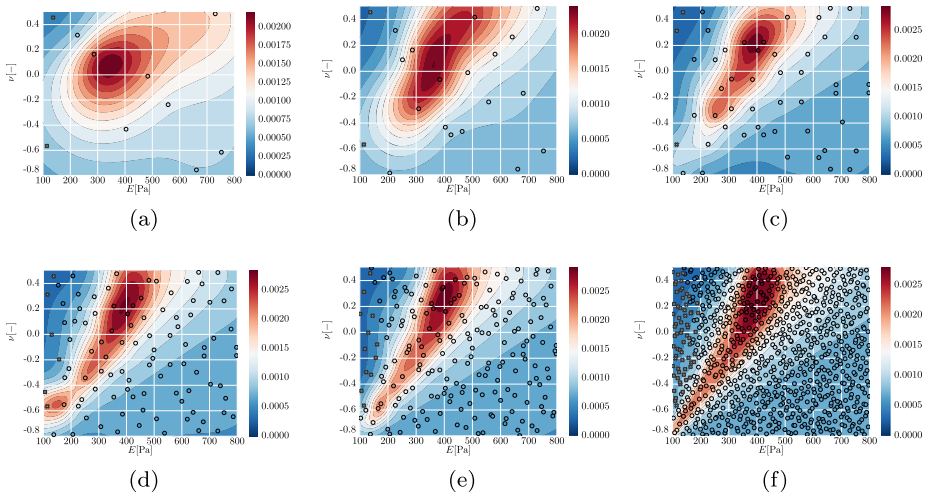

Fig. 8 Convergence of the Gaussian process regression model for the likelihood function over number of training points n_{train} (forward model evaluations). **a** $n_{\text{train}} = 10$, **b** $n_{\text{train}} = 20$, **c** $n_{\text{train}} = 50$, **d** $n_{\text{train}} = 100$, **e** $n_{\text{train}} = 200$, **f** $n_{\text{train}} = 900$. In all cases the same Sobol sequence was used to generate a space-filling training data set. Training samples as circles for successful and gray crosses (left side) for failed forward model evaluations

size, as the rounded squared average interface element length is $\bar{l}^2 \approx 0.0005\,\text{mm}^2$. It is difficult to interpret σ_{N} in relation to the measurement error alone, as especially also the image segmentation approach chosen to determine the model fluid–biofilm interface from experimental data influences the choice. We deviated from this parameter choice for σ_{N} in the comparison of the measures to keep it the same for all measures.

We used a Matérn 2/3 kernel (see appendix on GP, Eq. (27)) with one length scale hyperparameter l (in the standardized input space) and one signal variance σ_0^2 which will be determined via ML estimation using an L-BFGS-B optimizer for the evidence of the GP (see Eq. (29)). The Matèrn 2/3 kernel appeared to be the best suitable to represent the likelihood field as it resulted for the given example. Especially the great variety in steepness and therefore low smoothness of the likelihood seems to be the challenge for the regression approach. However, at the moment, no general recommendation for the GP kernel can be given. As commonly done [39] we used a fixed nugget noise $\sigma_{\text{n}}^2 = 10^{-5} \cdot (\max(\mathfrak{L}_{\text{train}}) - \min(\mathfrak{L}_{\text{train}}))$ to stabilize the training of the GP.

In the following, the convergence of the likelihood surrogate model over the number of used training points is qualitatively shown for the problem at hand. For this study, the Sobol sequence sampling property is used as all samples are consecutive samples from the same Sobol sequence. In Fig. 8 it is apparent, that only very few training points are necessary to estimate the general shape of the likelihood distribution and have a rough estimate for the optimum. With $n_{\text{train}} = 200$ samples the ML estimate is already in good agreement with the ground truth $\boldsymbol{x}_{\text{gt}} = \left[\nu = 0.3,\ E = 400\,\text{Pa}\right]^{\mathsf{T}}$.

It can be concluded that for this two-dimensional example the likelihood surrogate shows relevant features and the global shape well for $n_{\text{train}} = 200$ forward model evaluations and no significant gain in accuracy can be expected for a moderate increase of the sample size. Given that in the following examples a comparison with different priors is made and another problem dimension in form of an uncertain parameter is added, and therefore the complexity is increased, we use the Gaussian process model with one length

scale for all (standardized) parameters, a fixed nugget noise and $n_{\text{train}} = 1000$ training points for the following examples (see Remark 6 on dimensionality).

Remark 7 (Distribution of training points) With the applied approach of a grid-based quasi-random distribution of the samples, there is no compromise between exploration and exploitation, but the emphasis is put on exploration. It is possible to use available prior information for the generation of the samples and therefore have higher density of samples in high prior areas, or use an iterative approach and refine the samples in high posterior regions.

Calibration of constitutive parameters in biofilm models

In this subsection, the regression model will be generated according to the findings in the previous examples. The GP was constructed with a Matérn 2/3 kernel, a single length scale and signal variance for all parameters and a fixed nugget noise variance σ_{n}^2 in (29). 1000 samples were used for the training of the GP. As the likelihood model is available in form of a cheap to evaluate surrogate, we use 5000 SMC particles and 20 rejuvenation steps per SMC iteration (which would result in 1 million likelihood calls for 10 SMC iterations). For the adaptive step size of the SMC iterator a control parameter of $\zeta = 0.995$ was used (see Algorithm 1).

In the following examples, we examine the influence of priors in the parameters and uncertainties on the resulting posteriors. In Fig. 9 all results discussed in this section are plotted on the same page for better comparability. The different cases will be described and discussed subsequently in the following paragraphs. Figure 9 displays the resulting posteriors of the examples in form of SMC particle approximations. To visualize the character of the data, one particle distribution is shown explicitly in Fig. 9b, where the particles are plotted at their respective coordinates. The particle weights are illustrated as circle size and in a color scale. The other three subplots (Fig. 9a, c, d) show two-dimensional hexagonal histograms in a color scale. The particles are sorted into the displayed bins and summed up using their weights. The percentiles of the two-dimensional posteriors are additionally simplified as kernel density estimates (KDE) that are shown as black solid lines. For the KDE a radial basis function (RBF) kernel with bandwidth optimization was used.

On the top and right sides, the marginal distributions depending on both individual input parameters are plotted as histograms. The one-dimensional marginal posterior distributions $p\left(E|Y_{\text{obs},C}\right)$ and $p\left(\nu|Y_{\text{obs},C}\right)$ can easily be approximated by sorting the weighted particles into bins in the respective dimension. The marginals are additionally displayed in form of KDEs as black solid lines. The used priors are indicated as red dashed lines in all following plots.

Characteristic points deduced from the particle approximation are marked as crosses. The maximum a posteriori (MAP) estimate $\boldsymbol{x}_{\text{MAP}}$ is marked in green and the posterior mean (PM) $\boldsymbol{x}_{\text{PM}}$ in orange.

In high dimensions, the posterior cannot be plotted as easily as in the two-dimensional case. The analyst wants to have a comparative overview of where the mean value of the posterior is and how the probability mass is distributed in the posterior. For that and as another common approximation, we also show percentile lines of the global Gaussian approximation to the posterior in orange. The global Gaussian approximation is parame-

terized by the posterior mean (PM) vector $\boldsymbol{x}_{\mathrm{PM}}$ and the covariance matrix which can both be calculated from the weighted SMC particles very quickly.

We also present the Laplace approximation [21] of the posterior distribution around the MAP estimate depicted in Fig. 9a and c with green solid lines for the two cases without uncertainty. The Laplace approximation can be understood as a local quadratic approximation of the posterior density function around its MAP in the log space in form of a Gaussian distribution. The covariance matrix of the resulting local Gaussian distribution gives an idea of how fast the posterior changes in a certain direction, starting from the MAP estimate. Please note, that the posterior distribution is not known in closed form but only approximated by SMC particles with associated weight. We approximate the MAP estimate by the SMC particle that scored the highest posterior value in the last rejuvenation step of the last iteration. In these examples, the necessary gradients of the posterior distribution were approximated by finite differences w.r.t. the input variables $\boldsymbol{x}$ on the GP regression model. The Laplace approximation was omitted for the case with uncertain inflow. Laplace approximations are used for approximative Bayesian inverse analysis methods [6], where the MAP is first found through optimization and then the Lagrange approximation is computed for an estimate of the variance.

Influence of prior assumptions on the posterior distribution

To show the influence of quantifiable prior knowledge on the posterior, we discuss the same example with uniform prior and a combined beta-distribution and log-normal distribution prior on the model input $\boldsymbol{x}$.

Uniform prior In this first demonstration we choose an uninformative uniform prior distribution for Young's modulus $p(E) = \mathcal{U}(E|100\,\mathrm{Pa}, 800\,\mathrm{Pa})$ and for the Poisson ratio $p(\nu) = \mathcal{U}(\nu|-0.8, 0.5)$. Those are independent priors on the parameters and can be combined to $p(E, \nu) = p(E)\,p(\nu)$.

Figure 9a displays the approximation of the resulting posterior in form of a hexagonal histogram plot generated with the weighted particles from the SMC run. In Fig. 9b the resulting particle distribution of the SMC along with the colored-coded particle weight is shown.

The posterior in Fig. 9a shows an almost linear band shape of high densities. This shows that it is more crucial to have a good value for Young's modulus E than one for Poisson's ratio ν to obtain good similarity between model output and reference data for the given parameter ranges. The posterior mean (PM) vector computes to $\boldsymbol{x}_{\mathrm{PM}} = [E \approx 431\,\mathrm{Pa},\ \nu \approx -0.0071]^{\mathsf{T}}$. In Fig. 9a the Gaussian approximation has the same orientation as the particle approximation to the posterior. Still it can not represent the posterior complexity. The maximum a posteriori (MAP) is approximated to $\boldsymbol{x}_{\mathrm{MAP}} = [E \approx 388\,\mathrm{Pa},\ \nu \approx 0.266]^{\mathsf{T}}$. This $\boldsymbol{x}_{\mathrm{MAP}}$ is close to the ground truth in relation to the number of training points and the resulting resolution of training points in the input space.

Interestingly, the Laplace approximation, represented by its percentile contour lines in Fig. 9a in green, is almost oriented orthogonal to the actual posterior (solid black line). This means, that the Laplace approximation gives a misleading local approximation in this specific case. That can occur if the posterior has a more complex curvature around the MAP. In our example, this might be partially induced by the GP approximation, as well. It seems that the Laplace approximation cannot live up to the complexity of the given

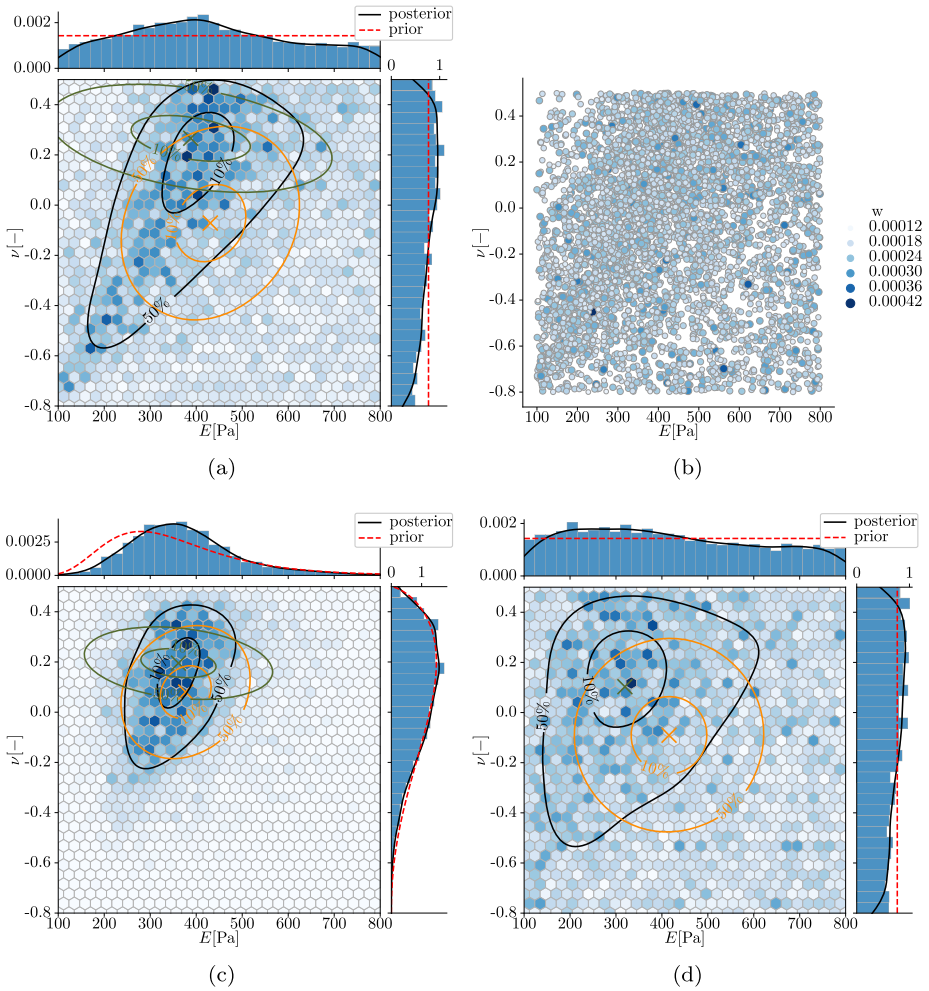

Fig. 9 Representation of the posterior distribution $p\left(E, \nu|Y_{\text{obs},C}\right)$ in histograms. Two-dimensional hexagon histograms for combined posterior and according marginals $p\left(E|Y_{\text{obs},C}\right)$ and $p\left(\nu|Y_{\text{obs},C}\right)$ attached to top and sides. Percentiles of kernel density estimates depicted as black solid lines, global Gaussian approximations as orange solid lines around the posterior mean ($\boldsymbol{x}_{\text{PM}}$ as orange cross) and the Laplace approximations as a green solid lines around the MAP estimate ($\boldsymbol{x}_{\text{MAP}}$ as green cross). **a** Posterior with uniform prior and **b** resulting particle and weight distribution from SMC. **c** Posterior with informed priors. **d** Posterior with uniform prior and uncertain inflow

posterior and therefore simplified methods based on the Laplace approximation would work poorly in presented examples without the analyst knowing. This is why we advocate the fully Bayesian treatment for this kind of problems.

As mentioned before, we also plot the marginal posterior distributions of $p\left(E|Y_{\text{obs},C}\right)$ and $p\left(\nu|Y_{\text{obs},C}\right)$, respectively. The marginals show that $p\left(E|Y_{\text{obs},C}\right)$ has a single, stable, global optimum and $p\left(\nu|Y_{\text{obs},C}\right)$ forms a plateau of high densities. Due to the strong coupling of E and ν and the complex shape of the joint posterior $p\left(E, \nu|Y_{\text{obs},C}\right)$, the marginal posterior distributions alone however are not informative for the coupling effects in the global posterior distribution.

Informed prior Physical insight can be incorporated in prior assumptions and can have a great influence on the posterior distribution and should be integrated in the analysis. Besides the uninformative uniform prior that we used in the first example, we now also

want to demonstrate the effect of an informed prior. For the Young's modulus, a log-normal prior is assumed with a mode of $E = 300$ Pa. The log-normal can be parameterized with $\mathcal{LN}(E|\mu_{\mathcal{LN}} \approx 5.86, \sigma_{\mathcal{LN}} = 0.4)$ with parameters $\mu_{\mathcal{LN}}, \sigma_{\mathcal{LN}}$ that are not standard deviation and mean of the distribution, but $\log(E) \sim \mathcal{N}\left(\mu_{\mathcal{LN}}, \sigma^2_{\mathcal{LN}}\right)$. This accounts for the fact that the Young's modulus must have positive values and it is very unlikely that it is close to zero but more probable to find values higher than the mode. For the Poisson's ratio a beta-distribution $\mathcal{B}(\nu|a = 43/13, b = 22/13)$ between -0.8 and 0.5 is used as prior. This distribution has its mode at $\nu = 0.2$ and accounts for the belief that the Poisson's ratio is more probable to have positive values and is strongly bounded between -1.0 and 0.5 with a decreasing probability towards the boundaries of this interval.

The modes of the presented priors are intentionally chosen to deviate from the ground truth $\boldsymbol{x}_{\text{gt}}$ to show the effect of informative priors. The priors are plotted in Fig. 9c alongside the respective marginal posterior distributions. It can be easily observed that compared to the uniform priors used in Fig. 9a, the informed prior assumptions, i.e., distributions that weight specific areas in the input space higher than others, lead to a posterior distribution which is more pronounced around the ground truth $\boldsymbol{x}_{\text{gt}}$ and has less probability mass in regions with low prior density. As the majority of the probability mass of the resulting posterior is now in a more compact area of the design space, also the marginal posterior distributions $p\left(E|Y_{\text{obs},C}\right)$ and $p\left(\nu|Y_{\text{obs},C}\right)$ show a more defined shape with one predominant mode.

Similar to Fig. 9a, the joint posterior $p\left(E, \nu|Y_{\text{obs},C}\right)$ has more variance in the ν-dimension, rendering ν a *sloppy* parameter. This becomes also apparent as the marginal posterior distribution $p\left(\nu|Y_{\text{obs},C}\right)$ almost coincides with the prior assumption $p(\nu)$, indicating a very small influence of this parameter on the likelihood function. This also means that for this type of measurement the exact value of model parameter ν has less importance for the agreement of mechanical model and observed experiment. In $p\left(E|Y_{\text{obs},C}\right)$ on the other hand the density does not have the same mode as the prior $p(E)$. This underlines that the likelihood contains characteristic information about this parameter.

The MAP estimate has the values $\boldsymbol{x}_{\text{MAP}} = [E \approx 361\,\text{Pa},\ \nu \approx 0.195]^{\mathsf{T}}$ in this case. This is slightly lower in both parameter values than in the run with uniform prior. With the prior modes deviating from the ground truth, a deviation of $\boldsymbol{x}_{\text{MAP}}$ from the ground truth towards lower values is expected. Furthermore, we see that the global Gaussian approximation of the posterior around $\boldsymbol{x}_{\text{PM}} = [E \approx 377\,\text{Pa},\ \nu \approx 0.08]^{\mathsf{T}}$ moves closer to the mode of the posterior distribution, as the low likelihood areas are further weighted with low prior values and therefore lose probability mass compared to the uniform priors. The Laplace approximation is still not a very good local approximation of the posterior.

Material calibration under uncertain boundary conditions

Now we also demonstrate the treatment of additional uncertain influences on the system, denoted as θ above. We use the example of an uncertain inflow volume rate in the flow cell experiment. As generally the biggest biofilm patches in the channel are analyzed, they take up a significant portion of the cross-section of the channel and force the flow to go around it. Further, only the middle of the channel can be scanned to high quality using OCT. Hence, the distribution of the volume flow rate between outlying parts of the cross-section and the analyzed patch is subject to uncertainties. Overall these considerations

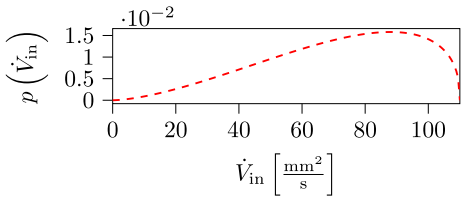

Fig. 10 Assumed beta-distribution $p\left(\dot{V}_{\text{in}}\right)$ of assumed uncertain inflow volume rate $\dot{V}_{\text{in}}$

are summed into the assumption of an uncertain inflow rate distribution, that has its main mode significantly lower than the average inflow rate and a spread distribution around that, with low density for higher flow rates. This is modeled with an assumption of $p\left(\dot{V}_{\text{in}}\right)$ as a beta-distribution $\mathcal{B}\left(\dot{V}_{\text{in}}|a = 2.6, b = 1.4\right)$ between $0\,\text{mm}^2/\text{s}$ and $110\,\text{mm}^2/\text{s}$ with mode at $88\,\text{mm}^2/\text{s}$ which is plotted in Fig. 10. The value of the volume inflow rate used for data generation is kept the same as in all other examples $\dot{V}_{\text{in}} = 100\,\text{mm}^2/\text{s}$. The distribution accounts for the belief that only less than average of the fluid volume rate flows over the biofilm as compared to the rest of the channel. For the two material parameters uniform priors $p\left(E\right) = \mathcal{U}\left(E|100\,\text{Pa}, 800\,\text{Pa}\right)$ and $p\left(\nu\right) = \mathcal{U}\left(\nu| -0.8, 0.5\right)$ were used.

The resulting joint posterior of the two analyzed parameters under the influence of the uncertain inflow are plotted in Fig. 9d. The posterior under uncertainty, denoted by $q(E, \nu|Y_{\text{obs},C}) = \mathbb{E}_{\dot{V}_{\text{in}}}\left[p\left(E, \nu|\dot{V}_{\text{in}}, Y_{\text{obs},C}\right)\right]$, was then calculated according to (3b) by incorporating the average effect of the uncertainty of the inflow $\dot{V}_{\text{in}} \sim p\left(\dot{V}_{\text{in}}\right)$. In Fig. 9d it can be seen that, as it should be expected, the additional consideration of uncertainty of the inflow made the posterior less expressive, such that an increase in the variance can be especially found along the dimension of the Young's modulus.

The consideration of an uncertain boundary condition has also moved the point estimates. The MAP estimate for both inputs $\boldsymbol{x}$ moves to lower values of $\boldsymbol{x}_{\text{MAP}} = [E \approx 322\,\text{Pa},\ \nu \approx 0.09]^{\mathsf{T}}$ than in the uniform prior example without uncertainties. The posterior mean is $\boldsymbol{x}_{\text{PM}} = [E \approx 416\,\text{Pa},\ \nu \approx -0.09]^{\mathsf{T}}$. This is expected as the mean of the assumed inflow distribution is lower than the value used for data generation and therefore lower stiffness leads to a better suiting deformation.

Remark 8 (MAP estimation after marginalization) With the consideration of uncertain parameter $\boldsymbol{\theta}(= \dot{V}_{\text{in}})$ the MAP estimate is more difficult to obtain than without uncertainties. MAP determination is more difficult because the extended posterior (3b) must first be integrated to the posterior under uncertainty. Although this integration can easily be evaluated using the particle representation (13), the maximum of the posterior under uncertainty cannot be found without another assumption. We chose a histogram approach to collect the SMC particles in squared bins with 30 intervals per input variable $\boldsymbol{x}$ according to the illustration in Fig. 9d. The trick of picking the particle that scored the highest posterior in the last SMC iteration does not work for the posterior under uncertainty or marginal distributions, as their determination first needs an integration step.

The global Gaussian approximation is more isotrop when considering the uncertainty. This is represented as a Gaussian approximation that has more circular percentile lines. In the interpretation of the covariance of the posterior, this means that there is no prevalent

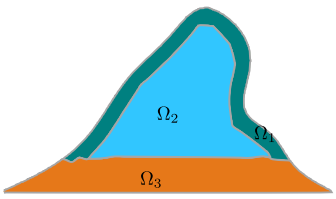

Fig. 11 Subdomains for heterogeneous biofilm model

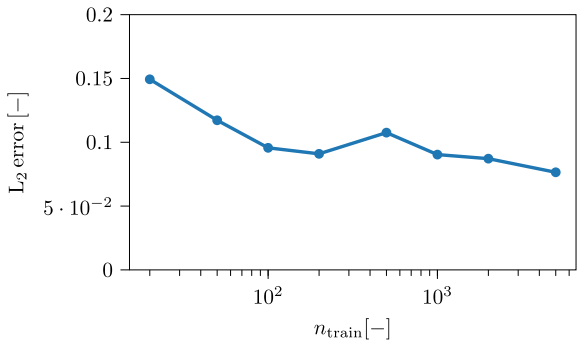

Fig. 12 Error for GP regression model with $n_{\text{test}} = 100$ test points over number of training data points n_{train}

direction in this posterior. Compared to the posterior for the fixed boundary condition, the posterior including the uncertainty $q(E, \nu | Y_{\text{obs},C}) = \mathbb{E}_{\dot{V}_{\text{in}}}\left[p\left(E, \nu | \dot{V}_{\text{in}}, Y_{\text{obs},C}\right)\right]$ is less restrictive by means of necessary assumptions and therefore also less stiff in the results. This gives also more flexibility in the results as there is a broader range of parameters to explain the observed experimental results. Nevertheless, better knowledge about uncertainties $p\left(\dot{V}_{\text{in}}\right)$ can greatly improve the calibration result.

In case non-controllable *aleatory* uncertainty is present, neglecting it will lead to an overconfident, wrong posterior as the analyst introduces a modeling error by neglecting these effects. Incorporating aleatory uncertainty in the probabilistic model will generally introduce more uncertainty to the posterior (the distribution widens) and might potentially even completely change the characteristics of the posterior distribution.

Calibration of heterogeneous biofilm model under uncertain inflow boundary condition

In our last example we want to calibrate material properties of a heterogeneous biofilm FSI model as in [12], but here under an uncertain inflow rate boundary condition. Heterogeneity comes into play in such problems due to different age and/or different nutrient availability of different parts of the domain. Hence, it was a natural choice to also shed some light on a more demanding case involving more parameters. The three subdomains are depicted in Fig. 11 and lead to six input parameters, consisting of the Young's modulus and Poisson's ratio of each subdomain.

The parameters $\boldsymbol{x}_{\text{gt}} = [E_1 = 500\,\text{Pa},\ \nu_1 = 0.2,\ E_2 = 200\,\text{Pa},\ \nu_2 = 0.1,\ E_3 = 1000\,\text{Pa},\ \nu_3 = 0.3]^{\intercal}$ for a hyperelastic Saint-Venant-Kirchhoff material model are used as the ground truth inputs, along with the inflow rate $\dot{V}_{\text{in}} = 100\,\text{mm}^2/\text{s}$. All other model details are the same as for the previous examples, to then generate the synthetic experimental data $Y_{\text{obs},C}$ for this heterogeneous case. Please note that in this example we addi-

tionally assume noise polluted measurement data according to

$$\begin{aligned} &Y_{\text{obs},C} = \mathfrak{M}\left(\boldsymbol{x}_{\text{gt}}, \boldsymbol{\theta}_{\text{gt}}, C\right) + \sigma_{\text{n,obs}} \cdot \boldsymbol{\epsilon} \\ &\text{with } \boldsymbol{\epsilon} \sim \mathcal{N}\left(\mathbf{0}, I\right) \end{aligned} \tag{16}$$

For the following example we choose noise with a standard deviation of $\sigma_{\text{n,obs}} = 1\,\mu\text{m}$. In remark 9 we comment on the determination of the GP surrogate for this example.

Remark 9 (Convergence of the Gaussian process surrogate) As the GP surrogate model for the likelihood is now dependent on six input variables plus one uncertain variable, more training data is necessary to reach acceptable accuracy of the posterior mean function of the GP. A small convergence study was performed to find an appropriate training size. Therefore we successively increased n_{train} according to the Sobol sequence and then calculated the L_2-error norm between the posterior mean of the GP and the likelihood evaluated with the forward model at $n_{\text{test}} = 100$ testing points that are fixed consecutive samples from later in the Sobol sequence and unused in the training data. This is a representative choice as the good space filling property leads to test points which are well distributed. The result of the convergence study is plotted in Fig. 12. The tested scenario is a kernel with multiple length scales with a multiplicative coupling [39,53] as used in the following example. The parameters are expected and also observed to have different influence on the likelihood. Therefore different length scales and variances in a multiplicative coupling of Matérn 2/3 kernels for each parameter dimension is used. As opposed to the L-BFGS-B optimizer used in previous examples, a scaled conjugate gradient optimizer is used for training for stability reasons.

Figure 12 shows that between $n_{\text{train}} = 1000$ and $n_{\text{train}} = 5000$ no significant improvement in the given error measure can be achieved. That is why the evaluation with $n_{\text{train}} = 2000$ data points is chosen for the following example as a compromise between efficiency and accuracy. In general asymptotic convergence can be expected, meaning that the error measure will go to zero for an infinite amount of training points. For $n_{\text{train}} = 500$ an increase in the error can be detected. Here a new characteristic in the likelihood function was introduced with the training points between $n_{\text{train}} = 200$ and $n_{\text{train}} = 500$, that lead to the increased deviation at the test points.

For the SMC approach a set of 10,000 particles with 30 rejuvenation steps was used with a step size control parameter of $\zeta = 0.998$. Just as a comparison to the $n_{\text{train}} = 2000$ training points used, a full evaluation in every rejuvenation step of the SMC algorithm would require three million ($10,000 \cdot 30 \cdot 10 = 3,000,000$) forward model evaluations for exemplary 10 SMC steps. This is neither desirable nor feasible if directly applied to the expensive forward model. After the proof of concept in previous examples, with two input parameters and potentially one uncertain parameter, it must be emphasized, that volume integrals for respective marginals and especially the normalization of the posterior (1) in six plus one dimensions scale even worse. Just for a moderately sized, grid-based discretization with 100 sample points in every dimension we would get 100^7 necessary evaluations of the GP-mean. So we make use of the good scalability of the SMC algorithm in higher dimensions in the following examples.

As already indicated above, in this last example we want to show the full capability of the approach and therefore we use an example with uncertain inflow rate $\dot{V}_{\text{in}}$ and added noise to the data generated from the ground truth values. The assumed distribution on $\dot{V}_{\text{in}}$

is the same as in Fig. 10 above with a beta-distribution $\mathcal{B}\left(\dot{V}_{\text{in}}|a = 2.6, b = 1.4\right)$ between $0\,\text{mm}^2/\text{s}$ and $110\,\text{mm}^2/\text{s}$ with its mode at $88\,\text{mm}^2/\text{s}$. The MAP approximation is found at $\boldsymbol{x}_{\text{MAP}} = [E_1 \approx 345\,\text{Pa},\ \nu_1 \approx 0.43,\ E_2 \approx 135\,\text{Pa},\ \nu_2 \approx 0.30,\ E_3 \approx 1034\,\text{Pa},\ \nu_3 \approx -0.47]^{\text{T}}$ and the global posterior mean computes to $\boldsymbol{x}_{\text{PM}} = [E_1 \approx 443\,\text{Pa},\ \nu_1 \approx -0.15,\ E_2 \approx 431\,\text{Pa},\ \nu_2 \approx -0.13,\ E_3 \approx 637\,\text{Pa},\ \nu_3 \approx -0.14]^{\text{T}}$. Analogously to the lower dimensional example, the MAP estimate is obtained with a binning approach with 10 intervals in each input dimension. Therefore it is a rough estimate. Nevertheless, the curse of dimensionality inhibits an excessively fine grid. The maximum of the posterior under uncertainty qualitatively represents the ground truth with $E_3 > E_1 > E_2$ and $\nu_1 > \nu_2$. Only for ν_3, it does not correspond to the ground truth. This can be a consequence of the relevance of the parameter to the overall posterior, as the lateral contraction in the stiffest subdomain, attached to the ground also has little effect on the interface deformation. In challenging examples it can be a good idea to first perform a global sensitivity analysis [54,55] and then focus the inverse analysis only on the most sensitive parameters. It also shows again, that the problem setup is challenging as the volume inflow rate is used as an uncertain parameter. But this is also often the case in real-world applications. This has the effect that the MAP parameters are those of a less stiff biofilm material, than the ones used for the ground truth simulation.

The resulting one dimensional marginals over the parameters, for which uniform priors were assumed, are plotted in Fig. 13 as histograms with KDE approximations in black. Here the letter $q(\boldsymbol{x}|Y_{\text{obs},C})$ is used because the distributions represent marginals of the posterior under uncertainty (3b).

It can be observed that most of these marginals show a rather uniform distribution. In this example, this happens as they represent the integration of the posterior with respect to all other parameters respectively and therefore the probability mass is accumulated herein. Only for subdomain Ω_2 (in Fig. 13c and d) the posterior marginals acummulate density around the ground truth $E_2 \approx 200\,\text{Pa}$ and $\nu_2 > 0$. As these single-dimensional marginals are not unveiling the full complexity of the posterior, a further step is made to show two-dimensional marginals for a selected combination of parameters in Fig. 14 as hexagonal histograms with the percentile lines of the KDE approximations. Therein the interaction effects between the respective combination of parameters can be seen. Especially within the regions enclosed by the percentile lines of 10% the most probable parameter combinations for the respective marginals can be found.

The marginal posterior distributions in Fig. 14 show complex densities. As compared to a deterministic calibration approach for the same example [12], where even the less complex case with a fixed volume inflow rate $\dot{V}_{\text{in}}$ could not be solved, this complex character can be well represented here in the obtained solution. Furthermore, for Fig. 14a and c it can be seen that E_2 dominates the marginal posteriors that are high around $E_2 \approx 200\,\text{Pa}$ for a plausible range of the other Young's moduli E_1, E_3. Also the shape of the distribution for Ω_2 in Fig. 14e resembles the posterior shape in Fig. 9d, which is the one for homogeneous example with uniform prior and uncertain inflow. This means that parameters in Ω_2 qualitatively have similar influence in this marginal, as the two parameters have in the homogeneous example in the posterior. This is also expected as Ω_2 takes up the highest portion of the biofilm domain (see Fig. 11) and therefore dominates the deformation.

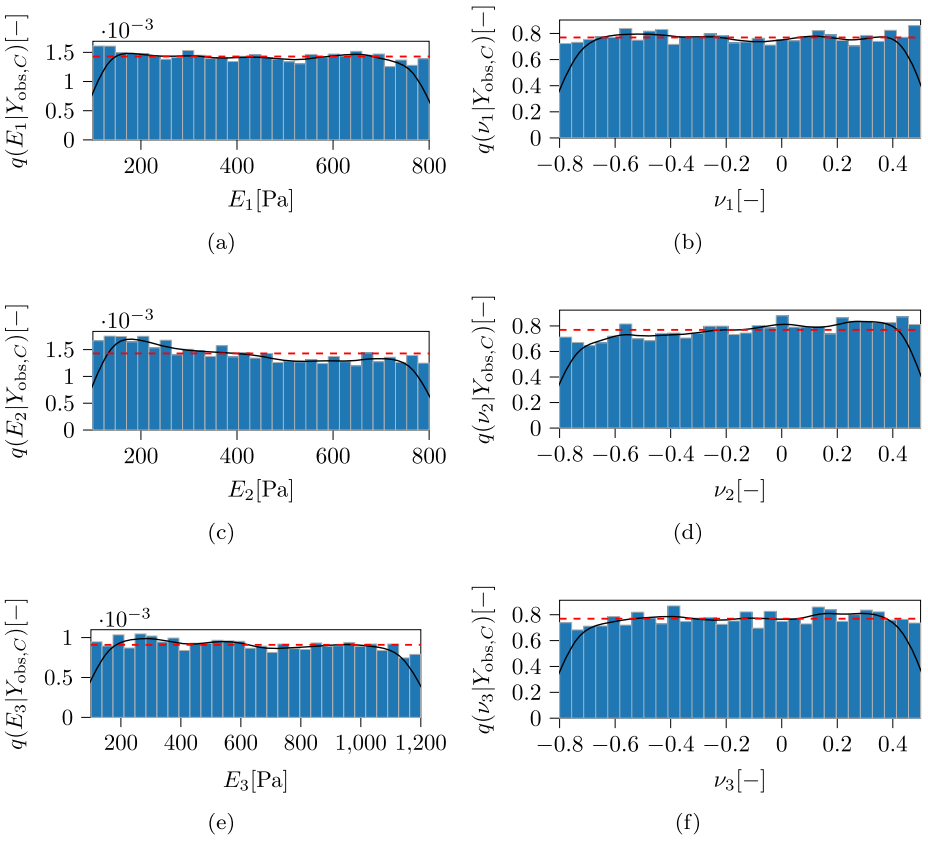

Fig. 13 Marginals of the posterior for **a**–**f** individual parameters in heterogeneous example with uncertain inflow condition with added Gaussian noise and uniform prior as red dashed line. Marginals as histograms (blue) with a KDE approximation (black)

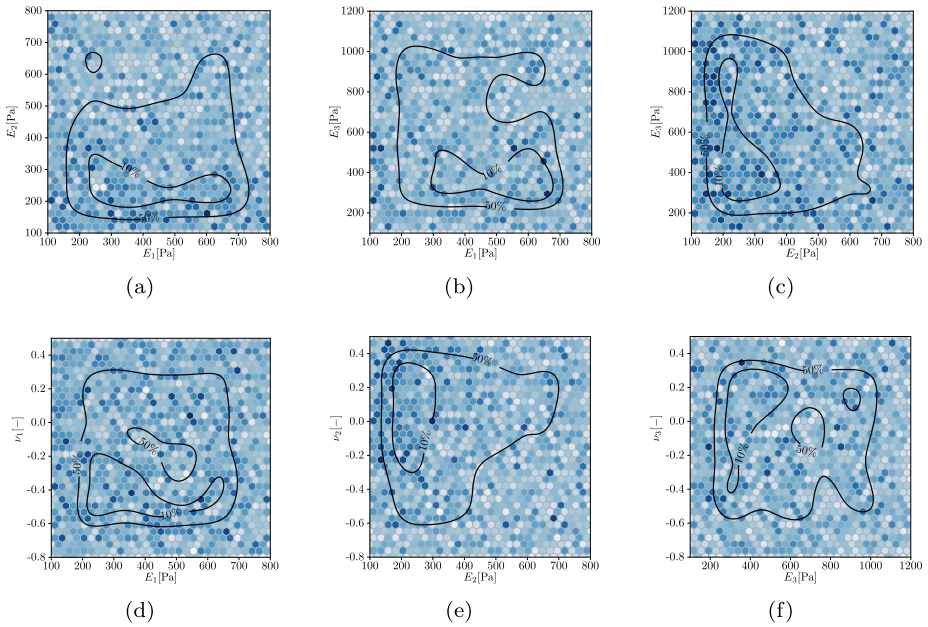

Fig. 14 Hexagonal histograms (high weight in dark blue) for marginals for selected pairs of parameters in heterogeneous example with uncertain inflow condition and added Gaussian noise. Percentile lines of KDE approximations in black

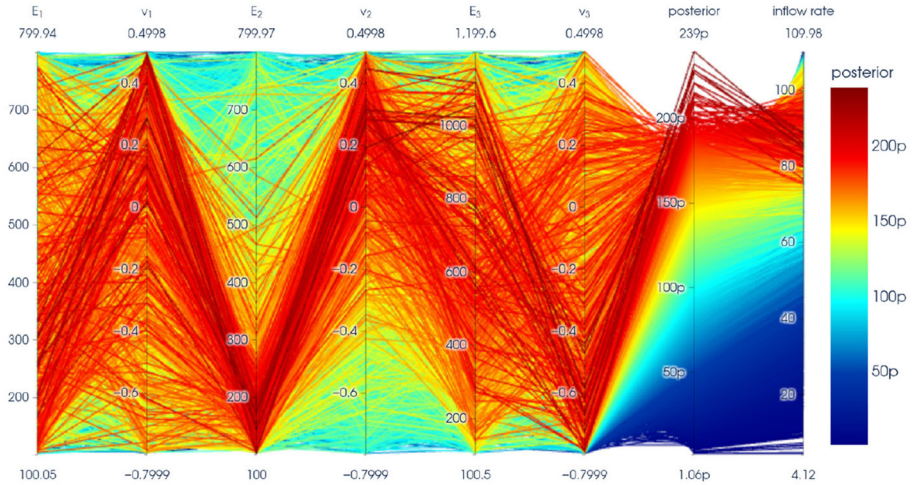

Fig. 15 Parallel axis plot over all parameters, posterior values $p\left(\boldsymbol{x}|\boldsymbol{\theta}, Y_{\text{obs},C}\right)$ and inflow rate for all particles of the SMC particle approximation of the posterior with uniform prior assumptions for $\boldsymbol{x}$

As we have six parameters involved, a full plot of the posterior is impossible. Alternatively, a parallel axis plot as in Fig. 15 can be used to get an idea of the underlying posterior shape.

Over the first six axis we see the input parameters for the range of interest. The seventh axis shows the extended posterior values for the 10,000 particles from the SMC particle approximation. The last axis represents the uncertain inflow boundary condition $\dot{V}_{\text{in}}$. Every line connecting the axis represents one particle of the SMC solution and all lines are colored by their absolute extended posterior density value. The lines are drawn on top of each other, starting with low posterior density values in blue and ending with the highest ones in red. Most of the parameter combinations with high posterior density accumulate around $E_2 \approx 200\,\text{Pa}$ and $\nu_1, \nu_2 > 0$. The other three parameters E_1, E_3, ν_3 seem to score relatively high posterior values for the whole range of interest. That means they are individually less significant to a specific value of the posterior density. Given the subdomain topology, as seen in Fig. 11, these posterior results can also be expected as Ω_2 takes up the largest portion of the biofilm and therefore can also be expected to have the highest influence on the deformation in this case.

The possibility for such a phenomenological interpretation of the posterior is a very attractive feature of tackling the inverse problem via the proposed approach, as not only good point estimates can be concluded, but more importantly the influence of the individual parameters on the posterior can be observed and interpreted. The information revealed in such a probablistic analysis, as for example displayed in Figs. 14 and 15, gives indeed a lot of insight into the problem at hand. Among others, it also shows how useful given experimental information is or whether other measurements are needed for the identification of relevant parameters. With the rich information from such an analysis also an estimation of the plausibility and stability of the point estimates can be made. As an example, a deterministic or trial and error approach might end up in identifying negative Poisson ratios for biofilms (easily understandable when looking at Figs. 9 or 15) and hence identifying biofilms as auxetic materials, as it has been done in the past. The probabilistic analysis would immediately show the lack of validity for such a conclusion.

Conclusion

We presented a robust and efficient Bayesian calibration approach for coupled computational mechanics models with given boundary or interface deformations. We considered the particularly challenging case, where only interface shapes based on images of the domain at different points in time or different experimental conditions are obtainable but no displacements of material points. Lacking such displacements, we also introduced and compared several metrics to calculate the discrepancy between interface shapes. We also considered the additional challenge to incorporate the influence of uncontrollable uncertainties in the experimental setup, such as uncertain boundary conditions

In contrast to deterministic optimization approaches for calibration tasks, Bayesian calibration is mathematically much more robust. This is because it is formulated in a probabilistic manner that describes the problem globally in form of a so-called posterior distribution. An optimization problem only results in one particular point estimate for the parameters instead. The latter is prone to get stuck in local optima which might not lead to satisfactory results.

The Bayesian calibration approach also allows for a more meaningful interpretation of the calibration result. The posterior density can be explored using a sequential Monte Carlo approach. This also allows for a convenient computation of the involved high-dimensional integrals or point estimates such as the maximum a posteriori (MAP) estimate. The posterior distribution gives rise to several further expressive point estimates, uncertainty and robustness measures, which help to get a deeper understanding of the parameters' effect on the solution.

We have observed, that already for very few parameters, approximations, e.g., based on point estimates as the MAP and the Laplace approximation, cannot live up to the complexity of the resulting posteriors. Therefore, a full approximation of the posterior appears to be a necessary approach to studied inverse problems. That allows to gain further insight into the relevance of the parameters and the interaction of parameters in the model. Thereby a better understanding of the computational forward model in relation to the observed results of an experiment can be obtained.

To control the computational cost of the approach we proposed to build a Gaussian process (GP) surrogate model on the log-likelihood. The computationally most expensive step in the presented approach is the generation of the training data for the construction of the GP surrogate. The required forward model evaluations can however be computed in parallel and their exact amount is open to the analyst's choice. By constructing the log-likelihood surrogate, the approach is robust against single failing forward model evaluations, as it can be built on the remaining successful runs.

We presented and tested three different types of discrepancy measures between interfaces when no comparison of displacements of material points is possible. At first, an Euclidean distance measure at selected measurement points at characteristic locations on the interface was used. It is expected to be the easiest measure to apply to real data, as no full representation of the deformed geometry is required. Second, we used closest point projection distances for all interface nodes from the finite element discretization as a comparative measure. Eventually, the RKHS norm measure led to the most expressive posterior and is in general appealing because of its solid mathematical foundation and flexibility. Nevertheless, all measures yielded suitable likelihood distributions. A proper

choice should be made based on the characteristics and quality of the experimental data. The choice of the distance measure is also dependent on the type of calibration task and on the question of which aspect of the deformation the analyst wants to emphasize.

For the demonstration of our calibration approach, we chose the material parameter identification of a spatially two-dimensional fluid–structure interaction (FSI) problem including a homogeneous hyperelastic solid biofilm model. We used artificial reference data such that we know the ground truth in order to be able to focus the attention on the characteristics of the proposed approach. We showed that the point estimates in the examples with two calibrated parameters were close to the ground truth $\boldsymbol{x}_{\mathrm{gt}}$ and the approximation of the full posterior allowed to observe the strong coupling between the input parameters in their influence on the posterior density. The posterior solution allowed us to observe the interaction of the two parameters in the model which in the present case was an almost linear relationship between E and ν for which high posterior densities occurred in this setting. We furthermore studied the influence of uncertain experimental conditions on the posterior density. Such uncertainty led to a slightly flatter and therefore less expressive posterior such that the variance of the posterior increased and the posterior density filled the design space more equally. Besides the expected increase in variance also the expectation and MAP estimate deviated. Compared to the previous case, where the additional uncertainty was neglected, this shows that it is important to consider existing uncertainties. Otherwise the posterior might be overconfident and might have entirely different characteristics.

As a further example, we investigated a more complex calibration problem of a heterogeneous biofilm model with six unknown material parameters under uncertainty that also included artificial measurement noise. In this challenging example, the MAP estimate deviates more from the ground truth because the problem has more degrees of freedom and additional uncertainty and noise. This example, that could not be solved at all for an easier setting without uncertainty with a deterministic approach in [12], could be solved and interpreted with the approach presented herein, hinting to higher robustness of the presented approach.

While the examples have been chosen from a particular field of application, the approach is general and can be applied to all sorts of single-field or coupled multi-field calibration problems with given boundary or interface deformations, where boundary deformations are available, but no point-to-point correspondence between simulation results and experimental observations can be found. This means that the presented approach can be used without limitations also for spatially three-dimensional models and more complex and expensive forward models.

In high parameter dimensions, other methods like variational Bayes approaches or multi-fidelity approaches such as [56] are promising alternatives.

Appendix

We present additional details for biofilm flow cell experiments, the continuum mechanics description of the FSI problem, further details of RKHS properties and a brief description of Gaussian processes in the appendix.

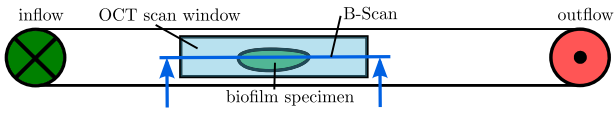

Fig. 16 Schematic setup of a flow cell experiment with biofilms for measurement with optical coherence tomography (OCT)

Flow cell experiments with biofilms and optical coherence tomography

This is a short introduction to flow cell experiments with biofilms. In a flow cell experiment, the biofilm is grown on the bottom of a channel with a flowing liquid that is providing nutrients to the microorganisms. The channel has dimensions like $50\,\text{mm} \times 5\,\text{mm} \times 0.45\,\text{mm}$ in recent experiments [15] or $124\,\text{mm} \times 2\,\text{mm} \times 1\,\text{mm}$ in previous experiments [14]. An exemplary flow cell channel is depicted in Fig. 16 in top–down view. To simplify the illustration only one single bigger patch of biofilm is drawn. After a pronounced patch of biofilm is identified in the channel, a deformation experiment is conducted with the specimen [14]. Such experiments are typical in biofilm research and hence we use them for parameter identification. Parameter identification is known to be very tricky for biofilms due to the soft consistency of the material and the necessity to keep the biofilm material in natural conditions. In an deformation experiment, mechanical load is applied onto the biofilm via the flowing liquid and then the deformation of the biofilm domain is measured.

To obtain accurate measurements of the biofilm boundary in undeformed reference configuration, the latter is first scanned using optical coherence tomography (OCT) without a significant fluid flow through the channel. Subsequently, a fluid flow is introduced into the channel at the inlet via a fluid pump, for which the volume flow rate can be controlled. We are not simply transferring this to defined load on the biofilm surface, e.g., constant shear stress, but take the full interaction between liquid and biofilm into account. This means that the resulting fluid forces acting at the immersed biofilm boundary deform the biofilm, which in return changes the surrounding fluid flow. This phenomenon is known as *fluid–structure interaction (FSI)* or in this specific case as *fluid–biofilm interaction (FBI)*.

The deformed biofilm is then again scanned via OCT. OCT can only be done in a *scan window* as sketched in Fig. 16. This is important information for our approach as it also contributes to the uncertainty of conditions. This is because upstream and downstream from the analyzed patch as well as in the attached tubes and inflow and outflow areas there will be "invisible" and unregistered biofilm patches. The resulting snapshots of the deformed and undeformed biofilm represent the data of the flow cell experiments. If required, the experiment and snapshots are repeated for different flow settings or multiple points in time. In the literature (e.g., [14,15,57]) one planar scan with OCT is labelled *B-scan* as it is a combination of one dimensional *A-scans* along the flow direction. By a combination of several *B-scans* to *C-scans* a three-dimensional volumetric representation of the biofilm is measured. This type of image data can then be used in the presented material parameter calibration approach.

Also due to the reduction of the whole channel to a planar view of a portion of the center of the channel, the fluid inflow boundary conditions in the planar consideration becomes prone to uncertainty. First, and as already mentioned, it is unknown if there are different

unregistered biofilm patches upstream or downstream of the regarded domain. Practically the inverse analysis and biofilm modeling will focus on the biggest biofilm patch in the channel. Second, if the biofilm patch does not occupy the full channel width uniformly, fluid flow will partly pass the biofilm and therefore the average fluid flow rate cannot be assumed to flow over the patch. These considerations lead to the assumption that the flow rate in the two-dimensional model is uncertain and this type of uncertainty must be quantifiable in our approach.

Fluid–solid interaction approach for modeling biofilm mechanics

In this work we model the previously described fluid–biofilm interaction of the flow cell experiments with biofilms as a coupled mechanical two-field problem. The experiments can result in significant deformations, displacements and rotations of the initial biofilm configuration, such that a nonlinear kinematic description of the biofilm displacement field is required. The strong form of the associated differential equations for the fluid–solid interaction are briefly summarized for the fluid domain, the solid domain and the coupling of the two. For the sake of compactness, the presentation is limited to the field equations. The respective boundary conditions are implicitly assumed to be well defined. The interested reader is referred to the literature (e.g. [58,59]) for a methodological discussion of fluid–solid interaction models and their numerical discretization with a monolithic arbitrary Lagrangian–Eulerian (ALE) approach.

Continuum description of the fluid field

The fluid field in the channel is well described by the incompressible Navier–Stokes equation for Newtonian fluids. We apply an arbitrary Lagrangian–Eulerian (ALE) description, which uses a moving fluid mesh and accounts for the resulting mesh displacements and velocities in the fluid domain, due to compatibility with the moving solid domain. The velocity of the fluid relative to the fluid mesh is then expressed by the ALE convective velocity $\boldsymbol{c}^{\mathrm{F}}$. The fluid equations in ALE formulation read as

$$\rho^{\mathrm{F}} \frac{\partial \boldsymbol{v}^{\mathrm{F}}}{\partial t} + \rho^{\mathrm{F}} (\boldsymbol{c}^{\mathrm{F}} \cdot \nabla) \boldsymbol{v}^{\mathrm{F}} - 2\mu^{\mathrm{F}} \nabla \cdot \boldsymbol{\epsilon}(\boldsymbol{v}^{\mathrm{F}}) + \nabla p^{\mathrm{F}} = \rho^{\mathrm{F}} \hat{\boldsymbol{b}}^{\mathrm{F}} \qquad \text{in } \Omega^{\mathrm{F}} \times (0, T) \tag{17a}$$

$$\nabla \cdot \boldsymbol{v}^{\mathrm{F}} = 0 \qquad \text{in } \Omega^{\mathrm{F}} \times (0, T). \tag{17b}$$

Wherein the variables of interest are the fluid velocity $\boldsymbol{v}^{\mathrm{F}}$, the fluid pressure p^{F}, the fluid density ρ^{F}, the fluid dynamic viscosity μ^{F} and the body force $\hat{\boldsymbol{b}}^{\mathrm{F}}$ in the fluid domain $\Omega^{\mathrm{F}} \times (0, T)$. The strain rate tensor $\boldsymbol{\epsilon}(\boldsymbol{v}^{\mathrm{F}})$ in (17) furthermore expands to the expression

$$\boldsymbol{\epsilon}(\boldsymbol{v}^{\mathrm{F}}) = \frac{1}{2} \left(\nabla \boldsymbol{v}^{\mathrm{F}} + \left(\nabla \boldsymbol{v}^{\mathrm{F}} \right)^{\mathrm{T}} \right). \tag{18}$$

Continuum description of the solid field

In this work, the biofilm is modeled as a nonlinear solid. In the solid domain, the continuum field is described by the nonlinear balance of momentum in reference configuration

$$\rho_0^{\mathrm{S}} \frac{\mathrm{d}^2 \boldsymbol{d}^{\mathrm{S}}}{\mathrm{d}t^2} = \nabla_0 \cdot (\boldsymbol{F} \cdot \boldsymbol{S}) + \rho_0^{\mathrm{S}} \hat{\boldsymbol{b}}_0^{\mathrm{S}} \quad \text{in } \Omega_0^{\mathrm{S}} \times (0, T). \tag{19}$$

Here, the solid displacements $\boldsymbol{d}^{\mathrm{S}}$ are used as primary variable. The other quantities are the deformation gradient $\boldsymbol{F}$, the second Piola-Kirchhoff stress tensor $\boldsymbol{S}$ and the body

force in reference configuration $\hat{\boldsymbol{b}}^{\mathrm{S}}$. ρ_0^{S} is the solid density in reference configuration. The balance equation is formulated for the initial structure domain in reference configuration $\Omega_0^{\mathrm{S}} \times (0, T)$.

Fluid–solid interface and coupling

The coupling of the fluid domain and the solid domain is achieved by the interface conditions on the fluid-solid interface $\Gamma^{\mathrm{F,S}} \times (0, T)$. Here, the balance of tractions $\boldsymbol{h}_{\Gamma}^{\mathrm{S}}$ between fluid and solid phase and a no-slip interface condition on the respective primary variables need to hold

$$\boldsymbol{h}_{\Gamma}^{\mathrm{S}} = -\boldsymbol{h}_{\Gamma}^{\mathrm{F}} \qquad \text{on } \Gamma^{\mathrm{F,S}} \times (0, T), \tag{20a}$$

$$\frac{\partial \boldsymbol{d}^{\mathrm{S}}}{\partial t} = \boldsymbol{v}_{\Gamma}^{\mathrm{F}} \qquad \text{on } \Gamma^{\mathrm{F,S}} \times (0, T). \tag{20b}$$

Consequently, in Fig. 2 the initial biofilm interface is labeled $\Gamma_0^{\mathrm{F,S}}$ which is the same as the interface in reference configuration.

Numerical discretization of the fluid–solid interaction problem

For all of the discussed problems in this article, the numerical discretization of the governing equations is conducted with the finite element method (FEM). We use a monolithic approach to solve the coupled FSI equations in ALE formulation [58,59], as the approach was shown to be well suited for biomedical problems of similar type [60] and has also been applied in the biofilm setting before [61].

Reproducing Kernel Hilbert space details

The *reproducing kernel* property implies that the inner product of the kernel and a function reproduces the original function, according to

$$\boldsymbol{f}(\boldsymbol{y}) = \langle \boldsymbol{f}(\boldsymbol{x}), \boldsymbol{k}(\boldsymbol{x}, \boldsymbol{y}) \rangle_{\mathcal{H}}. \tag{21}$$

The kernel $\boldsymbol{k}(\boldsymbol{x}, \boldsymbol{y})$ must be a positive definite function and is unique for the associated RKHS. For our investigations we furthermore require the kernel to be symmetric such that $\boldsymbol{k}(\boldsymbol{x}, \boldsymbol{y}) = \boldsymbol{k}(\boldsymbol{y}, \boldsymbol{x})$, with $\boldsymbol{k}(\cdot, \boldsymbol{y}) \in \mathcal{H}$. Symmetry allows us to interpret the kernel function as a correlation function in a statistical sense, which is commonly done in probabilistic machine learning [39,53]. A kernel can be generated by an associated *feature map* $\boldsymbol{\phi} : \mathcal{X} \to \mathcal{H}$ in the sense of $\boldsymbol{k}(\boldsymbol{x}, \boldsymbol{y}) := \langle \boldsymbol{\phi}(\boldsymbol{x}), \boldsymbol{\phi}(\boldsymbol{y}) \rangle_{\mathcal{H}}$. The feature map $\boldsymbol{\phi}$ can be an infinite dimensional vector, or an infinite series, respectively. Often, only a resulting valid reproducing kernel $\boldsymbol{k}$ is known and the associated feature map $\boldsymbol{\phi}$ remains unknown (kernel trick). Loosely speaking, a desirable property of an RKHS is that a small value of the inner product of the distance function $\boldsymbol{d}$ implies also point-wise closeness of associated functions $\boldsymbol{f}_1$ and $\boldsymbol{f}_2$ [22, 62]. The choice of kernel function encodes the smoothness and complexity assumptions about the underlying functions in the inner product. The latter are usually given in a discrete point representation and the continuous function is represented via the kernel function according to the well known *representer theorem*, which directly demonstrates the interpretation of the kernel as basis functions for the underlying function or curve

$$\boldsymbol{f} = \sum_{i=1}^{n} \alpha_i \boldsymbol{k}(\cdot, \boldsymbol{x}_i). \tag{22}$$

Therefore it can be represented by linear combinations with factors α_i. An extensive overview of common kernels and kernel algebra can be found in [53]. We only briefly demonstrate the *radial basis function (RBF)* kernel, which results in smooth, infinitely differentiable functions and is also used in our investigations

$$k(\boldsymbol{x}, \boldsymbol{y}) = \exp\left(-\frac{\|\boldsymbol{x}-\boldsymbol{y}\|_2^2}{2\sigma_{\mathrm{W}}^2}\right). \tag{23}$$

The RBF kernel with variance σ_{W}^2 describes a mapping $\mathbb{R}^{n\times n} \to \mathbb{R}$, such that it is treated as a scalar $k(\boldsymbol{x}, \boldsymbol{y})$ in the following. After the presentation of the general concepts of inner products in RKHS, we will now discuss possible definitions of distance measures. For the sake of simplicity, we investigate two-dimensional parameterized curves $\boldsymbol{f}(\boldsymbol{s})$, but the concepts generalize easily to three spatial dimensions and parameterized representation of surfaces. An arbitrary curve can be fully described by the parameterized vector representation in (24a). We can calculate the unit-normal vectors of the curve by differentiation w.r.t. the parameter $\boldsymbol{s}$ as demonstrated in (24b).

$$\boldsymbol{f}(\boldsymbol{s}) = \left[g(\boldsymbol{s}),\ h(\boldsymbol{s})\right]^T \tag{24a}$$

$$\boldsymbol{n}_{\boldsymbol{f}}(\boldsymbol{s}) = \frac{1}{\sqrt{\left(\frac{dh(\boldsymbol{s})}{d\boldsymbol{s}}\right)^2 + \left(\frac{dg(\boldsymbol{s})}{d\boldsymbol{s}}\right)^2}} \left[-\frac{dh(\boldsymbol{s})}{d\boldsymbol{s}},\ \frac{dg(\boldsymbol{s})}{d\boldsymbol{s}}\right]^T \tag{24b}$$

Given the parameterization in (24a) a natural choice for a distance is given by the inner product

$$\mathfrak{D}_{\mathcal{V},\boldsymbol{f}} = \langle \boldsymbol{d}_{\boldsymbol{f}}, \boldsymbol{d}_{\boldsymbol{f}} \rangle, \tag{25a}$$

$$\text{with } k\left(\boldsymbol{f}_1, \boldsymbol{f}_2\right) = \exp\left(-\frac{\|\boldsymbol{d}_{\boldsymbol{f}}\|_2^2}{2\sigma_{\mathrm{W}}^2}\right). \tag{25b}$$

In contrast to the closest point projection or L_2 norms, inner products in RKHS correlate all discretized points of curve $\boldsymbol{f}_1$ with all discretized points of curve $\boldsymbol{f}_2$, such that it is not important to identify specific point pairs for which the measure is calculated. While, (25a) is a valid distance measure, it might not account enough for different complexities of $\boldsymbol{f}_1$ and $\boldsymbol{f}_2$ if the overall distance in the Hilbert space is small. This is why we do not follow this approach in this paper.

To put more emphasis on the difference in functional complexity, one can incorporate derivatives of the curves in the measure. Hence, another special choice of distance measure, that will also be used in this paper, can be constructed with the difference in the vector function of the normal vectors $\boldsymbol{n}_{\boldsymbol{f}_1}$ and $\boldsymbol{n}_{\boldsymbol{f}_2}$ from (24b), instead of the difference of the functions themselves.

Brief presentation of used Gaussian process regression model

A Gaussian process (GP) is fully defined by its mean function $\mathrm{m}(x)$ and a correlation function $k(\bullet, \bullet)$ (or kernel, see, e.g., [39,53]) and describes a distribution over functions $f(\boldsymbol{x})$, such that for a fixed $\hat{\boldsymbol{x}}$, the function value $f(\hat{\boldsymbol{x}})$ is normally distributed according to $f(\hat{\boldsymbol{x}}) \sim \mathcal{N}\left(f|\mathrm{m}(\hat{\boldsymbol{x}}), \mathrm{k}_x(\hat{\boldsymbol{x}}, \hat{\boldsymbol{x}})\right)$. A realization of a Gaussian process (GP) can be written as

$$f(x) \sim \mathcal{GP}\left(\mathrm{m}(\boldsymbol{x}), k\left(\boldsymbol{x}, \boldsymbol{x}'\right)\right). \tag{26}$$

As the name suggests, the mean function $\mathrm{m}(\boldsymbol{x})$ represents the statistical mean for an infinite amount of function realizations $f_i(\boldsymbol{x})$. The kernel or covariance function $k\left(\boldsymbol{x}, \boldsymbol{x}'\right)$ encodes the correlation of two function values $f(\boldsymbol{x})$ and $f(\boldsymbol{x}')$ at different inputs $\boldsymbol{x}$ and $\boldsymbol{x}'$. In analogy to the RKHS, the choice of kernel hence encodes smoothness, complexity and characteristics assumptions of the underlying function.

In case we did not account for any data $\mathcal{D} = \{X_{\text{train}}, \boldsymbol{y}_{\text{train}}\}$ in (26), this expression can be interpreted as the so-called *prior* GP. The specific selection of $\mathrm{m}(x)$ and $k\left(\boldsymbol{x}, \boldsymbol{x}'\right)$ can be used to integrate prior knowledge when GPs are used for regression tasks. In this work we will restrict the considerations to a constant prior mean function $\mathrm{m}(\boldsymbol{x}) = const$.

Remark 10 (Prior mean for logarithmic likelihood) For our application, the prior mean function $\mathrm{m}(\boldsymbol{x})$ cannot be neglected, i.e., set to zero, as the log-likelihood for Bayesian calibration (5), that we want to build the regression model for, cannot just randomly be set zero, as then the associated likelihood tends towards a finite value ($\sim \exp(0)$) far away from the training points $\boldsymbol{x}_{\text{train}\,i}$. Strictly the log-likelihood should tend towards negative infinity for irrelevant regions, which is unfeasible, so that the likelihood tends towards zero. Therefore we define an auxiliary mean that is lower than any occurring log-likelihood in the training data $\mathrm{m}(\boldsymbol{x}) = \min(\mathfrak{L}_{\text{train}}) - 1.0 \cdot (\max(\mathfrak{L}_{\text{train}}) - \min(\mathfrak{L}_{\text{train}}))$ with the log-likelihoods $\mathfrak{L}_{\text{train}}$ as training outputs.

In this work we choose a Matérn 3/2 kernel function [39,63,64] for the regression model of the log-likelihood function. In contrast to the infinite differentiable radial basis function kernel used in (23), the Matérn 3/2 kernel is a one time differentiable covariance function [39] that does hence result in samples $f(\boldsymbol{x})$ with lower smoothness requirement. As the log-likelihood might potentially be peaked in areas with high posterior probability density or might also evince abrupt functional changes, we want to relax the smoothness requirements on the regressor. The Matérn 3/2 kernel function is defined as

$$\mathrm{k}_{\text{Matern},\eta=3/2}\left(\boldsymbol{x}, \boldsymbol{x}'\right) = \sigma_{\mathrm{k}}^2 \left(1 + \frac{\sqrt{3}\left\|\boldsymbol{x} - \boldsymbol{x}'\right\|_2}{l_{\mathrm{k}}}\right) \exp\left(-\frac{\sqrt{3}\left\|\boldsymbol{x} - \boldsymbol{x}'\right\|_2}{l_{\mathrm{k}}}\right). \tag{27}$$

The hyper-parameters σ_{k}^2 and l_{k} control the magnitude of the covariance and its length scale, respectively.

Typically there is *training data* $\mathcal{D} = \{X_{\text{train}}, \boldsymbol{y}_{\text{train}}\}$ available and the prior GP can be *conditioned* on $\mathcal{D}$ to yield the *posterior* GP, whose posterior mean function $\bar{f}_*(\boldsymbol{x}_*)$ is then used as a regression model. Training data are input–output pairs of values that are known or can be determined systematically. The posterior variance function $\mathbb{V}\left[f_*\right](\boldsymbol{x}_*)$ serves as a measure for the uncertainty in the regression model. Here it is assumed that $\boldsymbol{y}_{\text{train}} = \left[y_1, \ldots, y_{n_{\text{train}}}\right]^{\mathsf{T}}$ consists of n_{train} scalars (log-likelihood $\mathfrak{L}_{\text{train}}$ in the presented approach) at potentially vector-valued training inputs $X_{\text{train}} = \{\boldsymbol{x}_{\text{train},i}\}\big|_{i=1}^{n_{\text{train}}}$ (forward model parameters $\boldsymbol{x}_{\text{train}}$ in presented approach). The test point $\boldsymbol{x}_*$ denotes a new input for the prediction of the regression model. The posterior mean and variance function can be calculated from the prior GP and the training data $\mathcal{D}$ using the following expressions [39]

$$\bar{f}_* = \boldsymbol{k}_*^{\mathsf{T}}\left(\boldsymbol{K} + \sigma_{\mathrm{n}}^2 \boldsymbol{I}\right)^{-1}\left(\boldsymbol{y}_{\text{train}} - \mathbf{m}\right), \tag{28a}$$

$$\mathbb{V}\left[f_*\right] = \mathrm{k}_x(\boldsymbol{x}_*, \boldsymbol{x}_*) - \boldsymbol{k}_*^{\mathsf{T}} \boldsymbol{K}^{-1} \boldsymbol{k}_*. \tag{28b}$$

In (28) we use the abbreviations $\boldsymbol{K} = k\left(X_{\text{train}}, X_{\text{train}}\right)$ for the covariance matrix at training inputs and the vector $\boldsymbol{k}_* = k\left(X_{\text{train}}, \boldsymbol{x}_*\right)$ for kernel evaluations at test point and training data. $\mathbf{m}$ is a vector of suitable length n_{train} populated with the constant prior mean $\mathrm{m}\left(\boldsymbol{x}\right)$ in all entries. The so-called nugget noise variance σ_{n}^2 is used for numerical stability of the GP [39].

The optimization of the so-called *marginal likelihood* or *evidence* of the GP w.r.t. the hyper-parameters $\sigma_{\mathrm{k}}^2, l_{\mathrm{k}}$ in (27) is known as the *training* of the Gaussian process. The log-marginal likelihood expresses the likelihood of the training data under the chosen model parameterization and it is given by

$$\begin{aligned} -\log p\left(\mathcal{D}|\sigma_{\mathrm{k}}^2, l_{\mathrm{k}}\right) = \\ = \frac{1}{2}\left(\boldsymbol{y}_{\text{train}} - \mathbf{m}\right)^{\mathsf{T}} \boldsymbol{K}^{-1}\left(\boldsymbol{y}_{\text{train}} - \mathbf{m}\right) + \frac{1}{2}\log|\boldsymbol{K}| + \frac{n_{\text{train}}}{2}\log 2\pi \end{aligned} \tag{29}$$

For numerical reasons one usually minimizes the negative log-marginal likelihood instead of maximizing the marginal likelihood directly.

Acknowledgements
Funding of the project with project number WA 1521/22 for this work by the German Research Foundation (DFG) is gratefully acknowledged. Furthermore, the research was partly funded by the German Research Foundation (DFG) under the priority program SPP 1886 *Polymorphic uncertainty modeling for the numerical design of structures*. SB gratefully acknowledges funding from the German Research Foundation (Deutsche Forschungsgemeinschaft, DFG) - Projektnummer 386349077. A base version of the software QUEENS was provided by AdCo Engineering^{GW} GmbH, which is gratefully acknowledged. The first implementation of Gaussian processes and further infrastructure in QUEENS done by B. Wirthl is gratefully acknowledged.

Author contributions
HW implemented the workflow in QUEENS, run the simulations and generated the figures. HW and JN concepted and discussed the approach. SB implemented the SMC integration and contributed to the discussion of its application. WAW concepted the general outline of the project. All authors read and approved the manuscript.

Funding
Open Access funding enabled and organized by Projekt DEAL. This work was funded by the German Research Foundation (DFG) with different projects of the authors. HW was funded with project number WA 1521/22, JN by priority program SPP 1886 *Polymorphic uncertainty modeling for the numerical design of structures* and SB with project number 386349077.

Availability of data and materials
The research code is hosted on a private GitLab repository at Leibniz Rechenzentrum (LRZ) in Garching. The generated numerical results and digital data are held on machines that are backed up on servers managed by the LRZ in Garching. The datasets used and/or analysed during the current study are available from the corresponding author on reasonable request.

Declarations

Competing interests
The authors declare that they have no competing interests.

Received: 9 June 2022 Accepted: 28 November 2022
Published online: 22 December 2022

References

1. Bilionis I, Zabaras N. Solution of inverse problems with limited forward solver evaluations: a Bayesian perspective. Inverse Probl. 2013;30(1): 015004. https://doi.org/10.1088/0266-5611/30/1/015004.
2. Kennedy MC, O'Hagan A. Bayesian calibration of computer models. J Royal Stat Soc Ser B. 2001;63(3):425–64. https://doi.org/10.1111/1467-9868.00294.
3. Tarantola A. Inverse problem theory and methods for model parameter estimation. Philadelphia: SIAM Society for Industrial and Applied Mathematics; 2005.
4. Moireau P, Chapelle D, Tallec PL. Filtering for distributed mechanical systems using position measurements: perspectives in medical imaging. Inverse Probl. 2009;25(3): 035010. https://doi.org/10.1088/0266-5611/25/3/035010.
5. Sermesant M, Moireau P, Camara O, Sainte-Marie J, Andriantsimiavona R, Cimrman R, Hill DLG, Chapelle D, Razavi R. Cardiac function estimation from MRI using a heart model and data assimilation: advances and difficulties. Med Image Anal. 2006;10(4):642–56. https://doi.org/10.1016/j.media.2006.04.002.
6. Kehl S, Gee MW. Calibration of parameters for cardiovascular models with application to arterial growth. Int J Numer Methods Biomed Eng. 2016;33(5):2822. https://doi.org/10.1002/cnm.2822.

7. Flemming H-C, Wingender J. The biofilm matrix. Nat Rev Microbiol. 2010;8(9):623–33. https://doi.org/10.1038/nrmicro2415.
8. Böl M, Ehret AE, Albero AB, Hellriegel J, Krull R. Recent advances in mechanical characterisation of biofilm and their significance for material modelling. Crit Rev Biotechnol. 2013;33(2):145–71. https://doi.org/10.3109/07388551.2012.679250.
9. Gloag ES, Fabbri S, Wozniak DJ, Stoodley P. Biofilm mechanics: implications in infection and survival. Biofilm. 2020;2:100017. https://doi.org/10.1016/j.bioflm.2019.100017.
10. Boudarel H, Mathias J-D, Blaysat B, Grédiac M. Towards standardized mechanical characterization of microbial biofilms: analysis and critical review. npj Biofilms Microbiomes. 2018;4:17. https://doi.org/10.1038/s41522-018-0062-5.
11. Picioreanu C, Blauert F, Horn H, Wagner M. Determination of mechanical properties of biofilms by modelling the deformation measured using optical coherence tomography. Water Res. 2018;145:588–98. https://doi.org/10.1016/j.watres.2018.08.070.
12. Willmann H, Wall WA. Inverse analysis of material parameters in coupled multi-physics biofilm models. Adv Model Simul Eng Sci. 2022. https://doi.org/10.1186/s40323-022-00220-0.
13. Wagner M, Taherzadeh D, Haisch C, Horn H. Investigation of the mesoscale structure and volumetric features of biofilms using optical coherence tomography. Biotechnol Bioeng. 2010;107(5):844–53. https://doi.org/10.1002/bit.22864.
14. Blauert F, Horn H, Wagner M. Time-resolved biofilm deformation measurements using optical coherence tomography. Biotechnol Bioeng. 2015;112(9):1893–905. https://doi.org/10.1002/bit.25590.
15. Gierl L, Stoy K, Faíña A, Horn H, Wagner M. An open-source robotic platform that enables automated monitoring of replicate biofilm cultivations using optical coherence tomography. npj Biofilms Microbiomes. 2020;6:18. https://doi.org/10.1038/s41522-020-0129-y.
16. Jackson BD, Connolly JM, Gerlach R, Klapper I, Parker AE. Bayesian estimation and uncertainty quantification in models of urea hydrolysis by *E. coli* biofilms. Inverse Probl Sci Eng. 2021;29(11):1629–52. https://doi.org/10.1080/17415977.2021.1887172.
17. Robert CP. The Bayesian choice. New York: Springer; 2007. https://doi.org/10.1007/0-387-71599-1.
18. Sternfels R, Koutsourelakis P-S. Stochastic design and control in random heterogeneous materials. Int J Multiscale Comput Eng. 2011;9(4):425–43. https://doi.org/10.1615/IntJMultCompEng.v9.i4.60.
19. Koutsourelakis PS. Design of complex systems in the presence of large uncertainties: a statistical approach. Comput Methods Appl Mech Eng. 2008;197(49–50):4092–103. https://doi.org/10.1016/j.cma.2008.04.012.
20. Kaipio J, Somersalo E. Stat Comput Inverse Probl. New York: Springer; 2004. https://doi.org/10.1007/b138659.
21. Bishop CM. Pattern recognition and machine learning. New York: Springer; 2011.
22. Aronszajn N. Theory of reproducing kernels. Trans Am Math Soc. 1950;68(3):337–337. https://doi.org/10.1090/S0002-9947-1950-0051437-7.
23. Vaillant M, Glaunès J, Christensen G, Sonka M. Surface matching via currents. In: Information Processing in Medical Imaging, pp. 381–392. Springer, Berlin, Heidelberg 2005.
24. Imperiale A, Routier A, Durrleman S, Moireau P. Improving efficiency of data assimilation procedure for a biomechanical heart model by representing surfaces as currents. In: Ourselin S, Rueckert D, Smith N, editors. Functional imaging and modeling of the heart. Berlin: Springer; 2013. p. 342–51. https://doi.org/10.1007/978-3-642-38899-6_41.
25. Geyer CJ. Practical markov chain monte carlo. Statistical science, 1992; 473–483.
26. Chib S, Greenberg E. Understanding the metropolis-hastings algorithm. Am Stat. 1995;49(4):327–35. https://doi.org/10.1080/00031305.1995.10476177.
27. Glynn PW, Iglehart DL. Importance sampling for stochastic simulations. Manag Sci. 1989;35(11):1367–92. https://doi.org/10.1287/mnsc.35.11.1367.
28. Tokdar ST, Kass RE. Importance sampling: a review. WIREs Comput Stat. 2010;2(1):54–60. https://doi.org/10.1002/wics.56.
29. Doucet A, Freitas N, Gordon N, editors. Sequential Monte Carlo methods in practice. New York: Springer; 2001. https://doi.org/10.1007/978-1-4757-3437-9.
30. Chopin N, Papaspiliopoulos O. An Introduction to Sequential Monte Carlo. Cham: Springer; 2020. https://doi.org/10.1007/978-3-030-47845-2.
31. Blei DM, Kucukelbir A, McAuliffe JD. Variational inference: a review for statisticians. J Am Stat Assoc. 2017;112(518):859–77. https://doi.org/10.1080/01621459.2017.1285773.
32. Hoffman MD, Blei DM, Wang C, Paisley J. Stochastic variational inference. J Mach Learn Res. 2013;14(4):1303–47.
33. Del Moral P, Doucet A, Jasra A. Sequential Monte Carlo for Bayesian computation. In: Bernardo JM, Bayarri MJ, Berger JO, Dawid AP, Heckerman D, Smith AFM, West M, editors. Bayesian Statistics 8. Oxford: Oxford University Press; 2007. p. 1–34.
34. Koutsourelakis PS. A multi-resolution, non-parametric, Bayesian framework for identification of spatially-varying model parameters. J Comput Phys. 2009;228(17):6184–211. https://doi.org/10.1016/j.jcp.2009.05.016.
35. Chopin N. A sequential particle filter method for static models. Biometrika. 2002;89(3):539–52. https://doi.org/10.1093/biomet/89.3.539.
36. Del Moral P, Doucet A, Jasra A. Sequential Monte Carlo samplers. J Royal Stat Soc Ser B. 2006;68(3):411–36. https://doi.org/10.1111/j.1467-9868.2006.00553.x.
37. Minson SE, Simons M, Beck JL. Bayesian inversion for finite fault earthquake source models i-theory and algorithm. Geophys J Int. 2013;194(3):1701–26. https://doi.org/10.1093/gji/ggt180.
38. Robert CP, Casella G. Monte Carlo statistical methods. New York: Springer; 2004. https://doi.org/10.1007/978-1-4757-4145-2.
39. Rasmussen CE, Williams CKI. Gaussian Processes for Machine Learning. MIT Press Ltd, Cambridge, Massachusetts 2006. first (University of Cambridge) second (University of Edinburgh).
40. Sobol I. The distribution of points in a cube and the accurate evaluation of integrals (in Russian). Zh Vychisl Mat i Mater Phys. 1967;7:784–802.

41. Owen AB. Scrambling Sobol'and niederreiter-xing points. J Complex. 1998;14(4):466–89. https://doi.org/10.1006/jcom.1998.0487.
42. Kucherenko S, Albrecht D, Saltelli A. Exploring multi-dimensional spaces: a Comparison of Latin Hypercube and Quasi Monte Carlo Sampling Techniques 2015. arXiv:1505.02350.
43. Biehler J, Nitzler J, Wall WA, Gravemeier V. QUEENS - A Software Platform for Uncertainty Quantification, Physics-Informed Machine Learning, Bayesian Optimization, Inverse Problems and Simulation Analytics: User Guide. AdCoEngineering^{GW} 2019.
44. GPy: GPy: A Gaussian process framework in python. http://github.com/SheffieldML/GPy, Last accessed on 2021-08-20 (since 2012)
45. Schroeder W, Martin K, Lorensen B. The Visualization Toolkit: an Object-oriented Approach to 3D Graphics. Clifton Park, N.Y: Kitware; 2006.
46. Waskom ML. seaborn: statistical data visualization. J Open Source Softw. 2021;6(60):3021. https://doi.org/10.21105/joss.03021.
47. Hunter JD. Matplotlib: a 2d graphics environment. Comput Sci Eng. 2007;9(3):90–5. https://doi.org/10.1109/MCSE.2007.55.
48. Plotly Technologies Inc.: Collaborative Data Science. https://plot.ly
49. Paszke A, Gross S, Massa F, Lerer A, Bradbury J, Chanan G, Killeen T, Lin Z, Gimelshein N, Antiga L, Desmaison A, Kopf A, Yang E, De Vito Z, Raison M, Tejani A, Chilamkurthy S, Steiner B, Fang L, Bai J, Chintala S. Pytorch: An imperative style, high-performance deep learning library. In: Wallach H, Larochelle H, Beygelzimer A, d' Alché-Buc F, Fox E, Garnett R. (eds.) Advances in Neural Information Processing Systems 2019;32:8024–8035. Curran Associates, Inc., Vancouver, BC, Canada.
50. BACI: a comprehensive multi-physics simulation framework. https://baci.pages.gitlab.lrz.de/website/. Accessed 16 June 2021.
51. Coroneo M, Yoshihara L, Wall WA. Biofilm growth: a multi-scale and coupled fluid-structure interaction and mass transport approach. Biotechnol Bioeng. 2014;111(7):1385–95. https://doi.org/10.1002/bit.25191.
52. Schölkopf B, Smola A, MÜller K-R. Kernel principal component analysis. In: Gerstner, W., Germond, A., Hasler, M., Nicoud, J.-D. (eds.) Artificial Neural Networks - ICANN'97, 1997; vol. 1327, pp. 583–588. Springer, Berlin Heidelberg. https://doi.org/10.1007/BFb0020217.
53. Duvenaud D. Automatic model construction with gaussian processes. PhD thesis, University of Cambridge 2014.
54. Brandstaeter S, Fuchs SL, Biehler J, Aydin RC, Wall WA, Cyron CJ. Global sensitivity analysis of a homogenized constrained mixture model of arterial growth and remodeling. J Elast. 2021;145(1–2):191–221. https://doi.org/10.1007/s10659-021-09833-9.
55. Wirthl B, Brandstaeter S, Nitzler J, Schrefler BA, Wall WA. Global sensitivity analysis based on gaussian-process meta-modelling for complex biomechanical problems 2022. arXiv:2202.01503.
56. Nitzler J, Biehler J, Fehn N, Koutsourelakis P-S, Wall WA. A generalized probabilistic learning approach for multi-fidelity uncertainty quantification in complex physical simulations. Comput Methods Appl Mech Eng. 2022;400: 115600. https://doi.org/10.1016/j.cma.2022.115600.
57. Wagner M, Horn H. Optical coherence tomography in biofilm research: a comprehensive review. Biotechnol Bioeng. 2017;114(7):1386–402. https://doi.org/10.1002/bit.26283.
58. Gee MW, Küttler U, Wall WA. Truly monolithic algebraic multigrid for fluid-structure interaction. Int J Numer Methods Eng. 2010;85(8):987–1016. https://doi.org/10.1002/nme.3001.
59. Yoshihara L, Coroneo M, Comerford A, Bauer G, Klöppel T, Wall WA. A combined fluid-structure interaction and multi-field scalar transport model for simulating mass transport in biomechanics. Int J Numer Methods Eng. 2014;100(4):277–99. https://doi.org/10.1002/nme.4735.
60. Küttler U, Gee M, Förster C, Comerford A, Wall WA. Coupling strategies for biomedical fluid-structure interaction problems. Int J Numer Methods Biomed Eng. 2010;26(3–4):305–21. https://doi.org/10.1002/cnm.1281.
61. Taherzadeh D, Picioreanu C, Küttler U, Simone A, Wall WA, Horn H. Computational study of the drag and oscillatory movement of biofilm streamers in fast flows. Biotechnol Bioeng. 2010;105(3):600–10. https://doi.org/10.1002/bit.22551.
62. Berlinet A, Thomas-Agnan C. Reproducing Kernel Hilbert spaces in probability and statistics. New York: Springer; 2004. https://doi.org/10.1007/978-1-4419-9096-9.
63. Stein ML. Interpolation of spatial data. New York: Springer; 1999.
64. Matérn B. Spatial variation. New York: Springer; 1986. https://doi.org/10.1007/978-1-4615-7892-5.

Publisher's Note